SINGLE MOLECULE TRACKING STUDIES OF FLOW-ALIGNED MESOPOROUS SILICA MONOLITHS: PORE ORDER AND PORE WALL PERMEABILITY

by

SEOK CHAN PARK

B.S., Hanyang University, 2005
M.S., Hanyang University, 2007

AN ABSTRACT OF A DISSERTATION

submitted in partial fulfillment of the requirements for the degree

DOCTOR OF PHILOSOPHY

Department of Chemistry
College of Arts and Sciences

KANSAS STATE UNIVERSITY
Manhattan, Kansas

2015

Abstract

This dissertation describes single-molecule tracking (SMT) studies for the quantitative characterization of one-dimensional (1D) nanostructures in surfactant-templated mesoporous silica monoliths prepared within microfluidic channels. Single molecule diffusion of fluorescent probe molecules within the cylindrical mesopores reflects microscopic morphologies and mass-transport properties of the materials with high temporal and spatial resolution. The pore organization and materials order are initially investigated as a function of sol aging prior to loading into the microfluidic channels. Mesopores in these materials are templated by Cetyltrimethylammonium bromide (CTAB). Wide-field fluorescence videos depict 1D motion of the dyes within the individual mesopores. Orthogonal regression analysis of these motions provides a measure of the mesopore orientation. Channels filled prior to gelation of the sol produce monoliths incorporating large monodomains with highly aligned mesopores. In contrast, channels filled close to or after gelation yield monoliths with misaligned pores that are also more disordered. Two-dimensional (2D) small angle X-ray scattering (SAXS) experiments support the results obtained by SMT. These studies help to identify conditions under which highly aligned mesoporous monoliths can be obtained and also demonstrate the utility of SMT for characterization of mesopore order.

The non-ionic surfactant Pluronic F127 is also utilized as the structural-directing agent. The diffusive motions of PDI dyes that are uncharged, cationic and anionic are explored by SMT and fluorescence correlation spectroscopy (FCS). The SMT studies for the uncharged dye show development of 1D diffusion along the flow direction while charged dyes exhibit predominant isotropic diffusion, with each of these behaviors becoming more prevalent as a function of aging time after filling of the microfluidic channels. SMT studies from silica-free F127 gels suggest that

partitioning plays a important role in governing the diffusion behavior of the PDI dyes within the surfactant-filled mesopores. FCS results exhibit similar mean diffusion coefficients for all three dyes that suggest these dyes diffuse through similar sample regions. These studies demonstrate that the silica pore walls in the mesoporous silica monoliths remain permeable after gelation and that partitioning of solute species to different regions within the pores plays an important role in restricting the dimensionality of their diffusive motion.

SINGLE MOLECULE TRACKING STUDIES OF FLOW-ALIGNED MESOPOROUS SILICA MONOLITHS: PORE ORDER AND PORE WALL PERMEABILITY

by

SEOK CHAN PARK

B.S., Hanyang University, 2005
M.S., Hanyang University, 2007

A DISSERTATION

submitted in partial fulfillment of the requirements for the degree

DOCTOR OF PHILOSOPHY

Department of Chemistry
College of Arts and Sciences

KANSAS STATE UNIVERSITY
Manhattan, Kansas

2015

Approved by:

Major Professor
Dr. Daniel A. Higgins

Copyright

Abstract

This dissertation describes single-molecule tracking (SMT) studies for the quantitative characterization of one-dimensional (1D) nanostructures in surfactant-templated mesoporous silica monoliths prepared within microfluidic channels. Single molecule diffusion of fluorescent probe molecules within the cylindrical mesopores reflects microscopic morphologies and mass-transport properties of the materials with high temporal and spatial resolution. The pore organization and materials order are initially investigated as a function of sol aging prior to loading into the microfluidic channels. Mesopores in these materials are templated by Cetyltrimethylammonium bromide (CTAB). Wide-field fluorescence videos depict 1D motion of the dyes within the individual mesopores. Orthogonal regression analysis of these motions provides a measure of the mesopore orientation. Channels filled prior to gelation of the sol produce monoliths incorporating large monodomains with highly aligned mesopores. In contrast, channels filled close to or after gelation yield monoliths with misaligned pores that are also more disordered. Two-dimensional (2D) small angle X-ray scattering (SAXS) experiments support the results obtained by SMT. These studies help to identify conditions under which highly aligned mesoporous monoliths can be obtained and also demonstrate the utility of SMT for characterization of mesopore order.

The non-ionic surfactant Pluronic F127 is also utilized as the structural-directing agent. The diffusive motions of PDI dyes that are uncharged, cationic and anionic are explored by SMT and fluorescence correlation spectroscopy (FCS). The SMT studies for the uncharged dye show development of 1D diffusion along the flow direction while charged dyes exhibit predominant isotropic diffusion, with each of these behaviors becoming more prevalent as a function of aging time after filling of the microfluidic channels. SMT studies from silica-free F127 gels suggest

that partitioning plays a important role in governing the diffusion behavior of the PDI dyes within the surfactant-filled mesopores. FCS results exhibit similar mean diffusion coefficients for all three dyes that suggest these dyes diffuse through similar sample regions. These studies demonstrate that the silica pore walls in the mesoporous silica monoliths remain permeable after gelation and that partitioning of solute species to different regions within the pores plays an important role in restricting the dimensionality of their diffusive motion

Table of Contents

List of Figures xi
List of Tables xvi
Acknowledgements xvii
Dedication xviii
Acronyms and Definitions xix
Variables and Descriptions xx
Chapter 1 - General Introduction 1
1. 1 Mesoporous Silcia Materials 1
1. 2 Single Molecule Tracking Methods Applied to Mesoporous Silica 3
1. 3 Objectives and Motivations of the Present Research 5
Chapter 2 - Surfactant-templated Mesoporous Silica Materials 8
2. 1 Silica Sol-Gel Process 9
2. 2 Preparation of Surfactant-Templated Mesoporous Silica 10
2. 3 Influence of Synthetic Parameters 13
2. 4 Control of One-dimensional (1D) Mesopores 13
2. 4. 1 Control of Mesopore Orientation in Solution Phase Synthesis 14
2. 4. 2 Control of 1D Mesopores in Mesoporous Silica Films 16
2. 4. 2. 1 Orientation by Confinement 17
2. 4. 2. 2 Spontaneous Pore Orientation on Modified Substrates. 18
2. 4. 2. 3 Application of External Fields 19
2. 4. 3 Flow-alignment in Mesoporous Silica Monoliths 20
2. 5 Pore Wall Permeability 21
Chapter 3 - Experimental Considerations 25
3. 1 Silica Sol Preparation: Formation of the Hexagonal Mesophase 25
3. 2 Perylene Diimide (PDI) Dyes 26
3. 3 Instrumentation 27
3. 3. 1 Two-dimensional (2D) Small Angle X-Ray Scattering (SAXS) 27
3. 3. 2 Wide-field Fluorescence Microscopy 28

3. 3. 3 Confocal Fluorescence Microscopy 30
3. 4 Single molecular Trajectory Analysis 31
3. 4. 1 Orthogonal Regression 31
3. 4. 2 Trajectory Angle Order Parameter 33
Chapter 4 - Single Molecule Tracking Studies of Flow-Aligned Mesoporous Silica Monoliths: Aging-Time Dependence of Pore Order 35
4. 1 Introduction 35
4. 2 Experimental Section 38
4. 2. 1 Sample Preparation 38
4. 2. 2 Microfluidic Channel Design and Fabrication 39
4. 2. 3 Flow Alignment of Sols 40
4. 2. 4 Single Molecule Tracking 41
4. 2. 5 2D SAXS Measurements 43
4. 3 Results 43
4. 3. 1 2D SAXS Measurements 43
4. 3. 2 Single Molecule Tracking Studies 45
4. 4 Discussion 52
4. 4. 1 Quantitative Assessment of Mesopore Alignment and Order 52
4. 4. 2 Mechanism for Organization of Flow-Aligned Mesopores 56
4. 5 Conclusion 58
Chapter 5 - On the Dimensionality of Diffusion in Flow-Aligned Surfactant-Templated Mesoporous Silica: A Single Molecule Tracking Study of Pore Wall Permeability 60
5. 1 Introduction 60
5. 2 Experimental Considerations 63
5. 2. 1 Sample Preparation 63
5. 2. 2 Flow Alignment of Gels 63
5. 2. 3 Single Molecule Tracking 65
5. 2. 4 Fluorescence Correlation Spectroscopy (FCS) 67
5. 3 Results and Discussion 67
5. 3. 1 General Observations from Video Data 68
5. 3. 2 Quantitative Analysis of Single Molecule Trajectories in Mesoporous Silica 70

5. 3. 3 Comparisons with F127 Gels in the Absence of Silica 74
5. 3. 4 Diffusion Coefficient Measurements 77
5. 3. 5 Model for Confinement of Dyes in F127-Templated Mesoporous Silica 80
5. 4 Conclusion 81
Chapter 6 - General Conclusions and Future Directions 83
Chapter 7 - References 87

List of Figures

Figure 2.1 General mechanisms of hydrolysis and condensation of alkoxysilane precursors to form silica under (a) acid catalyzed conditions and (b) base catalyzed conditions. Condensation can produce either water or alcohol as a byproduct. Adapted with permission from Ref (62). Copyright © 2013, Royal Society of Chemistry..... 10

Figure 2.2 Structures of mesoporous M41S materials: a) MCM-41 (2D hexagonal, space group $\boldsymbol{p6mm}$), b) MCM-48 (cubic, space group $\boldsymbol{Ia3d}$), and c) MCM-50 (lamellar, space group $\boldsymbol{p2}$). Adapted with permission from Ref (66). Copyright © 2006 WILEY-VCH Verlag GmbH & Co. KGaA, Weinheim..... 11

Figure 2.3 Formation of mesoporous materials by structure-directing agents: a) true liquid-crystal template mechanism, b) cooperative liquid crystal template mechanism. Adapted with permission from Ref (66). Copyright © 2006 WILEY-VCH Verlag GmbH & Co. KGaA, Weinheim..... 12

Figure 2.4 Schematic structure of a conelike particle produced in an SBA-3-like synthesis. Release from a whole particle is determined by cross-wall transport connected with the flux $\phi_{\text{eff}}\perp$ and the effective diffusion coefficient $D_{\text{eff}}\perp$. (B) After cutting a particle in half, diffusion along the pores becomes effective ($\phi_{\text{eff}}\parallel$ associated with $D_{\text{eff}}\parallel$) with diffusion paths along ξ. Reprinted with permission from Ref (53). Copyright 2007 American Chemical Society. 24

Figure 3.1 Chemical structures of (left) CTAB and (right) Pluronic F127 surfactants. 25

Figure 3.2 (left) The ternary CTAB/water/ethanol phase diagram[127] and (right) phase diagram for F127/water/butanol mixtures[48]. The sol compositions were adjusted to form hexagonal mesophase in both phase diagrams. 26

Figure 3.3 Chemical structures of the uncharged (a), cationic (b), and anionic (c) PDI dye molecules employed in single molecule tracking and FCS experiments..... 27

Figure 3.4 Schematic of a 2D-SAXS instrument with its major components: an X-ray source, sample and a 2D detector. The SAXS data are collected simultaneously for small scattering angles (2θ) and the anisotropic pattern of scattering intensity indicates an ordered and aligned mesostructure of the sample..... 28

Figure 3.5 Schematic of wide-field microscope used for single molecule imaging..... 29

Figure 3.6 Schematic of objective-based TIRF imaging mode. The pink dotted line in the inset image shows the decay of the evanescent field..... 30
Figure 3.7 Schematic of confocal fluorescence microscope set-up used for wide-field single molecule imaging..... 31
Figure 4.1 a) Etched glass microfluidic cell employed to obtain flow-aligned mesoporous silica monoliths for SMT experiments. These cells are comprised of an etched microscope slide incorporating a rectangular channel 15 mm long, 2 mm wide and 70 μm deep, with inlet and outlet holes drilled through the glass at the channel ends. A microscope cover glass is bonded to each slide to enclose the channel and to allow for imaging with a high NA objective. b) Locations at which SMT tracking measurements were made within each monolith (red circles). c) Model for flow-aligned, hexagonally arranged cylindrical surfactant micelles in mesoporous silica..... 40
Figure 4.2 Representative wide-field fluorescence images of a flow-aligned monolith from an 8 h aged sol under different excitation polarizations. The excitation polarization is circular (a, b), horizontal on the optical table (c, d) and vertical on the optical table (e, f). The initial direction of the microfluidic channel axis was parallel to the horizontally polarized incident light (a, c, e) and rotated by 90° (b, d, f). The images were obtained using the Z-project routine in ImageJ and depict the maximum intensity for each pixel in the associated videos. The scale bars are 5 μm..... 41
Figure 4.3 a) X-ray scattering intensity as a function of scattering angle 2θ, derived from the 2D SAXS pattern shown in the inset. The data was obtained from a flow-aligned mesoporous silica monolith prepared within a cylindrical glass capillary from a 4 h aged sol. The capillary was oriented along the vertical direction on the scattering pattern (see inset). b) Characteristic *d*-spacing for hexagonally arranged cylindrical mesopores in the silica monoliths as a function of sol aging time. The data demonstrate that mesopore spacing is independent of sol aging time. Error bars depict the 95% confidence intervals about the mean. c) Scattering intensity as a function of azimuthal angle, χ, from 4h (black) and 20 h (gray) aged sols. Here, 0^o corresponds to the long axis of the capillary..... 44
Figure 4.4 a) Representative wide-field fluorescence image of a flow-aligned monolith prepared from a 4 h aged sol. This image was obtained using the Z-project routine in ImageJ and plots the maximum intensity for each pixel observed in the associated video. b) Single

molecule trajectories obtained from the same video. c) Histogram showing the trajectory angles relative to the flow axis (0^o) in the microfluidic channel. d)-f) Similar data obtained from a flow-alinged monolith prepared from a 20 h aged sol. 47
Figure 4.5 Histograms depicting the trajectory angles compiled from all 9 images collected from each sample in a single, representative set of flow-aligned silica samples, as a function of sol aging time. The data demonstrate that the mesopores are all well aligned along the flow direction (0^o) over distances of several millimeters, for materials prepared prior to gelation of the sol at ~ 19 h. Near the gelation time, markedly more disordered and misaligned materials are obtained (see 20 h data). 49
Figure 4.6 Selected MSD data (symbols) from (a) the shortest (7 frames) and (b) the longest (23 frames for dashed and gray lines, and 18 frames for black line) trajectories in a single video of a flow-aligned monolith from an 8 h aged sol. All frame times were 0.042 s, as described in the experimental section. Dashed and solid lines were obtained by fitting the first five points of each trajectory and diffusion coefficients were determined from the slope of these lines. Error bars depict the standard deviation about the mean in each. 50
Figure 4.7 a) Representative histogram showing diffusion coefficients determined from a single flow-aligned mesoporous silica sample prepared from a 4 h aged sol. The diffusion coefficients were determined from the mean square diffusion coefficients obtained as a function of sol aging time for three replicate sample series. No apparent trend is observed in these data, suggesting the viscosity within the surfactant-containing mesopores is invariant over the range of samples investigated. Error bars depict the 95% confidence intervals about the mean in each case. displacement exhibited by each single molecule at short time delays (i.e. 5 frames).). b) Mean diffusion coefficients obtained as a function of sol aging time for three replicate sample series. No apparent trend is observed in these data, suggesting the viscosity within the surfactant-containing mesopores is invariant over the range of samples investigated. Error bars depict the 95% confidence intervals about the mean in each case. 51
Figure 4.8 Order parameters measured for flow-aligned silica monoliths as a function of sol aging time prior to injection into the microfluidic channel. Shown are SMT data from three replicate sample series along with SAXS data. The data depict a constant, high level of organization up to approximately the gelation time (~ 19 h, vertical line), beyond which an

abrupt decrease in order is observed. The dashed line has been appended to better highlight this tren..... 56
Figure 4.9 Model for the trend in mesopore order as a function of sol aging time. Surfactant-templated sols that are injected into microfluidic channels or capillaries prior to gelation are strongly aligned by shear flow during injection. Subsequent gelation of the sol forms a rigid matrix incorporating well aligned mesopores. For sols close to the gelation time, the rigid gel structure has already begun to form around randomly aligned domains in the original vessel. These sols are not strongly aligned by flow during injection into the channels and capillaries and may be broken up by strong mechanical forces during injection. 57
Figure 5.1 PDMS-based microfluidic cell employed to obtain flow aligned mesoporous silica monoliths and F127 gels. 64
Figure 5.2 Representative TIRF-mode Z-projection images and corresponding trajectory plots obtained from uncharged (a-c), cationic (d-f) and anionic (g-i) PDIs. Results obtained at monolith aging times of 22 h, 41 h and 77 h are shown from top to bottom. Trajectories (≥ 10 frames in length) of immobile molecules and molecules exhibiting 1D and 2D motions are shown in black, red and blue, respectively. 68
Figure 5.3 Fractions of 1D and 2D mobile populations for uncharged (top), cationic (middle) and anionic (bottom) PDI dyes obtained from flow-aligned mesoporous silica monoliths as a function of aging time. Results from 9 videos obtained from each samples were used to obtain each pair of 1D/2D bars. The empty bars represent the 1D mobile population and solid bars indicate the 2D mobile population. The error bars show the 95% confidence intervals. 71
Figure 5.4 Mean trajectory aspect ratios for 1D and 2D trajectories of uncharged (top), cationic (middle) and anionic (bottom) PDI molecules as a function of aging time. The empty bars show the mean trajectory aspect ratios for 1D trajectories, while the solid bars depict the mean 2D trajectory aspect ratios. The error bars show the 95% confidence intervals. 73
Figure 5.5 Representative TIRF-mode images (left) and corresponding trajectory plots (right) obtained from silica-free F127 gels doped with uncharged (a), cationic (b), and anionic (c) dye. Trajectories (≥ 10 frames in length) obtained by tracking the motions of the molecules were separated into immobile (black), and 1D (red) and 2D (blue) mobile populations. The

images were obtained using the Z-project routine in ImageJ and depict the maximum intensity for each pixel in the associated videos. 75
Figure 5.6 Fractions of 1D and 2D mobile populations (a), and mean trajectory aspect ratio of 1D and 2D trajectories (b) for uncharged (black), cationic (red) and anionic (blue) PDI molecules obtained from flow-aligned silica-free F127 gels. The solid bars depict the 1D mobile population and empty bars the 2D mobile population. The error bars show the 95% confidence intervals. 76
Figure 5.7 Representative autocorrelation data from charged and uncharged dye doped samples at each aging time. 78
Figure 5.8 Mean diffusion coefficients estimated from FCS measurements of uncharged (top, black), cationic (middle, red), and anionic (bottom, blue) PDI dye molecules at different aging times. The error bars give the 95% confidence intervals. 79
Figure 5.9 Model for probe localization (a), and diffusion modes for anisotropic (b) and apparent isotropic (c) diffusion. Uncharged dyes (red circles) are mainly localized in hydrophobic core of the F127 micelles (dark gray region) while the charged dyes (blue circles) preferentially partition into the hydrophilic corona region (light gray region)..... 81

List of Tables

Table 4.1 Single molecule tracking data under different excitation polarization and channel direction. Error bars give the 95% confidence intervals of the mean values..... 42

Table 4.2 Single molecule tracking and SAXS data compiled from a series of replicate samples in each case. Errors give the 95% confidence intervals of the mean values..... 55

Acknowledgements

I would like to express my sincere gratitude and appreciation to my advisor Dr. Daniel Higgins. He helps me complete the Ph.D. degree in Department of Chemistry with his constant guidance, valuable advice and ***endless patience*** with my mistakes and continuous encouragement. I also would like to greatly thank my co-advisor Dr. Takashi Ito. Without his great advice I would never grasp how important looking at details in every experiment is. I would also like to thank Dr. Stefan Bossmann, Dr. Keith Hohn, and Dr. Jon Faubion for being on my supervisory committee. I am very thankful for the friendship and support of Dipak Giri and members of the Higgins and Ito group. I would especially like to thank Dr. Khanh-Hoa Tran-Ba for showing me the best attitude to science and his time spending on discussing interesting research and other daily topics.

I also gratefully acknowledge support from the Division of Chemical Sciences, Geosciences, and Biosciences, Office of Basic Energy Sciences, U.S. Department of Energy. Prof. Chris Culbertson is thanked for valuable suggestions on preparing microfluidic devices. SAXS measurements were carried out at the Characterization Facility at the University of Minnesota, which is supported by the NSF MRSEC Program. Linda Sauer and Michael Manno are thanked for their help with SAXS measurements.

Finally, I thank my family for their love, encouragement, and support throughout the years. I am also very thankful for all of my friends who have encouraged me and been there for me throughout my graduate years.

Dedication

To my loving wife Min Jung, my lovely son Junsoo Daniel and especially my proud daughter Miso Stella.

Acronyms and Definitions

1D/2D/3D	One/Two/Three dimensional
APD	Avalanche photo diode
CTAB	Cetyltrimethylammonium bromine
EM	Electron microscopy
EM CCD	Electron multiplying charge-coupled device
FCS	Fluorescence correlation spectroscopy
LCT	Liquid crystal templating
MSD	Mean square displacement
NA	Numerical aperture
NMR	Nuclear magnetic resonance
PAA	Porous anodic alumina
PDI	Perylene Diimide
PDMS	Poly(dimethylsiloxane)
SAXS	Small angle X-ray scattering
SEM	Scanning electron microscopy
SMT	Single-molecule tracking
S/N	Signal-to-noise
TEM	Transmission electron microscopy
TIRF	Total internal reflection fluorescence
TMOS	Tetramethoxysilicate
XRD	X-ray diffraction

Variables and Descriptions

β	Angle of the trajectory segment with respect to the horizontal direction
$\bar{\beta}$	Mean trajectory orientation in a given sample region
$\Delta\beta$	Angular deviation in the direction of the individual trajectories, β from $\bar{\beta}$
δ_i	Error in measuring the position of the molecule
σ (Chapter 4)	Gaussian functions and their widths of SAXS anisotropy data
σ (Chapter 5.3.2)	Localization precision
σ (Chapter 5.3.4)	Lateral detection volume dimensions of the FCS measurement
σ_δ^2	Variance in the position measurement for each molecule along each trajectory
σ_R^2	Motional variance in the molecular position
θ	Angle of the trajectory segment with respect to the horizontal direction
θ (Chapter 4)	X-ray scattering angle
$\bar{\theta}$	Mean trajectory orientation in a given sample region
$\Delta\theta$	Angular deviation in the direction of the individual trajectories, θ from $\bar{\theta}$
χ	Azimuthal angle
a	Pixel size
A	The spot amplitude
b^2	Background noise obtained from the rolling-ball background subtraction step
$i(t)$	Time transient data obtained by FCS measurement
$i(t+\tau)$	Time transient with a time-delay, τ,
N	Total number of photon counts in the spot area
s	Gaussian width of the detected spot

S_{yy}	Arithmetic mean of squared y_i
S_{xx}	Arithmetic mean of squared x_i
S_{xy}	Arithmetic mean of the product of x_i and y_i
x_i	Measured *x* position of a single molecule spot in the video frames
X_i	The best estimate of the actual *x* position of the molecule
y_i	Measured *y* position of a single molecule spot in the video frames
z	Longitudinal detection volume dimensions of the FCS measurement

Chapter 1 - General Introduction

1. 1 Mesoporous Silcia Materials

Mesoporous materials contain pores with diameters between 2 and 50 nm. These materials are typically prepared by the hydrolysis and condensation of inorganic oxide precursors (e.g., alkoxysilanes) in the presence of structure-directing agents such as surfactant micelles. The development of mesoporous materials has employed a diversity of framework compositions (e.g., silica, organosilica, and metals) and various morphologies (e.g., nanoparticles, monoliths, and films) under various synthetic conditions.[1, 2]

Since ordered mesoporous silica particles were first produced by surfactant-templating methods in the early 1990s,[3, 4] these new materials have been utilized in many different fields. These mesoporous silicas were originally developed to afford materials for catalysis and chemical separations that would allow for entry of molecules that were too large to fit in the micropores of conventional zeolites. The pore organization and morphology of mesoporous silica materials are defined by the mesophase of the structure-directing agent (i.e., the structure of the surfactant micelles). The most commonly used mesophases for mesoporous silicas with pore sizes in the range of 2-5 nm are the 2D hexagonal (*p6m* space group), the 3D cubic (*Ia3d*) and the lamellar (*p2*), also known as MCM-41, MCM-48 and MCM-50 materials, respectively.[5] For the preparation of materials with larger pore sizes, 6 to 20 nm in diameter, 2D hexagonal SBA-15 and 3D cubic IBN-2 were developed.[6]

Due to their unique properties, including high surface area, large pore volume, controlled morphology, facile functionalization, and good biocompatibility, mesoporous silica materials have been of interest to many academic and industrial labs for the past few decades.[7, 8] These materials have been explored for use in the fields of catalysis, chemical separation, ion exchange, molecular

sieving, and adsorption.[9-14] Mesoporous silicas have been used as catalytic nano-reactors for the synthesis of conductive polymers,[15-19] and as templates for growth of certain carbon nanostructures such as nanotubes, nanowires and mesoporous carbon materials.[20] Synthetic mesoporous silicas are also being used in the fields of sensors and energy transfer devices.[21-25] Mesoporous silica materials incorporating hexagonally organized cylinder-shaped mesopores have been intensively studied. This is due to the fact that the ordered array of cylindrical channels can serve as a simple model to evaluate materials properties.[26, 27] Such cylindrical open pores find potential applications as supporting media for catalysis and chemical separations, and as drug carriers for selective drug delivery. To facilitate any/all such applications, it is necessary to establish well-defined procedures to produce well-ordered mesoporous silica solids incorporating fully aligned nanochannels and to understand the formation mechanisms of such materials. Most importantly, as described in this dissertation, it is also important that their mass transport properties be fully characterized and understood. Therefore, it is essential to quantitatively evaluate the characteristics of the nanoscale structures and morphologies of these materials, and the behavior of guest molecules in these host systems. Because of the short length scales over which such phenomena are manifested, it is also important that these issues be explored with high spatial resolution in a temporally resolved manner.

The structural characteristics of mesoporous materials are usually assessed by electron microscopy (EM),[4, 28-34] small-angle X-ray scattering (SAXS),[4, 29-31, 35] and nuclear magnetic resonance (NMR) spectroscopy.[35] These methods offer complementary information on the material characteristics and thus it is common to combine two or more of these techniques to complete the structural analysis of mesoporous silicas.

EM (e.g., TEM and SEM) provides visual evidence of local structure of the material through a direct observation of mesopore structure with nanometer scale spatial resolution.[26, 27] The local morphologies including pore diameter and orientation can be directly revealed from the high-resolution microscopic view of the mesostructure. However, due to the extremely small view area, these methods require significant time and labor for longer-range (>10 μm) detection of the pore organization. X-ray scattering techniques also have been widely employed to assess nanostructure size and organization. SAXS measurements are made by detection of the diffraction scattering at very low angles (< 5°). Thus, they reveal information on organized pores 2-30 nm in size in mesoporous silicas. Furthermore, two-dimensional (2D) SAXS measurements provide anisotropy data that reflect the orientation of ordered pore domains, and hence, quantitative measurements of average nanostructure order.[36] However, the materials properties obtained by SAXS measurements are effectively averaged over macroscopic (< 1 mm) sample regions.[26, 27] While EM and SAXS provide microscopic and macroscopic views of the physical structure of mesoporous silica materials, neither directly provides dynamical information related to their mass-transport characteristics such as the rate and anisotropy of diffusion for incorporated reagents and analytes. NMR methods provide such dynamical information of probe molecules within the mesostructure and also afford an important measure of the long-range organization and orientation of the mesopores.[37] However, NMR measurements provide averaged mass-transport information over relatively large sample regions.

1. 2 Single Molecule Tracking Methods Applied to Mesoporous Silica

Single molecule tracking (SMT) methods are now being widely employed in investigations of mesoporous systems.[38-48] In these studies, the mesoporous materials are doped to nanomolar concentrations with fluorescence probe molecules. The samples are then usually imaged under

wide-field illumination in an optical microscope and the motions, orientations and spectral emission characteristics of the individual molecules detected and followed in time.[49] An important advantage of SMT methods stems from their ability to directly revel the locations and motions of individual probe molecules incorporated within nanostructures with nm-scale spatial precision and millisecond time resolution. Adoption of SMT techniques for the characterization of mesoporous silica materials enables visualization of open mesopore structures, characterization of pore orientation and organization, as well as direct determination of the dimensionality and mobility of the probe's diffusive motions. Therefore, SMT provides a unique means to assess the local mass-transport and structural properties of nanostructured materials, while overcoming some of the limitations of more conventional methods.

Importantly, the capability to monitor molecular motions at the single-molecule level also enables the exploration and investigation of the materials heterogeneity. Assessment of spatial and temporal heterogeneities is essential for in-depth characterization and understanding of materials properties. Monitoring diffusion behavior of individual probe molecules in discrete nanochannels reveals the presence of local defects in the organized mesostructure. In addition, SMT data can be used to visualize the presence of distinct domains or grains having different pore orientations but similar levels of pore order, as has been demonstrated in previous studies of spin-coated mesoporous silica films.[50] Such organized domains were found to be nanometers to micrometers in size and were difficult to detect by SAXS measurements in which the beam size was much larger than the domain size.

Close study of the single molecule trajectories generated from the molecular diffusion at the single-pore and single molecule level afford significant fundamental insights on mesoporous silica materials and on the origins of their unique properties. For example, the angular distribution

of the mesopore orientation offers the average in-plane alignment of cylindrical nanochannels and a quantitative measure of materials order. SMT data also directly describe the aging-time dependence of pore organization within the flow-aligned mesoporous silica monoliths. In addition, the frame-to-frame mean square displacement (MSD) for each molecule in the SMT videos allows for estimation of mobility and transport rate of incorporated probe molecules.

SMT studies also reveal different diffusion behaviors of differently charged molecules in the flow-aligned, cylinder-shaped mesopores. The dimensionality of single molecule motion associated with the charge of probe molecules suggests the pore wall permeability is defined by the interaction between the guest molecules and the mesoporous host system as well as the inherent structure of the mesoporous silica materials.

1. 3 Objectives and Motivations of the Present Research

In the present dissertation, two important aspects of mesoporous silica materials preparation and properties are explored. In the first, the exact aging conditions that lead to highly ordered materials are identified. Secondly, the origins of silica wall permeability and solute diffusion anisotropy are investigated. SMT was employed (i) to characterize the in-plane alignment and order of cylindrical mesopores, (ii) to estimate diffusion rate of incorporated probe molecules, and (iii) to determine dimensionality of single molecule motions in flow-aligned surfactant-templated silica monoliths. The structural and mass-transport characteristics were quantitatively evaluated via a series of SMT experiments on thick mesoporous silica monoliths (70-150 μm in thickness) templated alternately by an ionic surfactant and non-ionic surfactant.

The characterization of mesoporous silicas having well-defined pore orientation and a high degree of order is required for several potential applications of mesoporous silica materials Through direct observation of the fluorescent probes diffusing within the cylindrical nanopores

with high spatial (ca. 50 nm) resolution at the single molecule level, SMT served as a unique tool for characterization of the order and organization of mesoporous systems incorporating one-dimensional (1D) nanostructures. Along with fabrication of aligned mesopores in a particular direction, quantitative estimation of the long-range nanopore alignment is specifically important for optimum performance in most applications.

On that account, systematic investigation on the mesopore order in the flow-aligned mesoporous silica monoliths were conducted by SMT as a function of sol aging time. Silica sols incorporating cylindrical micelles of an ionic surfactant, cetyltrimethylammonium bromide (CTAB) were injected into microfluidic channels with different aging times prior to filling of the microfluidic channels. SMT and SAXS were then utilized to explore mesopore organization. The results were used to obtain a quantitative measure of the 2D orientational order parameter and suggest a model describing the aging-time dependence of sol organization to achieve optimum pore organization. Studies of these phenomena are reported in Chapter 4 of this dissertation.

Another structural aspect of mesoporous silica materials to be investigated was the inter-connectivity and/or permeability of the mesopores. In many mesoporous silica systems incorporating cylindrical pores, it is assumed that the guest molecules are confined to and travel along one dimension within the pores templated by the surfactant micelles. However, evidence for permeability of the silica pore walls is readily found in the literature.[37, 51-54] One objective of this dissertation is to explore/identify the factors that affect the permeability of the pore walls to incorporated reagents or analytes. With knowledge of the material structure, such cross-wall porosity and permeability are often inferred from ensemble measurements. However, as mentioned above, SMT provides the means directly visualize the motions of the incorporated molecules. In fact, a recent work reported the electrophoretic mobility of charged and uncharged dyes within

aligned mesoporous silica.[47] The single molecular trajectories showed different levels of isotropic and anisotropic motion from probe molecules having different chemical structures and different charges. The results imply that pore wall permeability in the surfactant filled silica mesopores depends upon probe molecule properties (i.e., charge) and its interaction with regions nearest the pore walls.

In this dissertation, SMT experiments with use of differently charged fluorescence probes have been performed to elucidate the role of partitioning in governing the diffusion behavior of probe molecules in aligned, surfactant-filled mesoporous silica monoliths. Silica sol incorporating cylindrical micelles of a nonionic triblock copolymer surfactant, Pluronic F127 were injected into microfluidic channels to form the flow-aligned mesoporous silica monoliths. SMT and FCS were utilized to quantify diffusion behaviors of incorporated probes. Studies of the above phenomena are reported in Chapter 5 of this dissertation.

Chapter 2 - Surfactant-templated Mesoporous Silica Materials

The mesoporous molecular sieves are one of the most intensively studied and rapidly developed materials over the past few decades. The effort to create such organized materials found considerable boost after the discovery that micellar and lyotropic liquid-crystal phases can serve as templates for the organized porous structures at the meso-scales.[3, 55-57] Since then, many science and engineering disciplines have challenged to establish the design, synthesis, characterization, and utilization of the organized and structured materials.[1, 2, 58] Development of mesostructured and mesoporous materials have been carried out by employing a diversity of chemical compositions and provided various shapes and morphologies such as powders, thin films, fibers, or monoliths.[1, 2, 10] A high degree of versatility of these innovative materials also has been found in terms of structure, texture, and functionality.[1, 2, 59]

Surfactant-templated mesoporous silica materials have been introduced as chemically and thermally stable materials with well-defined and controllable structure. Preparation of these materials is generally accomplished by the sol-gel-process in which alkoxysilane precursors are hydrolyzed and condensed in the presence of amphiphilic surfactant molecules as structure directing agents. The properties of the silica material such as its structure, morphology and porosity are determined by the specific synthetic conditions employed including the concentration of silica precursor and surfactant, and polarity and pH of the sol.

In the present dissertation, characterization of surfactant-filled mesoporous silica monoliths comprising nanoscale cylindrical pores is mainly discussed. The sol composition should be carefully adjusted to produce well-aligned, open cylindrical pores. This chapter provides a review of the fundamentals behind fabrication of well-ordered and aligned mesoporous silica monoliths before stepping into the specific subject.

2. 1 Silica Sol-Gel Process

The sol-gel process is a method for producing solid materials from a colloidal suspension, generally obtained from the hydrolysis and condensation of alkoxysilane precursors. This process offers a low temperature route to homogeneous materials having unique and various compositions. Along with capability to obtain materials of diverse composition, it also possesses the ability to produce materials in powder (particle), film, fiber, and bulk monolith form. Such versatility leads sol-gel-derived materials to a prominent place in various areas of research. For the preparation of mesoporous silica materials, the sol-gel process provides a convenient and simple route to produce ordered materials having various structural and functional properties.[60] As in the general sol–gel process, the synthesis of mesoporous silicas involves the hydrolysis and condensation (polymerization) of the silica precursor.[61, 62] General acid and base catalyzed silica sol-gel procedures are shown in **Figure 2.1**.[63] Hydrolysis of a silicon alkoxide (e.g., tetraethoxysilane (TEOS), or tetramethoxysilicate (TMOS)) leads to the formation of silanol groups, Si-OH, and further reaction of the silanol groups forms Si-O-Si groups. As the hydrolysis and condensation proceed, the sol viscosity increases and a solid silica matrix, the gel is formed. During the sol–gel transition, the ratio of precursor silane to water, the pH and concentration of the catalyst, and aging and drying conditions have a critical effect on the final structure, morphology and porosity of the gel.[61, 62, 64-66] For example, acid catalyzed processes produce highly crosslinked networks (e.g., a continuous gel) of relatively low porosity, while in base-catalyzed preparations, colloidal particles are produced that subsequently form xerogels (dried gels) possessing higher porosity.[66]

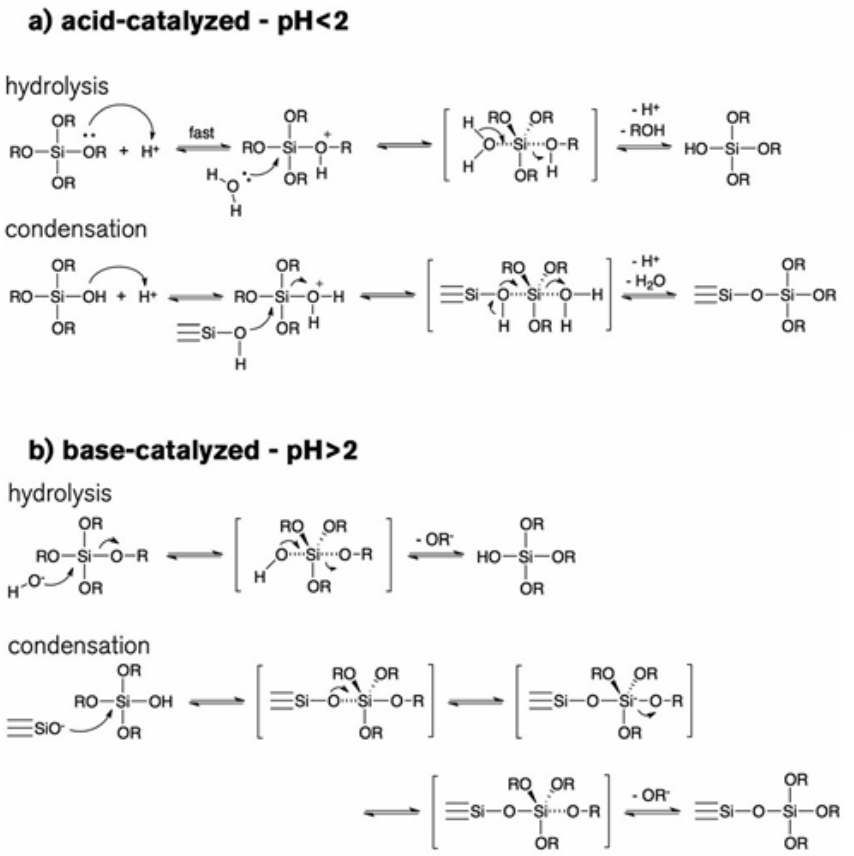

Figure 2.1 General mechanisms of hydrolysis and condensation of alkoxysilane precursors to form silica under (a) acid catalyzed conditions and (b) base catalyzed conditions. Condensation can produce either water or alcohol as a byproduct. Adapted with permission from Ref (62). Copyright © 2013, Royal Society of Chemistry.

2. 2 Preparation of Surfactant-Templated Mesoporous Silica

As the structural-directing agent, surfactant micelles play a significant role to form the organized structure of the mesoporous silicas. The mesoporous structure of the synthesized silica material is directly determined by the micellar structure of the surfactant under the synthetic conditions employed. Representative mesopore structures obtained by surfactant micelles are shown in **Figure 2.2.**[67] Under various sol compositions, the surfactant may form bilayers, spherical micelles, or cylindrical micelles. These micellar structures finally produce lamellar, three-dimensional (3D)

cubic or 2D hexagonal mesostructures that serve to template nanostructures (i.e., pores) in the fabricated silica materials.

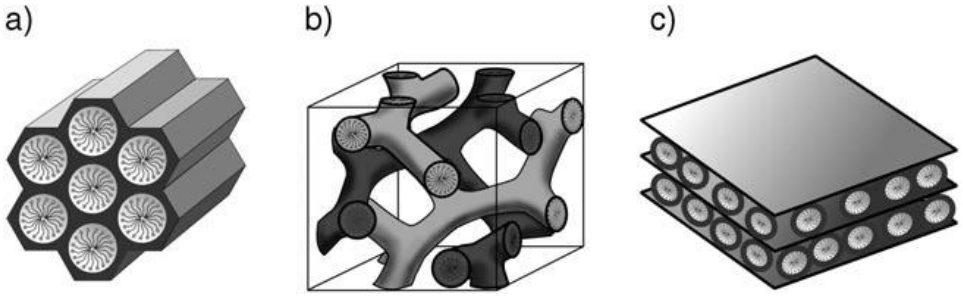

Figure 2.2 Structures of mesoporous M41S materials: a) MCM-41 (2D hexagonal, space group $p6mm$), b) MCM-48 (cubic, space group $Ia\bar{3}d$), and c) MCM-50 (lamellar, space group $p2$). Adapted with permission from Ref (66). Copyright © 2006 WILEY-VCH Verlag GmbH & Co. KGaA, Weinheim.

Formation of mesoporous silica is generally explained by a liquid crystal templating (LCT) mechanism as shown in **Figure 2. 3.**[4, 67] In-depth investigations into the formation procedure of the mesoporous structures have found that the LCT process involves two different routes. Firstly, in true LCT (Route (a) in **Figure 2.3**), the concentration of the surfactant is high enough to form the desired micellar structure under the prevailing conditions (temperature, pH). Thus, the inorganic phase (i.e., silica precursor) condenses around a stable lyotropic liquid-crystalline phase already formed in the initial sol.[4, 68, 69] On the other hand, the cooperative self-assembly (Route (b) in **Figure 2.3**) of surfactant molecules and inorganic species forms hybrid intermediate substances. The hybrid species act as independent composite entities and further self-assembly of these species allows a liquid-crystal phase to develop into the hexagonal, cubic, or laminar arrangement.[70-72] Besides concentration of the surfactant, the overall characteristics of the solution including polarity, pH, and concentration of the silica have a crucial influence on the formation of the hybrid composite species of the surfactant and the silica precursor. So, it is possible to form the micellar structure even at lower concentrations of surfactant molecules via the cooperative self-assembly

route. However, it is sometimes difficult to say which process is particularly involved in organization of the material. In the true LCT, the mesophase and organization of surfactant micelles are affected by addition of the silica precursor. Also, the surfactant molecules should form appropriate micellar structures before and/or during the cooperative self-assembly process to be finally arranged into the desired mesostructure. Hence, it is most likely that a combination of both mechanisms governs the construction of the mesostructured hybrid phases depending on the critical sol composition (e.g., silica and surfactant concentration, polarity and pH of the sol) and processing parameters (e.g., aging and temperature). Such a complicated formation mechanism provides a wide versatility on the materials properties while, on the other hand, the synthetic conditions have to be carefully chosen to obtain the desired materials for any specific fabrication or application.

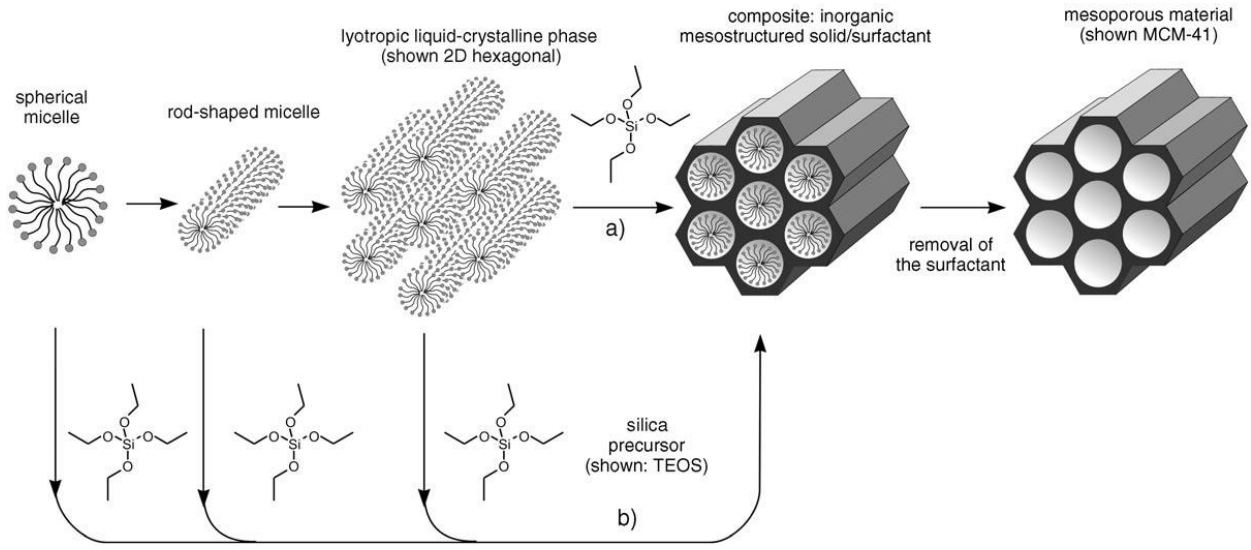

Figure 2.3 Formation of mesoporous materials by structure-directing agents: a) true liquid-crystal template mechanism, b) cooperative liquid crystal template mechanism. Adapted with permission from Ref (66). Copyright © 2006 WILEY-VCH Verlag GmbH & Co. KGaA, Weinheim.

2. 3 Influence of Synthetic Parameters

In the design and fabrication of mesoporous silica materials, it is important to know how the sol composition and processing conditions control the final mesopore structure and morphology. By changing the inorganic precursors and adjusting the synthesis conditions, mesoporous thin films,[73, 74] spheres,[75, 76] tubes,[77] fibers,[78] and monoliths[79, 80] have been prepared. Many studies of surfactant-templated mesoporous silicas in various systems have been reported to improve knowledge of the organized material.

The pore structure and size are two of the important parameters that define the properties of mesoporous materials. The pore structures of mesoporous materials are controlled by a cooperative process between the template and the growing silica polymer. Because aggregation of the surfactant in solution depends on its concentration and on the pH of the solution, the relative amount of silica source and surfactant in solution is a critical parameter for determination of the pore structure.[5] In addition to this, the packing capacity of the surfactant determined by its molecular structure is the main factor for the pore structure control.[81]

For example, addition of organic cosolvents , such as 1,3,5-trimethylbenzene (TMB) expanded the pore size of the mesoporous silica materials. The pore size could be adjusted by varying the heating temperature and time in the reaction solution.[82]

2. 4 Control of One-dimensional (1D) Mesopores

In this section, alignment and order of 1D nanochannels in mesoporous silica materials are discussed. The 1D nanochannels comprised of cylinder shape open pores are constructed by hexagonal arrangement of cylindrical surfactant micelles. Spontaneous self-assembly of the mesostructure provides locally ordered, organized pores. However, it is more difficult to achieve control over long-range pore order and orientation in a particular alignment. Many researchers

have explored a number of strategies to obtain preferential orientation of the channels and long-range order of the mesostructure. For instance, thermodynamic parameters were controlled in the solution phase preparation of mesoporous silicas by utilizing different templates, by adjusting the pH, and by using co-solvents or additives.[83-87] In addition, several methods have been developed for preparation of mesoporous thin films, including use of substrate modifications[31], external fields,[28, 35] and confinement in small space.[36, 88, 89]

2. 4. 1 Control of Mesopore Orientation in Solution Phase Synthesis

A synthesis of mesoporous silica materials in solution provides growth of mesoporous silica particles or fibers on nanometer to micrometer length scales. Experimental conditions including the precursor solution composition, temperature, and stirring rate govern fundamental variables, which control the size and morphology of mesoporous silica, such as rates of hydrolysis and condensation of the silica source, and the degree of the interactions between the growing silica polymer and the assembled templates. For example, by using a series of alkyl substituted silanes with various functionalities or changing its concentration, it was possible to generate diverse morphologies such as spheres, tubes, and rods of various dimensions, with precisely controlled particle sizes.[90] Mesoporous silica nanofibers also have been obtained by slow growth of the silica mesophase.[91-94]

As with control of particle morphology and size, the sol composition also affects the internal pore architectures of mesoporous silica particles and fibers. Considering the free energy balance for the formation of mesostructures may help reveal the influence of the synthetic conditions on the internal pore alignment. The free energy involved in the cooperative assembly of the surfactant molecules and silica species into well-defined nanoscale organic and inorganic domains includes several possible contributions; (i) van der Waals and electrostatic interactions at

the interface between surfactant and silica domains, (ii) interactions within the silica domains, (iii) van der Waals and conformational energies of surfactant hydrocarbon chains and/or van der Waals and electrostatic interactions of surfactant headgroups, (iv) the chemical potential of the surrounding solution phase, and (v) the solid-liquid interfacial energy between solid mesostructured products and the growth solution.[95] As a result of the intricate association of thermodynamic processes, the mechanism behind materials ordering is difficult to understand. Neverthless, carefully adjusted experimental conditions have been used to produce well-defined meporous silicas incorporating well-aligned pores.

Tan et al. reported fabrication of spherical silica particles with radially oriented nanopores. Their investigation suggested that ethanol plays a significant role as a cosolvent and as a low-dielectric constant solvent to bring about cooperative effects on micelle organization. Ethanol is expected to induce a decrease in the surface area per surfactant in the aggregates and therefore promote formation of low-curvature aggregates such as cylindrical micelles and bilayers.[83] As a result, mesoporous silica particles with radially oriented pores were synthesized at a large ethanol concentration.

Moreover for mesoporous silica particles, fabrication of hollow mesoporous silica spheres with highly ordered pores oriented perpendicular to the surface were demonstrated by using the water/oil emulsions,[84] air bubbles induced by ultrasonic irradiation,[85] and vesicles templated by fluorocarbon-hydrocarbon surfactants.[86] Regarding the arrangement of the surfactant micelles, some simulation studies suggested possible mechanisms for the ordering of surfactant aggregates.[96, 97] In the presence of either hydrophilic or hydrophobic walls, the mesostructure would align parallel to the wall. In contrast, if the wall has no preferential interaction, the mesophase would be aligned perpendicular to the wall.[96] Moreover, surface curvature has an

impact on the arrangement of the micelles.[97] In this point of view, the hollow (core) structure templates play an important role in the formation of ordered pores perpendicular to the surface as well as hollow cavity formation.

Under strongly acidic conditions, highly organized mesoporous silica nanofibers have been synthesized with cationic alkyltrimethylammonium and alkylpyridinium surfactants.[95] The nanofibers can possess hexagonally packed pores either aligned parallel to the fiber axis (i.e., a longitudinal pore architecture) or wound circularly around the fiber axis (i.e., a circular pore architecture). Systematic experiments were conducted to determine the fraction of the nanofibers with circular pore architectures among the overall nanofibers, as a function of the growth temperature. The result generally showed mesopores in the nanofiber tended to be aligned parallel to the fiber axis at lower temperatures while circular pore architectures were preferentially formed at higher temperatures. This is due to the variation of the free energy associated with the organization of amphiphilic surfactant molecules.[87] The temperature change can also affect the electrostatic interactions between charged surfactant molecules and silica species, and the chemical potential of the growth solution. The result from the minimization of the overall free energy was then manifested by formation of the nucleation sites for mesostructured nanofibers with different internal pore architectures.

2. 4. 2 Control of 1D Mesopores in Mesoporous Silica Films

One of the important features of sol–gel processing is that fluidic precursor sols can form solids with a diversity of shapes. So, it is possible to produce high quality mesoporous silica thin films easily by simple methods such as spin-coating. Development of mesoporous thin films is motivated by their possible applications as membranes, sensors, and surfaces for heterogeneous catalysis. Understandably, the precise control of the orientation of 2D hexagonal mesopores in the

films is needed for many practical applications. Such substances showed interesting anisotropic properties in the films on the macroscopic scale. For example, aligned fluorescent dyes incorporated in fully oriented mesoporous silica films showed anisotropic optical properties.[98] Highly uniaxial alignments of mesochannels were organized in the silica thin film with use of a rubbing-treated polyimide surface.[30, 99, 100] The mesoporous films with aligned cyanine dyes showed the maximum absorption when the incident polarization was parallel to the mesochannels (i.e., parallel to the long axis of the cyanine dyes).

As with 1D mesochannels aligned with their long-axis running parallel to the substrate, the 1D mesochannels aligned perpendicular to the substrates also have practical importance. The vertical 1D nanochannels can act as a barrier with controlled permeation for analytes without lateral diffusion. Different methods were investigated to obtain fully oriented films, using the template approach. For example, Teramae et al. reported a demonstration of size-selective molecular transport across the perpendicular 1D mesochannels inside porous anodic alumina (PAA) membranes.[101]

In this section, several approaches/techniques are introduced for the control of 1D mesochannels in mesoporous silica films.

2. 4. 2. 1 Orientation by Confinement

The alignment of mesopores in 2D hexagonal mesoporous materials is significantly affected by confinement of the materials on short length scales. In a confined space, the mesochannels tend to be aligned in the most thermodynamically stable direction. Porous anodic alumina (PAA) membranes are the most widely used substrate to guide mesopore alignment in a particular direction. In the synthetic approach, evaporation of a precursor solution penetrated into the matrices of PAA leads to formation of the mesoporous silica films. The direction of the

mesochannels in this process strongly depended on the synthetic conditions.[102-106] For example, a cationic surfactant such as CTAB provided mesochannels aligned along the long axes of the PAA channels (i.e., columnar orientation).[101] The mesochannels were oriented perpendicular to the PAA channels and circularly packed like stacked donuts with use of nonionic surfactants as the structural directing agents.

Confinement within small structures fabricated by electron-beam lithography is also very effective for orientation control of mesochannels, as demonstrated by Wu and Kuroda et al.[107] Their results show that the widths of the mold strongly affect the final orientation of the mesochannels. For the same thickness of the molds, 1D mesochannels were highly aligned along the long axis of molds of 0.5 mm widths. With a decrease in the width down to 0.1 mm, the mesochannels were less ordered and were at least partly oriented in the perpendicular direction.

The Brauchle group has demonstrated a simple synthesis method for well-aligned 2D hexagonal mesoporous silica thin films using PDMS microgrooves.[88] Well-defined macroscopic alignment of the mesochannels was achieved by confinement in PDMS microgrooves. Further investigation of the influence of experimental conditions found that the alignment of the mesochannels can change from parallel to perpendicular depending on the height within the microgrooves.

2. 4. 2. 2 Spontaneous Pore Orientation on Modified Substrates.

The reciprocal interaction between surfactants and substrates induces the spontaneous self-assembly of surfactants oriented in particular directions without external forces. Epitaxial growth is typically utilized to selectively grow a single-crystal layer. The Ozin[108] group and the Aksay[109] group reported mesoscale epitaxial-like growth by using anisotropic surface structures of mica and graphite substrates. The in-plane arrangement of aligned mesochannels reflected the surface

structure through the interactions between the substrate surface and the silicate-surfactant species. Si (110) substrates were also employed by Miyata and Kuroda[31] to prepare uniaxially aligned mesoporous silica films. In this research, the 2-fold symmetry arrangement of the silicon atoms on the Si (110) surface determined the preferred alignment of the mesopores. The same group also achieved the control of mesochannels in films by using substrates that were previously coated with a rubbing-treated polyimide film.[30, 99, 100] Uniaxially oriented mesopores were supposed to be induced by the hydrophobic interactions between the alkyl chains of surfactants and elongated polymer chains. Another useful technique for control of 1D mesochannel alignment is the photo-orientation technique. Seki et al. demonstrated the control of mesochannels using the previously aligned polymer prepared by patterning using photo-masks.[110] The result showed various orientations of the 1D mesochannels within the same film by using different patterning.

A long-range ordering of mesopores oriented perpendicular to the substrate was achieved by utilizing PAA substrates with straight holes (around 100 nm in diameter).[111-113] From SEM and TEM observation, the standing mesochannels are epitaxially generated along the PAA holes[111] and grew from the interface between the holes and the continuous silica region above the PAA holes. The oriented mesochannels within the PAA holes served as an initiator for the forced evolution of the aligned mesochannels in the silica film above the PAA holes. As a result, the mesopore alignment in the continuous region exhibited similar mesochannel orientation as that inside the PAA holes. Furthermore, This concept was employed to prepare perpendicularly oriented P123-based mesochannels on PAA substrates with conical holes.[112]

2. 4. 2. 3 Application of External Fields

The utilization of external fields such as electric fields and magnetic fields can induce alignment of mesopores in a particular orientation. For example, Chmelka and coworkers applied

a strong magnetic field to control the alignment of 1D mesochannels.[35] Under a strong, anisotropic magnetic field, uniaxial self-assembly of rod-like surfactants micelles was induced along the magnetic field direction.[114, 115] While heating the samples above the isotropic-to-anisotropic phase transition, followed by slow cooling, unpolymerized hexagonal silicate-surfactant lyotropic liquid crystals were oriented under the influence of the field. Thus, the long-axis of the tubular micelles was aligned parallel to the magnetic direction. Preparation of perpendicular 1D mesoporous films has also been demonstrated by similar methods.[116-118] Mesoporous silica films were prepared by casting the ethanolic silicate-surfactant precursor under a strong magnetic field. During evaporation of the precursor sol, the magnetic field was applied either perpendicular or parallel to the substrate. Cross-sectional TEM images and XRD measurements found that the mesochannels were indeed aligned parallel to the field direction.

Electric fields have also been used by the Walcarius group to create vertically-aligned mesopores on an underlying electrode surface.[28] This research showed synthesis of mesoporous silica films with perpendicular 1D mesochannels on various conductive substrates under potentiostatic control. The mesopores in the silica films were found to be perfectly aligned perpendicular to the substrate. However, electric field strength should be limited to avoid degradation of the materials and it is difficult to obtain longer-range alignment due to the limited electric field strength.

2. 4. 3 Flow-alignment in Mesoporous Silica Monoliths

Efforts to develop orientationally ordered mesoporous silica solids has produced well-ordered and well-aligned mesostructured silica thin films, fibers and even particles by employing many different approaches mentioned above. Despite successful progress in the synthesis of such mesoporous silica materials, some of techniques are not well suited to the synthesis of well-defined

macroscopic monoliths with highly ordered mesopores, because many of the driving forces for pore alignment such as surface interactions and thermodynamic energy balancing do not extend into the bulk. However, a shear stress still provides the simplest and most effective way to induce macroscopic alignment in a bulk silica monolith.

Su et al. applied air flow to guide the orientation of mesochannels in multilayer films.[119] The surfactants in the silica precursor sol could be enriched and form tubular-shaped micelles surrounded by silica species with evaporation of ethanol under hot air flow. High speed air flow also leads to rapid motion of the droplet,[120] generating great shear force. The micelles were then anisotropically arranged along the air-flow direction under the shear force induced by the air flow.

Melosh el al. demonstrated fabrication of mesoscopically ordered bulk silica with a high degree of macroscopic alignment using capillary flow and parallel plate shearing.[34] To achieve a shear-induced alignment of cylindrical mesopores, evaporation of alcohol produced by hydrolysis of silica precursors is require to form 2D hexagonally arranged cylindrical surfactant micelles. Transmission XRD studies and uniform birefringence from products identified highly aligned mesostructures along the shear direction.

2. 5 Pore Wall Permeability

The organized, well-aligned nanostructures within mesoporous silica materials incorporating cylindrical open pores provide well-defined 1D pathways for the mass transport of incorporated reagents or analytes. These well-defined and simple structures attract considerable interest as a host system for applications in catalysis, drug release and separations. As a result, it is essential to investigate the parameters affecting the diffusion characteristics of host molecules within the mesoporous systems. The comprehensive study of mass transport processes within

these materials would facilitate the successful preparation and appropriate functionalization of the mesopores for their possible applications.

The anisotropic diffusion of incorporated probe molecules is suggested on the basis of the materials structure. Several studies have also reported observing 1D molecular diffusion in the mesopores using SMT experiments.[39-43, 121] The diffusive motions of the probe molecules frequently follow the well-defined structure of the mesopores. In the SMT studies, the 1D motion reflects the organization of the cylindrical mesochannels. Isotropic diffusive trajectories are often assumed to imply disorder of the nanostructures brought about by, for example, local defects. In recent research from the Brauchle group, different diffusion modes (i.e., isotropic and anisotropic diffusion) based on charge of the guest molecule were revealed.[47] The results demonstrated charged and uncharged probe molecules traveled different pathways in the organized mesostructure. The charged molecules showed isotropic diffusive motions that likely arose by probe molecules crossing between neighboring pores. In contrast, the uncharged molecules depicted 1D diffusion along the aligned, 1D nanochannels. This result may indicate very interesting features of the diffusion behaviors of incorporated reagents or analytes within the mesoporous materials.

The inherent microporosity of the mesoporous silica materials may lead to permeability of the silica pore walls, providing isotropic pathways for the molecular transport. Micropores in the pore wall may arise as a result of the surfactant-templating process. For example, the well-known core-corona structure of $EO_mPO_nEO_m$ triblock copolymer micelles[122-125] are composed of hydrophobic PO blocks and relatively hydrophilic EO blocks. In the formation of mesoporous silica materials templated by triblock copolymer micelles (e.g., Pluronic F127), the silica framework may be penetrated by the EO blocks composing the corona region of the micelles. The

penetration of the EO tails into the silica matrix may therefore produce micropores, voids or small defects that permit passage of some molecules through the pore walls.

Cross-wall transport and release of incorporated dye molecules have also been reported for CTAB-templated materials.[53, 54] The mesoporous system chosen for these studies comprised a unique pore organization,[126] in which the mesopores were coiled around the axis of symmetry. The loss of dye from the mesoporous fibers was observed under a microscope.[53] The results suggested transport of the dye in the radial direction (perpendicular to the long-axis of the mesoporous fiber), which requires channel-to-channel diffusion or cross-wall transport. Further investigations were also conducted on the coiled pore systems of microparticles.[54] **Figure 2.4** represents the schematic structure of these microparticles. The result from this research confirmed the release of probe molecules by cross-wall transport. Such transport provides support for the conclusion that the guest molecules escape from the mesoporous system through micropores connecting the mesopores.

In addition, distinct diffusion behaviors of uncharged and charged molecules indicated that the interaction between the guest molecules and the host mesoporous system plays a significant role in pore wall permeability. Host-guest interactions may affect the selectivity of diffusion of incorporated guest molecules. In this dissertation, diffusion behavior of charged and uncharged dye molecules within the F127 templated mesoporous monoliths are discussed in Chapter 5. Different diffusion modes (i.e., isotropic and anisotropic) suggested dissimilar pore wall permeability of charged and uncharged probe molecules, which is governed by the partitioning of dye molecules into the different regions of the cylindrical micelles consisting hydrophilic exterior and hydrophobic core.

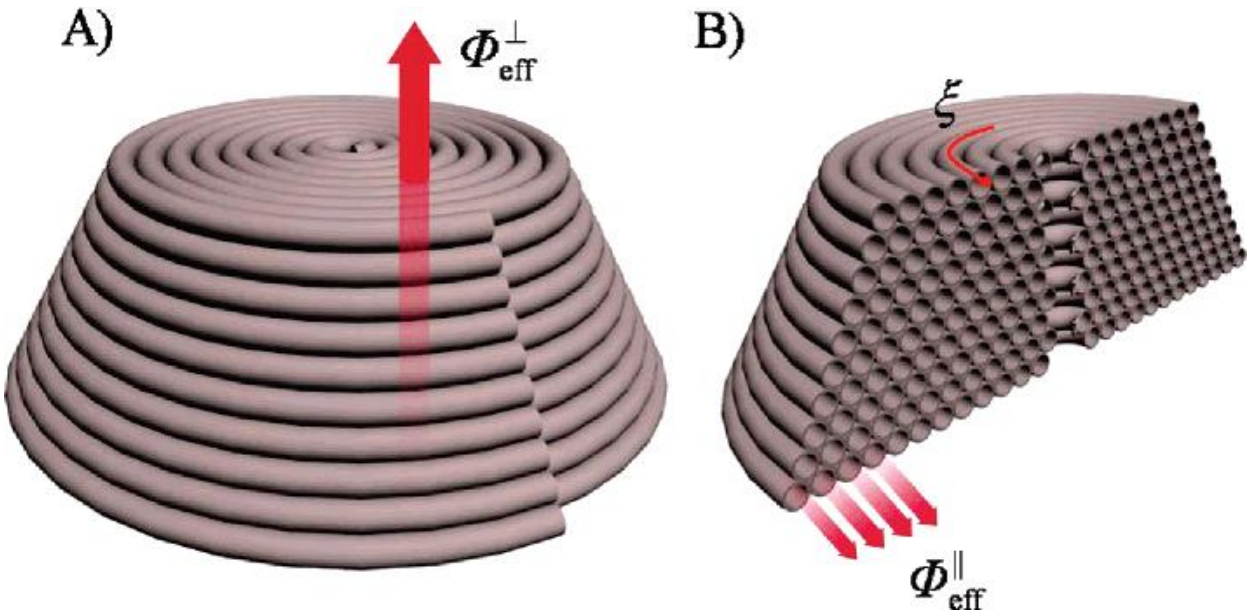

Figure 2.4 Schematic structure of a conelike particle produced in an SBA-3-like synthesis. Release from a whole particle is determined by cross-wall transport connected with the flux $\phi_{eff}^{\perp}$ and the effective diffusion coefficient $D_{eff}^{\perp}$. (B) After cutting a particle in half, diffusion along the pores becomes effective ($\phi_{eff}^{\parallel}$ associated with $D_{eff}^{\parallel}$) with diffusion paths along ξ. Reprinted with permission from Ref (53). Copyright 2007 American Chemical Society.

Chapter 3 - Experimental Considerations

This chapter describes the fabrication of flow-aligned mesoporous silica monoliths studied throughout this dissertation. It also covers the techniques and data analysis procedures used in the characterization of the samples. Chapters 4 and 5 give further detail on experimental setups and sample preparation conditions.

3. 1 Silica Sol Preparation: Formation of the Hexagonal Mesophase

In this dissertation, two different surfactant molecules were used to construct highly ordered cylindrical mesopores in the mesoporous silica monoliths, aligned by flow-induced shear. First, an ionic surfactant, CTAB (cetyltrimethylammonium bromide, $(C_{16}H_{33})N(CH_3)_3Br$) was employed to investigate the aging-time dependence of mesopore orientation and a non-ionic surfactant, Pluronic F127 was used as the structural directing agent for studies of the dimensionality of diffusion in flow-aligned surfactant-templated mesoporous silica monoliths. The chemical structures of CTAB and F127 are shown in **Figure 3.1**.

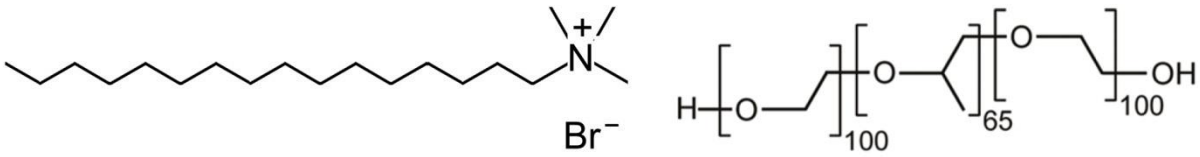

Figure 3.1 Chemical structures of (left) CTAB and (right) Pluronic F127 surfactants.

For both cases, the formation of aligned mesopores was achieved via flow-induced orientation of cylindrical surfactant micelles. So, the hexagonal mesophase of cylindrical micelles was formed by using a high concentration of surfactant and removal of the alcohol produced by hydrolysis of the silica precursor (i.e., methanol from hydrolysis of TMOS). Thus, sols prepared

under carefully selected composition fall within the hexagonal region of the phase diagrams shown in **Figure 3.2**.

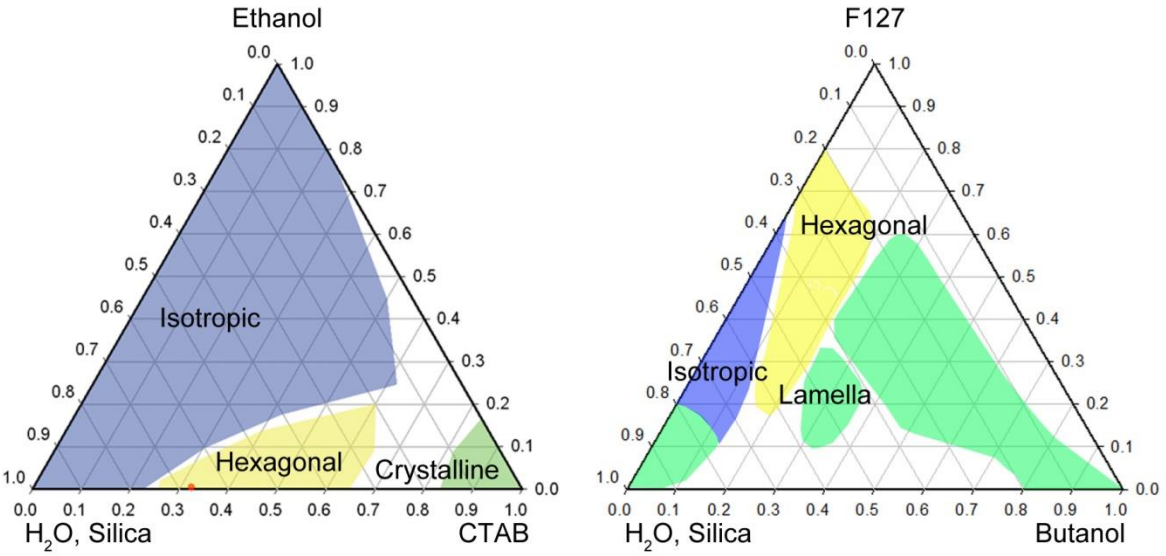

Figure 3.2 (left) The ternary CTAB/water/ethanol phase diagram[127] and (right) phase diagram for F127/water/butanol mixtures[48]. The sol compositions were adjusted to form hexagonal mesophase in both phase diagrams.

3. 2 Perylene Diimide (PDI) Dyes

In the present work, diffusive motions of a series of charged and uncharged perylene diimide (PDI) dyes were followed by SMT as a means to explore the physical properties of the surfactant-filled cylindrical mesopores. Diffusion coeffcients of these dyes were also estimated by FCS studies of Pluronic F127 templated mesoporous silica monoliths. The dyes employed include an uncharged PDI, N,N′-bis(octyloxypropyl)-perylene-3,4,9,10-tetracarboxylic diimide, and two doubly charged PDIs, N,N′-bis(3-sulfonatopropyl)perylene-3,4,9,10-tetracarboxylic diimide and N,N′-bis(2-(trimethylammonio)ethyl)-perylene-3,4,9,10-tetracarboxylic diimide. All dyes were synthesized in house.[128] **Figure 3.3** depicts the chemical structures of the PDI dyes.

a)

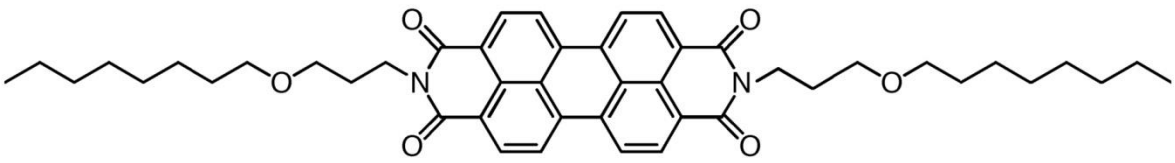

N,N′-bis(octyloxypropyl)-perylene-3,4,9,10-tetracarboxylic diimide

b)

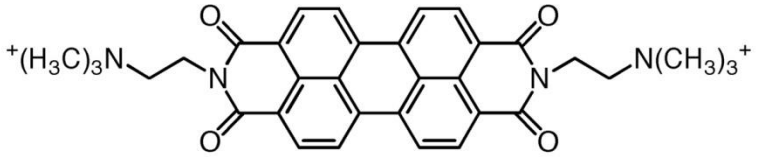

N,N′-bis(2-(trimethylammonio)ethyl)-perylene-3,4,9,10-tetracarboxylic diimide

c)

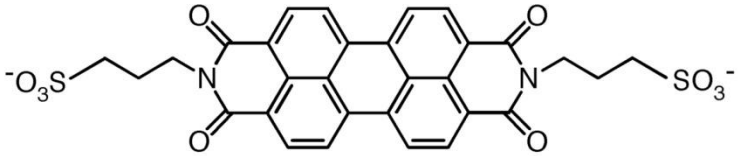

N,N′-bis(3-sulfonatopropyl)perylene-3,4,9,10-tetracarboxylic diimide

Figure 3.3 Chemical structures of the uncharged (a), cationic (b), and anionic (c) PDI dye molecules employed in single molecule tracking and FCS experiments.

3. 3 Instrumentation

3. 3. 1 Two-dimensional (2D) Small Angle X-Ray Scattering (SAXS)

The morphology and orientation of the cylindrical nanostructures in monoliths was assessed by 2D SAXS. In the general, the 2D SAXS technique provides complete information on average domain and nanopore structures, spacing and orientation over macroscopic sample regions, throughout the entire thickness of the bulk materials. The morphology of the nanoscale structure is probed by collecting the variation of elastic X-ray scattering intensity at very small angles (2θ < 2º) from an X-ray beam incident on the sample. The scattering angle (θ) directly describes the spacing/distance (d) between the periodic structures (domains or pores) by Bragg's law:

$$2dsin\theta=n\lambda \qquad \text{(Eq. 3.1)}$$

where λ is the wavelength of the X-rays (i.e., λ = 1.54 Å in this dissertation) and n the order of the scattering peak. When a 2D detector is employed in the SAXS measurements, the anisotropy of the mesostructure and thus, the order and orientation of cylindrical mesopores can be estimated. However, a broad illumination of X-ray beam provides spatially averaged information and is not sufficient to describe the local structure and morphology as well as sample heterogeneities (e.g. defects) in the materials.

The 2D-SAXS instrument used in this dissertation employed a rotating anode Cu (λ = 1.54 Å) source and a multi-wire area detector provided 2D features of X-ray scattering. A large distance (59.5 cm) between the sample holder and the detector was used to record very small angle scattering (**Figure 3.4**).

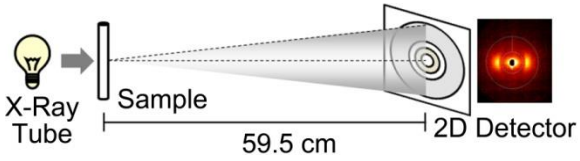

Figure 3.4 Schematic of a 2D-SAXS instrument with its major components: an X-ray source, sample and a 2D detector. The SAXS data are collected simultaneously for small scattering angles (2θ) and the anisotropic pattern of scattering intensity indicates an ordered and aligned mesostructure of the sample.

3. 3. 2 Wide-field Fluorescence Microscopy

All SMT measurements were performed on a wide-field fluorescence microscope. A typical setup is shown in **Figure 3.5**. This microscope set-up consists of a blue diode laser emitting 488 nm light as an excitation source, suitable optics including optical filters, a dichroic mirror or polarizers, a high magnification and high numerical aperture (NA) objective lens (100X magnification, 1.49 NA) and a highly sensitive electron multiplying (EM) CCD-camera for detection of the signal. Utilization of the high magnification and high NA objective lens enables almost diffraction-limited detection of single molecule spots and provides for efficient collection

of the fluorescence emission from individual fluorescent probe molecules. The EM-CCD detector afforded high-speed data collection (e.g., 0.042 sec/frame in this dissertation) with sufficient signal-to-noise (S/N) ratio for detection and tracking of single molecule fluorescent probes. Combined with broad illumination, high-throughput and sensitive data acquisition allows the dynamics of a number of single molecules within nanoscale structures to be recorded simultaneously for μm-scale wide sample areas (e.g. 18.75 μm x 18.75 μm in the present works).

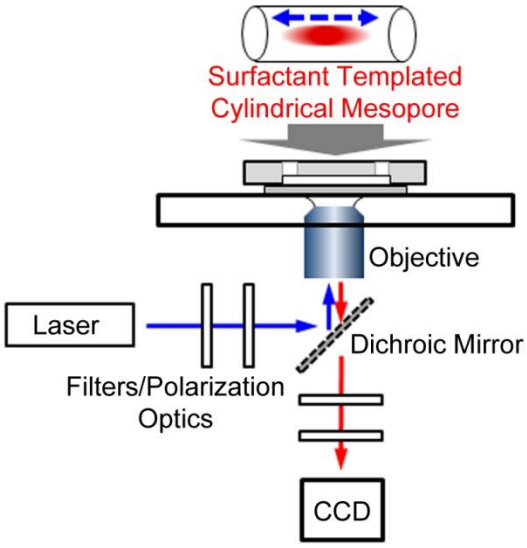

Figure 3.5 Schematic of wide-field microscope used for single molecule imaging.

For SMT imaging of the mesoporous silica monoliths, total internal reflection fluorescence (TIRF) mode measurements were required to minimize the background fluorescence intensity. TIRF allows for fluorescence excitation in a narrow region close to the glass-sample interface. A typical objective-based TIRF scheme is shown in **Figure 3.6**. In TIRF imaging, the incident angle (θ_{inc}) of the excitation light is adjusted to produce total internal reflection at the glass-sample interface (i.e., $\theta_{inc} > \theta_{crit}$) when the refractive index of the sample (n_s) is smaller than that of the glass (n_g): [129, 130]

$$\theta_{crit} = sin^{-1}\left(\frac{n_s}{n_g}\right) \qquad \text{(Eq. 3.2)}$$

When total internal reflection occurs, an evanescent wave of the incident laser excites the fluorescence probe molecules within a nm-scale thin layer adjacent to the glass-sample interface. The penetration depth (d_p) of the evanescent wave is governed by decay of the evanescent fields and can be estimated using:[129, 130]

$$d_p = \frac{\lambda}{2\pi}\left[n_g^2 \sin^2\theta - n_s^2\right]^{-1/2} \qquad \text{(Eq. 3.3)}$$

where λ is the wavelength of the light source. Typically, d_p is between 30 to 300 nm depending on the incident angle (θ_{inc}). For example, the d_p of the evanescent wave produced by a 488 nm laser at the interface of the glass substrate (n_g = 1.54) and CTAB sample (n_s = 1.41) with θ_{inc} of 75.4° is ~ 160 nm ($1/e^2$).

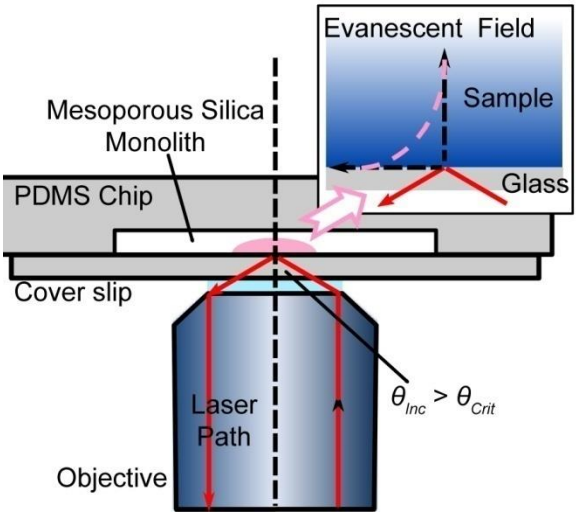

Figure 3.6 Schematic of objective-based TIRF imaging mode. The pink dotted line in the inset image shows the decay of the evanescent field.

3. 3. 3 Confocal Fluorescence Microscopy

A confocal fluorescence microscope (**Figure 3.7**) was used to study the diffusion behavior (i.e., diffusion rate) of charged and uncharged PDI dyes. This home-built microscope setup includes a blue diode laser (488 nm), as an excitation source, mirrors, high NA objective lens (NA

= 1.3), a dichroic mirror, and a filter set to select emission of the desired wavelength; the emission was subsequently detected by an avalanche photo diode (APD). A closed-loop piezoelectric positioner was employed to prevent focus drift and a pinhole (50 μm diameter) defined the detection volume. From the known diffusion coefficient of rhodamine 123 in aqueous solution (e.g., $D_{R123} = 4.6 \times 10^{-6}$ cm^2/s), the dimensions of the detection volume were calibrated.

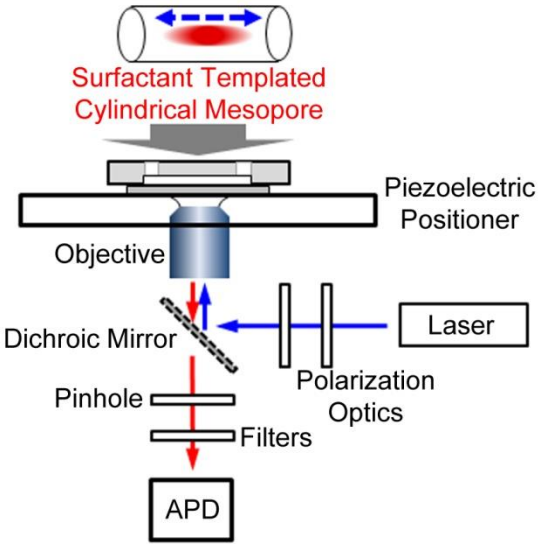

Figure 3.7 Schematic of confocal fluorescence microscope set-up used for wide-field single molecule imaging.

3. 4 Single molecular Trajectory Analysis

3. 4. 1 Orthogonal Regression

Analysis of the single-molecule motions in the wide-field fluorescence videos offers information on mass transport dynamics of molecules within the nanostructures as well as detailed structural features of the materials. The comprehensive analysis of single-molecule diffusion is commonly accomplished by investigating the single molecule trajectories of the detected spots. The single molecule trajectories are produced by linking the single molecule spots frame-by-frame in a video and depict the diffusive motions of each molecule. In the present dissertation, orthogonal

linear regression methods[50] were utilized for quantitative analysis of the individual trajectory segments.[131-133] Fundamentally, the orthogonal regression analysis assumes that the trajectories are truly 1D without any detectable curvature. By fitting the single-molecule trajectories to linear functions, this analysis allows for a more quantitative assessment of a number of parameters. For example, this analysis quantitatively provides the in-plane orientation of each 1D trajectory segment, the best fit (*x*,*y*) locations of the single molecule spot in each trajectory, and estimates of angular and positional errors in these parameters. These parameters can also be used to determine mobility and dimensionalities of the diffusive motion of individual molecules.

With an assumption that x and y positions are measured to similar levels of precision, . the measured position (x_i, y_i) can be written as:

$$x_i = X_i + \delta_i \quad \text{(Eq. 3.4)}$$

$$y_i = X_i \tan\theta + \delta_i \quad \text{(Eq. 3.5)}$$

where X_i represents the best estimate of the actual *x* position of the molecule and δ_i is the error in measuring the position of the molecule. θ corresponds to the angle (-90° to 90°) of the trajectory segment with respect to the horizontal direction (x-axis) in the video frames and thus represent the in-plane orientation of the diffusive motion. While the best-fit line ($Y_i = X_i \tan\theta$) is obtained by finding $\tan\theta$ for a minimum sum of the squared residuals (SSR) between x_i and X_i, and y_i and Y_i, the errors in determining x_i and y_i for each molecule along each trajectory provides a measure of the positioning error across the entire length of the trajectory. The variance in the position measurement along each trajectory is given by:[132, 133]

$$\sigma_\delta^2 = \frac{S_{yy} - 2S_{xy}\tan\theta + S_{xx}\tan^2\theta}{1 + \tan^2\theta} \quad \text{(Eq. 3.6)}$$

where,

$$S_{yy} = \frac{1}{n}\sum_{i=1}^{n} y_i^2,\ S_{xx} = \frac{1}{n}\sum_{i=1}^{n} x_i^2 \text{ and } S_{xy} = \frac{1}{n}\sum_{i=1}^{n} x_i y_i \quad \text{(Eq. 3.7)}$$

Also, the motional variance in the molecular position along 1D trajectories is found by:

$$\sigma_R^2 = \frac{S_{xy}}{\tan\theta}(1 + \tan^2\theta) \qquad \text{(Eq. 3.8)}$$

While σ_δ^2 can actually reflect the width of corresponding trajectory by describing the total deviation of the trajectory from a 1D model, σ_R^2 affords a measure of the trajectory length.

3. 4. 2 Trajectory Angle Order Parameter

A common ensemble parameter used to quantify materials order is the order parameter. In general, individual pore orientations can be described as the angular deviations of the nanochannels from the most preferred pore direction of the material (or selected region). The Legendre polynomials can provide a quantitative measure of the angular deviations, and the average of the second Legendre polynomial is employed to estimate the orientational order parameter in 3D systems for materials with cylindrical symmetry. So, the ensemble order parameter (*S*) is universally defined as $S = \frac{1}{2}(3\langle\cos^2(\Delta\theta)\rangle - 1)$, where $\Delta\theta$ represents the angular deviation of individual cylindrical pores and $\langle\ \ \rangle$ denotes the average within a selected population, region or sample domain. Consequently, the value of *S*, the 3D ensemble order parameter, ranges from -1/2 to 1, where $S = 1$ for perfect ordering of the populations, and $S = 0$ indicates a totally isotropic organization of the pore structure. The perfect ordering of the structure orthogonal to the expected preferred plane corresponds $S = -1/2$, theoretically. For the trajectory analysis in the present single molecule tracking studies, the 2D analog of the 3D order parameter was employed. The 2D order parameter is defined as $\langle P\rangle = 2\langle\cos^2(\Delta\theta)\rangle - 1$, where $\Delta\theta$ represents the angular deviation in the direction of the individual trajectories, θ from $\bar{\theta}$. The latter is the mean trajectory orientation in a given sample region. Resulting value of $\langle P\rangle = 1$ for perfectly ordered populations, and $\langle P\rangle = 0$ for totally disordered populations are obtained.

The order parameter can successfully quantify the materials order, and so is being widely used especially for studies on the nematic mesophases. Single molecule methods presently represent the only means to follow mass transport at the single molecule and single nanostructure levels. In this case, the single molecules represent tracers that "map" the open nanostructures and reveal their abilities to confine and guide mass transport. The trajectory data obtained therefore provide valuable information on materials order specifically as it relates to mass transport. Most importantly, this information is obtained at the single nanostructure level, allowing for the complete distribution of open channel alignments to be assessed. Therefore, it is possible to describe the materials order in more detail than is provided by the ensemble order parameter alone.

Chapter 4 - Single Molecule Tracking Studies of Flow-Aligned Mesoporous Silica Monoliths: Aging-Time Dependence of Pore Order[1]

4. 1 Introduction

Surfactant template mesoporous silica materials find a range of possible applications in catalysis, chemical sensing, separations and molecular sieving.[3, 4, 134, 135] Such materials are prepared by the hydrolysis and condensation of alkoxysilane precursors in the presence of structure-directing agents such as surfactant micelles. Depending on the synthetic conditions employed, materials incorporating spherical, planar, or cylindrical surfactant structures organized in cubic, lamellar or hexagonal configurations can be produced.[134, 136] Mesoporous materials derived from hexagonally arranged cylindrical micelles are most common and are the subject of this report. Polymerization of the inorganic silica matrix around these micelles produces rigid glass materials incorporating hexagonally organized cylindrical mesopores.

Pore alignment is largely uncontrolled in most such syntheses, resulting in "polycrystalline" materials incorporating randomly aligned domains of otherwise well-organized pores.[50] However, optimum performance in many of their applications (i.e., membranes for chemical separations) requires the fabrication of pores aligned along a particular pre-defined direction. As a result, several research groups have developed methods for preparation of aligned mesoporous materials.[135, 136] For example, Chmelka and coworkers demonstrated that exposure of a surfactant-templated sol to a strong magnetic field[35] produced aligned mesopores upon gelation of the sol.

[1] Reprinted with permission from (Park, S. C.; Ito, T.; Higgins, D. A. Single Molecule Tracking Studies of Flow-Aligned Mesoporous Silica Monoliths: Aging-Time Dependence of Pore Order. J. Phys. Chem. B 2013, 117, 4222-4230.). Copyright (2013) American Chemical Society.

Walcarius, et al. have described electrochemically-assisted self-assembly methods for synthesizing silica films incorporating 1D mesopores oriented perpendicular to an underlying electrode surface.[28, 29] Interactions with substrate surface structures have also been employed to produce aligned mesopores. Representative methods include depositing surfactant-templated sols on rubbed polyimide films,[30] on single crystal substrates,[31] and on lithographically-prepared surface nanostructures.[107] Some of the simplest methods for obtaining aligned mesoporous materials, however, involve the injection of surfactant-containing sols into confining structures,[135] such as the pores of anodic alumina membranes,[32, 33] glass capillaries[34] or microfluidic channels.[88, 89] In capillaries and microfluidic channels, micelle (and pore) alignment often results from shearing of the surfactant mesophase.[69]

The physical properties of mesoporous materials are commonly assessed by electron microscopy (EM),[4, 28-34] small-angle X-ray scattering (SAXS) [4, 28-35] and by NMR.[4, 28-35] EM provides high-resolution visual evidence of local mesopore structure and orientation but requires significant effort to detect long-range organization. It also involves placing the sample under vacuum, and hence, removal of any solvent. Likewise, SAXS affords detailed physical insights into mesopore morphology and alignment, but the data obtained largely reflect average materials properties. Unfortunately, neither EM nor SAXS provides direct data on the mass-transport characteristics of the materials. NMR methods provide an important route to obtaining such dynamic information (i.e., rate and anisotropy of probe diffusion) along with data on long-range mesopore alignment. However, like SAXS, the information obtained is averaged over relatively large sample regions.

It has recently been demonstrated by the Brauchle group[39, 88, 121, 137] and others[40, 50] that single molecule tracking (SMT) methods[138] can be used to directly observe the motions of

individual fluorescent molecules diffusing within discrete nanometer-sized cylindrical channels of surfactant-templated mesoporous silica. Identical experiments on similarly-structured materials are now also being reported.[45, 122] SMT methods represent important tools for the investigation of mesoporous systems because they allow for (i) materials structure to be visualized,[50, 88] (ii) the occurrence of 1D mass transport to be directly observed, (iii) molecular mobility within *individual* pores to be quantified, and (iv) the alignment and organization of single mesopores to be assessed. While such methods have been used previously to qualitatively assess materials organization, recent work from our lab shows that quantitative information on mesopore orientational alignment and ordering can be obtained via orthogonal regression analysis of single molecule trajectory data.[50] We have used these methods to characterize mesopore alignment and order in spin-coated silica films,[50] the alignment of cylindrical surfactant micelles in lyotropic liquid crystal mesophases[122] and the alignment of cylindrical domains in block copolymer films.[46] Importantly, the ability to observe molecular motions at the single event level also enables investigation of materials heterogeneity. For example, in our studies of spin-coated silica films, SMT data revealed the presence of distinct domains having different average pore orientations but similar levels of pore order.[50] Such information would be lost in SAXS measurements, when the domain size is smaller than the incident beam size.

In this study, macroscopically aligned mesoporous silica monoliths were prepared by flow-alignment of surfactant-templated silica sols in etched glass microfluidic channels. Cetyltrimethylammonium bromide (CTAB) was employed as the surfactant and was present at sufficient concentration to form the hexagonal mesophase in the precursor sol. Mesopore alignment and organization in each sample was assessed by both SMT and SAXS. The primary goal of these investigations was to characterize mesopore organization as a function of sol aging

time (i.e. the time between sol preparation and injection into the microfluidic channel). A fluorescent perylene diimide dye (OPDI) (structure shown in **Figure 3.3**) was employed as the probe molecule. Wide-field fluorescence videos depicting OPDI motions at the single-molecule/single-pore level revealed a predominance of 1D diffusion. Orthogonal regression analysis of the trajectory data provided quantitative information on the in-plane orientation of individual pores. The degree to which the pores were aligned along the flow direction was assessed in each sample, as was mesopore order, which was quantified by calculation of a 2D order parameter from the individual trajectory angles. The results obtained were compared to those from SAXS experiments. Taken together, the results showed that materials prepared well before gelation of the sol incorporate large monodomains that extend over millimeter length scales. The mesopores within these monodomains were closely aligned with the flow direction and were well ordered. In contrast, materials prepared close to the time of sol gelation were often misaligned and always more disordered.

4. 2 Experimental Section

4. 2. 1 Sample Preparation

Silica sols were prepared from tetramethoxysilane (99%, TMOS, Aldrich), acidified water (HPLC grade, pH ~ 2) and cetyltrimethylammonium bromide (CTAB, Aldrich). The first step in the procedure was to mix 0.250 g of TMOS with 1 mL of acidified water, with stirring. The methanol generated by the hydrolysis of TMOS was then removed under vacuum.[34] CTAB (0.6 g) was subsequently dissolved in the sol by vigorous stirring, and by repeated inversion while centrifuging. For SMT experiments, all samples were doped to nanomolar concentrations with N,N′-bis(octyloxypropyl)-perylene-3,4,9,10-tetracarboxylic diimide (OPDI)[50] (see **Figure 3.3**) by addition of 10 μL of 200 nM ethanolic dye solution to the sol, yielding a final dye concentration

of ~2 nM. Sols prepared in this manner fall within the hexagonal region of the ternary CTAB/water/ethanol phase diagram.[127] The sols were subsequently aged at 35 °C in the dark, for a period of 0 to 20 hours. Finally, they were injected into microfluidic channels and capillaries for characterization by SMT and SAXS, respectively. The gelation time for the sol was determined by checking sol fluidity at 2 h intervals. Sol fluidity was assessed by inverting the vial and observing whether the sol flowed over the course of 10 min. The sols were concluded to gel 19 ± 1 h after preparation.

4. 2. 2 Microfluidic Channel Design and Fabrication

Microfluidic chips were designed to incorporate rectangular channels of 70 μm depth, 15 mm length, and 2 mm width (**Figure 4.1a**). The channels were etched into microscope slides (FisherFinest Premium) using a buffered NH_4F oxide etchant (Transene Co.).[139] Channel dimensions were defined by patterned commercial electrical tape contacted to the slide glass. After etching, the tape was removed and the slides were rinsed using 18 MΩcm water. Channel depths were measured using a surface profiler (Ambios Technology). Once etched to the desired depth, 1 mm diameter inlet and outlet holes were mechanically drilled at the ends of the channel.

Each etched slide was then bonded to a microscope coverslip (FisherFinest Premium) to form a microfluidic cell.[139] Before assembly of the cell, the slide and coverslip were thoroughly cleaned by a multistep process. First, the etched slide and coverslip were submerged in warm soap water, sonicated for 10 minutes and rinsed with 18 MΩcm water. They were subsequently sonicated in a warm 10 wt% NaOH and again rinsed. Next, they were immersed in 5 vol% H_2SO_4. Immediately after a final rinse in 18 MΩcm water, the slide and coverslip were pressed together using binder clips. The assembled chips were then placed in an oven at 45 °C for 30 min to evaporate remaining water and to prebond the two pieces of glass. Finally the cells were transferred

to a furnace and permanently bonded by heating at 350 °C for 12 h.

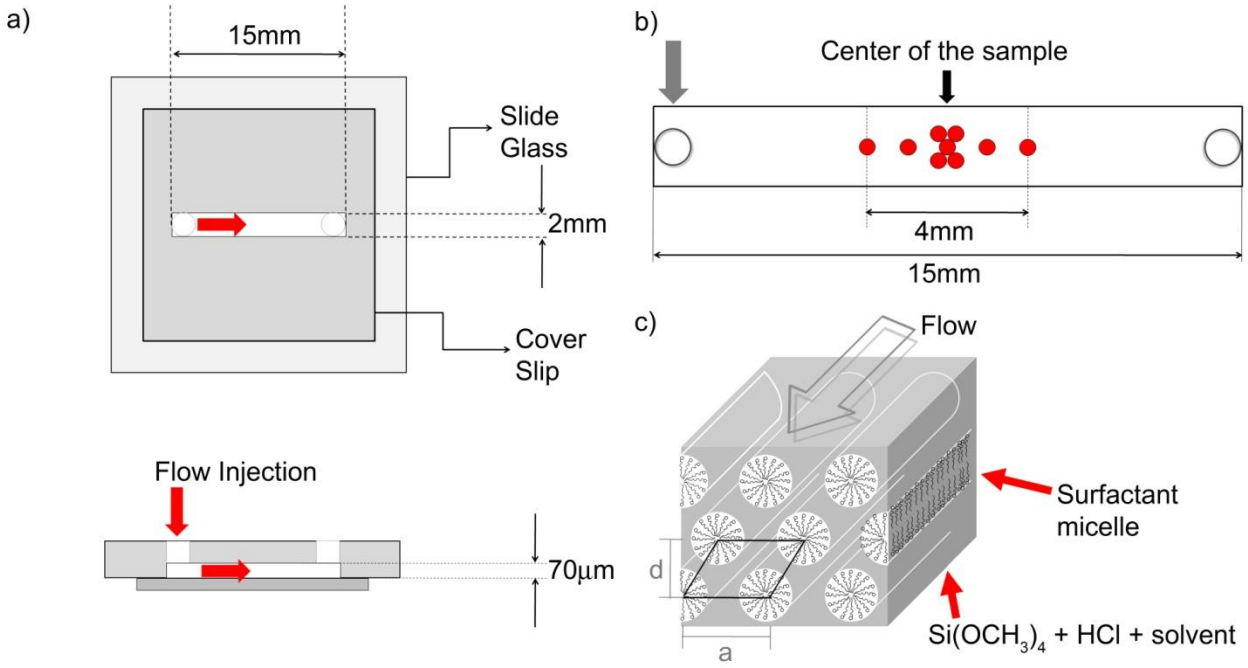

Figure 4.1 a) Etched glass microfluidic cell employed to obtain flow-aligned mesoporous silica monoliths for SMT experiments. These cells are comprised of an etched microscope slide incorporating a rectangular channel 15 mm long, 2 mm wide and 70 µm deep, with inlet and outlet holes drilled through the glass at the channel ends. A microscope cover glass is bonded to each slide to enclose the channel and to allow for imaging with a high NA objective. b) Locations at which SMT tracking measurements were made within each monolith (red circles). c) Model for flow-aligned, hexagonally arranged cylindrical surfactant micelles in mesoporous silica.

4. 2. 3 Flow Alignment of Sols

Silica sols were aged for 0, 4, 8, 12, 16 and 20 h prior to loading into the microfluidic channels and capillaries. Sols aged beyond 20 h could not be infused into the microfluidic channels. For filling of microfluidic channels, the sol was first drawn into a glass capillary, using a syringe pump. The capillary was then inserted into the channel inlet and the syringe pump reversed to introduce the sol into the channel. Sol was pumped into the channel at a flow velocity of ~12 mm/min. Once the channel was filled, the inlet and outlet holes were sealed using two-part 5 min epoxy. The microfluidic chips were then stored for one additional day, at 35 °C in the dark, to

ensure that the sol had gelled in each case.

4. 2. 4 Single Molecule Tracking

All SMT experiments were conducted on a wide-field fluorescence microscope operated in the through-objective total internal reflection fluorescence (TIRF) mode.[138] The optical microscope employed has been described previously.[50, 122] For excitation of the dye, 488 nm light from a blue diode laser was employed. The incident laser power was maintained at 4 mW in all experiments. In most, the incident light was linearly polarized parallel to the microfluidic channel axis. An electron multiplying CCD camera (Andor iXon DU-897) was used to detect sample emission (all polarizations).

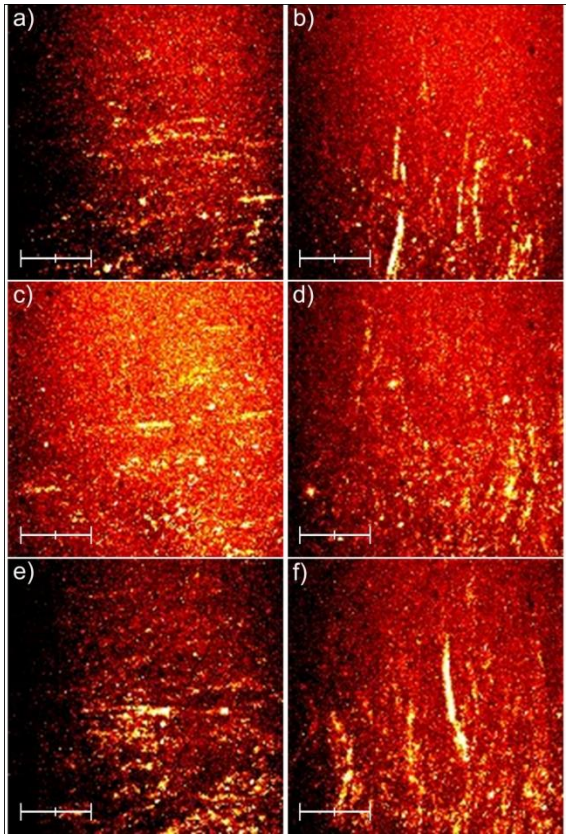

Figure 4.2 Representative wide-field fluorescence images of a flow-aligned monolith from an 8 h aged sol under different excitation polarizations. The excitation polarization is circular (a, b), horizontal on the optical table (c, d) and vertical on the optical table (e, f). The initial direction of the microfluidic channel axis was parallel to the horizontally polarized incident

light (a, c, e) and rotated by 90° (b, d, f). The images were obtained using the Z-project routine in ImageJ and depict the maximum intensity for each pixel in the associated videos. The scale bars are 5 μm.

TIRF videos were collected from nine different locations in each monolith (**Figure 4.1b**). Five of these were collected at evenly spaced 1 mm intervals along the centerline of the monolith. Four additional measurements were made at points displaced vertically and horizontally from the monolith center by a distance of 300 μm. Videos were acquired as 1000 frame sequences with a cycle time of 0.042 s per frame, using an electron multiplying gain of 30 and a 10 MHz readout rate. Camera pixels were binned in a 2 X 2 configuration, giving a calibrated image pixel size of 125 nm. Unbiased excitation and detection of the molecules was verified by exciting the sample with linearly polarized light of orthogonal polarizations (perpendicular and parallel to the channel axis), with circularly polarized light, and with the microfluidic channel oriented in orthogonal directions on the microscope stage (see **Figure 4.2** and **Table 4.1**). The number of molecules detected was independent of sample orientation on the microscope stage and the level of sample order was invariant with incident polarization and sample orientation.

Table 4.1 Single molecule tracking data under different excitation polarization and channel direction. Error bars give the 95% confidence intervals of the mean values

Excitation Polarization	Channel Direction	n[e]	$\langle P \rangle$
Circular	0°[c]	192	$0.89_{\pm 0.03}$
	90°[d]	182	$0.85_{\pm 0.04}$
Horizontal[a]	0°	246	$0.85_{\pm 0.04}$
	90°	262	$0.86_{\pm 0.04}$
Vertical[b]	0°	317	$0.88_{\pm 0.03}$
	90°	315	$0.87_{\pm 0.03}$

[a] Parallel to the optic table

[b] Vertical to the optic table

[c] Parallel to the horizontal polarization

[d] Rotated by 90° from initial direction (0°)

[e] Number of trajectories analyzed from 6 images in each sample.

4. 2. 5 2D SAXS Measurements

Two-dimensional (2D)-SAXS measurements were performed at the Characterization Facility at the University of Minnesota, Minneapolis, MN. The SAXS instrument employed incorporates a Rigaku 12kW Cu rotating anode source ($\lambda = 1.54$ Å) and a multi-wire area detector. The sample-to-detector distance was 59.5 cm. As in the single-molecule tracking experiments, 0, 4, 8, 12, 16 and 20 h aged sols were prepared and characterized. In this case, the sols were drawn into 1 mm diameter thin-walled (10 μm wall thickness) capillaries (Charles Supper Co.). The capillaries were then flame sealed. Several replicate SAXS patterns were acquired for each sample, with an exposure time of 300 s.

4. 3 Results

4. 3. 1 2D SAXS Measurements

The SAXS pattern obtained from a representative flow-aligned mesoporous silica monolith is shown in **Figure 4.3a** (inset). The capillary from which these data were acquired was oriented along the vertical direction on the figure. The bright regions on either side of the X-ray beam (center) demonstrate that the scattering is strongest in the plane perpendicular to the capillary axis. Scattering intensity as a function of 2θ is also plotted in **Figure 4.3a**. These data are consistent with the presence of hexagonally ordered cylindrical mesopores.[140] The characteristic (100) peak appears at $2\theta \approx 1.67°$, which corresponds to a *d*-spacing of ~52.8 ± 0.3Å (from multiple measurements). The *d*-spacing in this case is significantly larger than previously reported for dry[50, 140] and/or calcined mesoporous silica.[4, 140] This discrepancy is attributable to swelling of the surfactant micelles in the wet gels being investigated. Importantly, the *d*-spacing was found to be independent of sol aging time, as shown in **Figure 4.3b**.

Information on mesopore alignment and order was obtained by plotting the SAXS data as a function of azimuthal angle, χ, as shown in **Figure 4.3c**. The observation of strong scattering in the plane perpendicular to the capillary axis demonstrates that the mesopores are aligned parallel to the flow direction, on average, as depicted in **Figure 4.1c**. Qualitatively, the sharpness of the scattering peak in χ indicates that the mesopores are relatively well ordered, for short sol aging times (see **Figure 4.3c**, 4 h data). SAXS anisotropy data obtained for longer aging times show a trend in mesopore order that is consistent with the results of SMT experiments (see below). In particular, the incorporation of misaligned mesophases and a dramatic decrease in materials order is observed for capillaries filled near the time of sol gelation (see **Figure 4.3c**, 20 h data).

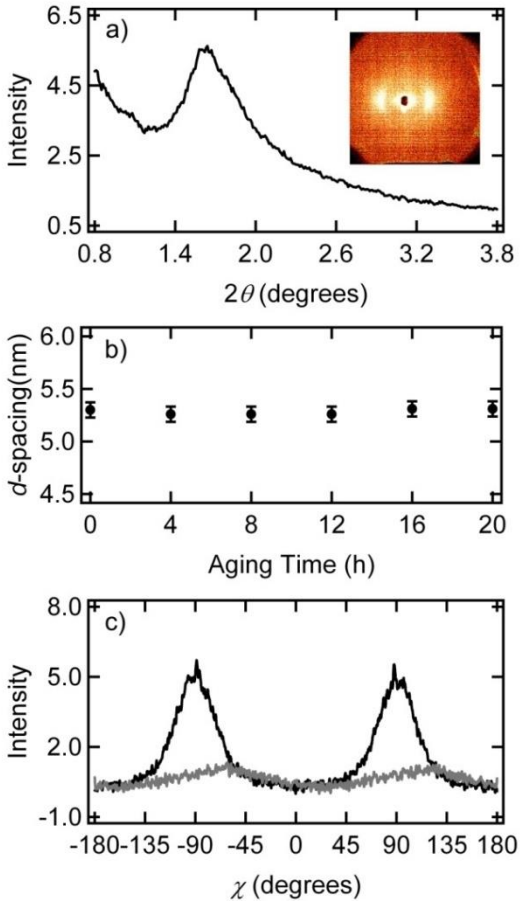

Figure 4.3 a) X-ray scattering intensity as a function of scattering angle 2θ, derived from the 2D SAXS pattern shown in the inset. The data was obtained from a flow-aligned mesoporous

silica monolith prepared within a cylindrical glass capillary from a 4 h aged sol. The capillary was oriented along the vertical direction on the scattering pattern (see inset). b) Characteristic *d*-spacing for hexagonally arranged cylindrical mesopores in the silica monoliths as a function of sol aging time. The data demonstrate that mesopore spacing is independent of sol aging time. Error bars depict the 95% confidence intervals about the mean. c) Scattering intensity as a function of azimuthal angle, χ, from 4h (black) and 20 h (gray) aged sols. Here, 0° corresponds to the long axis of the capillary.

4. 3. 2 Single Molecule Tracking Studies

The diffusion of single molecules in the mesoporous silica monoliths was investigated by recording wide-field TIRF-mode videos.[138] Use of TIRF imaging selectively probes molecules near the gel/glass interface and facilitates SMT by limiting the background fluorescence from dye molecules at different depths in the monolith. The depth probed is limited to ~200 nm (i.e., the $1/e^2$ distance) by the decay of the evanescent fields from the gel/glass interface.

A representative wide-field image of a flow-aligned silica monolith (prepared from a 4 h aged sol) is shown in **Figure 4.4a**. This image was generated by combining all 1000 frames from a single video, using the z-project routine in the ImageJ software package; it depicts the maximum intensity observed at each pixel in the video. Clearly apparent in the image are a large number of horizontal streaks. These streaks demonstrate the predominance of 1D diffusion by the individual OPDI molecules. The observation of 1D molecular motion is consistent with the presence of open (albeit surfactant-filled) cylindrical mesopores in the silica monoliths. The SMT data also demonstrate that the mesopores are aligned predominantly along the flow direction (**Figure 4.1c**). Along with 1D diffusing molecules, immobile molecules are also found in the videos (e.g., round spots shown in **Figure 4.4a**). Mobile and immobile molecules were distinguished by comparison of the single molecule localization precision[50] (calculated using Eq. 7 in Ref 47; 63 nm, on average) with the frame-to-frame mean square displacement (MSD) for each molecule. Those spots exhibiting MSD values greater than the localization precision at better than 90% confidence were

concluded to be mobile. The observation of immobile molecules was ascribed to adsorption of some at the gel/glass interface, while others may be trapped within the silica matrix or in short (i.e. closed) silica mesopores. Such fixed molecules provide no information on materials order and are excluded from further analysis, as discussed below.

For detailed analysis of single molecule motions, automated software routines available as an ImageJ plugin[141] (modified in house) were employed. Trajectories depicting the motions of the individual molecules within each video were obtained. Only those trajectories >6 frames in length were selected for further analysis. Relatively short trajectories were obtained in the present case because single molecule diffusion was relatively fast (see below), making it difficult to link the fluorescent spots observed in the video frames into longer trajectories. Trajectory length may also be limited by blinking of the molecules (i.e., fluorescence intermittency). Trajectories were terminated when the molecule being tracked disappeared for one or more frames. **Figure 4.4b** depicts the trajectories produced by the video shown in **Figure 4.4a**, again reflecting the predominance of 1D molecular motion.

The single molecule trajectories incorporate quantitative data on molecular position as a function of time. As we have demonstrated in previous SMT studies,[6] these data can be fit to a line, using orthogonal regression methods,[133] to quantitatively determine the in-plane orientation of each 1D trajectory. This analysis also provides additional statistical data such as the error in the trajectory orientation.[50] The trajectory angles were used to construct histograms showing the distribution of trajectory orientations. Importantly, as the trajectories depict molecular motions within discrete silica mesopores, they also provide a measure of pore alignment. **Figure 4.4c** presents the distribution of trajectory angles for the data shown in **Figure 4.4b**.

The histogram is sharply peaked near 0^{o}, corresponding to the approximate direction ($\pm 5^{o}$)

of sol flow during filling of the microfluidic channel. While the position of the peak indicates average pore alignment is along the expected direction, the narrow distribution observed also suggests a high degree of orientational order.

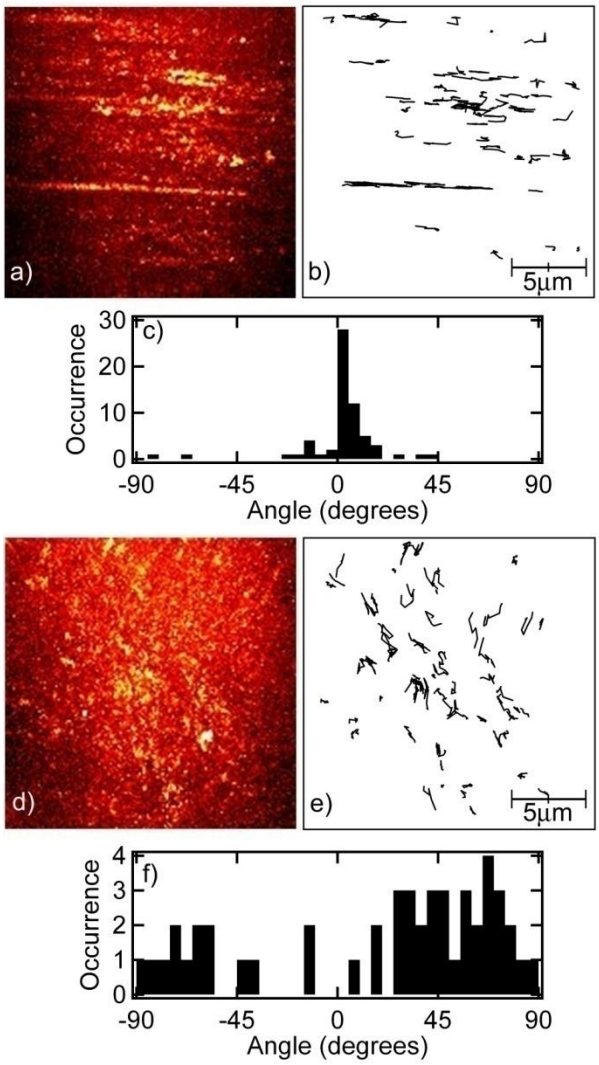

Figure 4.4 a) Representative wide-field fluorescence image of a flow-aligned monolith prepared from a 4 h aged sol. This image was obtained using the Z-project routine in ImageJ and plots the maximum intensity for each pixel observed in the associated video. b) Single molecule trajectories obtained from the same video. c) Histogram showing the trajectory angles relative to the flow axis (0º) in the microfluidic channel. d)-f) Similar data obtained from a flow-alinged monolith prepared from a 20 h aged sol.

As the main purpose of this report is to explore the dependence of pore organization on sol

aging time, similar SMT data were collected from a series of samples prepared from sols aged for up to 20 h. A clear trend towards misaligned and disordered mesopores was observed near the time of gelation (~ 19 h, see below). Monoliths prepared from 20 h aged sols were found to be the most disordered. **Figure 4.4d** depicts a representative image obtained from one such sample. The trajectory data and the trajectory angle histogram obtained from this video are shown in **Figure 4.4e,f**. As shown by these data, monoliths prepared from 20 h aged sols exhibited fewer 1D trajectories. Furthermore, the trajectories recorded from these samples were more randomly aligned and in some cases were even aligned perpendicular to the sol flow direction. It must be noted that some trajectories in these samples appear to depict 2D molecular motion. While the "orientations" of such trajectories are strictly undefined, their fitted values were still included in the pore orientation histograms and subsequent analysis to most properly reflect the true level of mesopore order in these materials.[122]

Wide-field videos and trajectory data were acquired for three replicate sample series prepared from sols aged for 0, 4, 8, 12, 16 and 20h (i.e., a total of 18 samples). Data were collected for nine different locations in each sample, as defined in **Figure 4.1b**. Representative histograms depicting the trajectory orientations for one sample series are shown in **Figure 4.5**. These histograms are compilations of trajectory angle data from all nine locations in each sample. Qualitatively, the distributions show that for short aging times, the mesopores are well aligned (on average) along the expected direction. These data appear to depict a small systematic bias to positive angles. As noted above, samples can only be aligned on the microscope to $\pm 5^{o}$. Single data series as show in **Figure 4.5** may also exhibit some bias within this range. However, data compiled from measurements on several different samples over several days show no such bias (see **Table 4.2**).

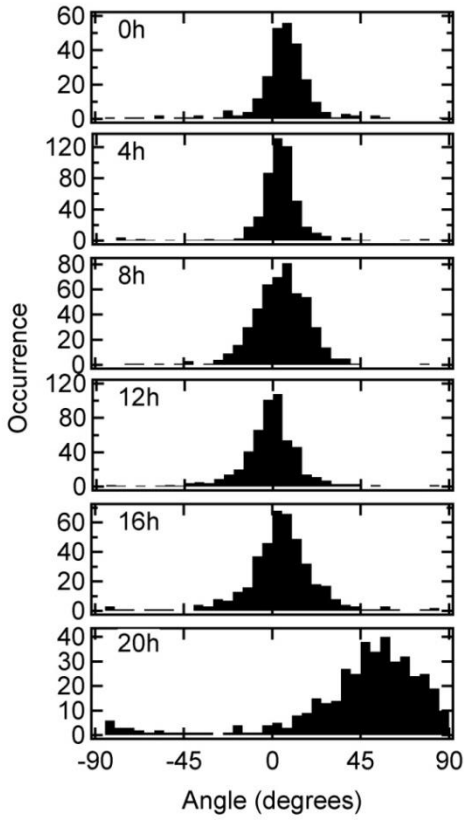

Figure 4.5 Histograms depicting the trajectory angles compiled from all 9 images collected from each sample in a single, representative set of flow-aligned silica samples, as a function of sol aging time. The data demonstrate that the mesopores are all well aligned along the flow direction (0º) over distances of several millimeters, for materials prepared prior to gelation of the sol at ~ 19 h. Near the gelation time, markedly more disordered and misaligned materials are obtained (see 20 h data).

The distribution widths reflect a relatively high level of mesopore orientational order that does not vary dramatically with sol aging, up to about the time of gelation. The mesopores become misaligned and markedly more disordered in monoliths prepared from sols aged to close to the gelation time, as demonstrated by the 20 h aged sample (**Figure 4.5**). As noted above, gelation of these sols occurred at ~19 h. The bias to positive angles in this case falls far outside that expected from alignment error on the microscope. Evidence of misaligned mesopores was also observed by SAXS (**Figure 4.3c**, 20 h data) in similarly prepared samples.

In our earlier studies of spin-coated mesoporous silica films, it was found from excitation-polarization-dependent imaging that OPDI molecules diffused within the silica pores in a strongly aligned state,[50] with their long axes oriented parallel to the pore axis. Such strong orientation of the dye clearly results from its steric confinement within the silica mesopores. In the present samples, the images obtained were largely independent of excitation polarization (see **Figure 4.2** and **Table 4.1**), demonstrating that the alignment measurements are not biased by polarization-selective detection of oriented molecules within pores aligned along the expected direction. These results are also consistent with "rapid" tumbling of the dye within the pores on time scales shorter than the video frame time. The pores in the present samples are concluded to be larger than in the spin-coated films, as is also suggested by the larger *d*-spacing determined from the SAXS data.

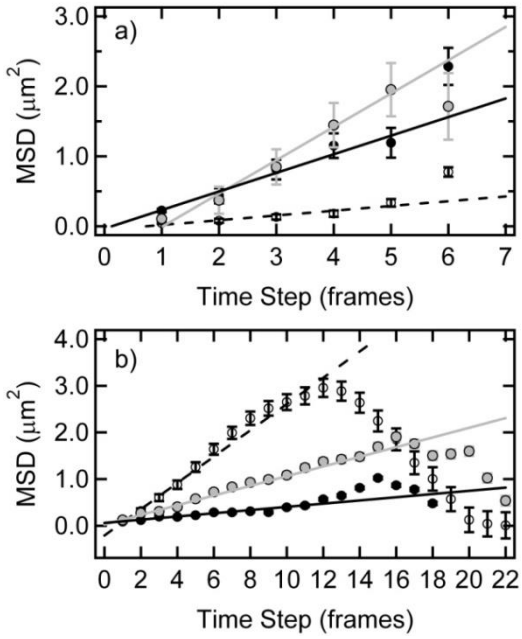

Figure 4.6 Selected MSD data (symbols) from (a) the shortest (7 frames) and (b) the longest (23 frames for dashed and gray lines, and 18 frames for black line) trajectories in a single video of a flow-aligned monolith from an 8 h aged sol. All frame times were 0.042 s, as described in the experimental section. Dashed and solid lines were obtained by fitting the first five points of each trajectory and diffusion coefficients were determined from the slope of these lines. Error bars depict the standard deviation about the mean in each.

Finally, the SMT data also provide the means to assess OPDI mobility within the silica

mesopores, as a function of sol aging time. The apparent diffusion coefficients, *D*, for individual mobile molecules were determined from their MSD values over short time scales, using $MSD = 2Dt$ (see **Figure 4.6** for representative examples).[142] As shown previously, these measurements are somewhat biased to smaller values for short trajectories.[122] **Figure 4.7a** depicts a histogram of the *D* values obtained from a 4 h aged sample, from which a mean *D* value of 1.74 $\mu m^2/s$ is obtained. *D* values measured as a function of sol aging time are presented in **Figure 4.7b** and show no apparent trend with sol aging time. The *D* values from SMT studies are ~ 100 fold larger than those reported for spin-coated mesoporous silica films under drier conditions.[50, 137, 143]

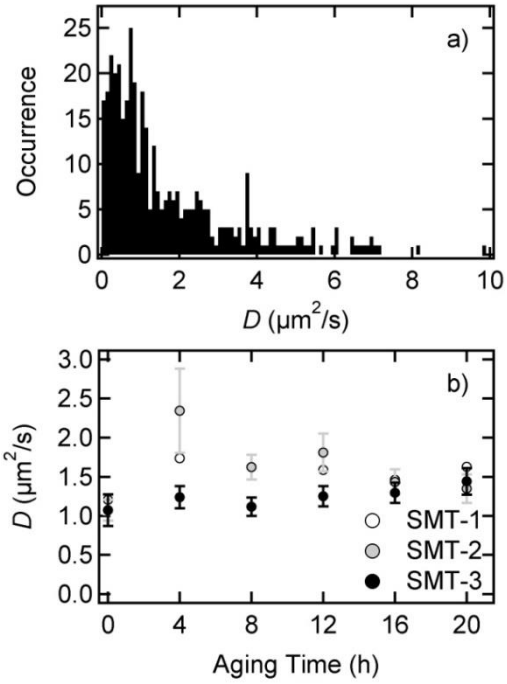

Figure 4.7 a) Representative histogram showing diffusion coefficients determined from a single flow-aligned mesoporous silica sample prepared from a 4 h aged sol. The diffusion coefficients were determined from the mean square diffusion coefficients obtained as a function of sol aging time for three replicate sample series. No apparent trend is observed in these data, suggesting the viscosity within the surfactant-containing mesopores is invariant over the range of samples investigated. Error bars depict the 95% confidence intervals about the mean in each case. displacement exhibited by each single molecule at short time delays (i.e. 5 frames).). b) Mean diffusion coefficients obtained as a function of sol aging time for three replicate sample series. No apparent trend is observed in these data, suggesting the

viscosity within the surfactant-containing mesopores is invariant over the range of samples investigated. Error bars depict the 95% confidence intervals about the mean in each case.

4. 4 Discussion

4. 4. 1 Quantitative Assessment of Mesopore Alignment and Order

The representative SMT results depicted in **Figure 4.5** demonstrate that with the exception of sols aged to near the gelation time (~ 19 h), the majority of materials are comprised of well-ordered monodomains in which the average mesopore alignment is along the flow direction. These monodomains extend over distances of several millimeters. The high degree of pore alignment and order in the present materials stands in stark contrast to prior results from spin-coated mesoporous silica films, in which organized domains only a few tens to hundreds of microns in size were observed.[50, 144] These previous materials exhibited widely-variable domain alignments, even when spin-coating methods meant to induce mesopore alignment along a particular direction were employed.[50] Their "polycrystalline" nature clearly reflects the participation of nucleation and growth processes in domain formation.[144] Organized domains in the present samples were produced instead by flow alignment of hexagonally-organized cylindrical mesophases already present in the sol.[69] Materials organization was quantitatively assessed based on two distinct parameters: i) average mesopore alignment relative to the expected direction and ii) the materials order parameter, reflecting the distribution of mesopore orientations around the average alignment direction.

Quantitative assessment of *average* mesopore alignment was accomplished by calculating the average in-plane trajectory angle, $\bar{\beta}$, for all individual trajectories acquired from three replicate samples at each aging time. **Table 4.2** presents these results. For samples prepared from sols aged for $\leq$ 16 h, $\bar{\beta}$ was found to be 0^o (the expected alignment), within the error of sample alignment on the microscope (i.e., $\pm 5^o$). In contrast, significant deviations from the flow direction were found

for 20 h aged sols, and $\bar{\beta}$ also varied widely between replicate samples. For the three replicate samples compiled in Table 1, the individual $\bar{\beta}$ values obtained were 51° (data in **Figure 4.5**), 10° and -2°. Comparison of the results obtained for samples aged ≤ 16 h with those aged for 20 h demonstrates that effective flow alignment requires the injection of a fluid sol into the microfluidic channel. Although somewhat more variable, the SAXS results provide support for this conclusion. As shown in **Table 4.2**, the greatest deviations from 0° are again observed for the 20 h aged sol, as demonstrated by the large error bar (95% confidence interval) on $\bar{\beta}$. Greater variability in the SAXS results may reflect differences in pore populations probed: SAXS measurements probe pore organization throughout the monolith, while TIRF-mode SMT probes only those pores within ~200 nm of the gel-glass interface.

Quantitative data on mesopore order was obtained from the widths of the SMT trajectory angle distributions (**Figure 4.5**). The widths of the scattering peaks in SAXS anisotropy data (**Figure 4.3c**) provide similar information. In both cases, the data obtained actually represent a 2D projection, $f(\beta)$, of the 3D pore orientation distribution function.[145, 146] For materials of cylindrical symmetry, 3D order is most often reported as the average value of the second Legendre polynomial. However, as in previous reports,[50, 122] a 2D order parameter, $\langle P \rangle$, is employed here instead. It is defined as follows:

$$\langle P(\Delta\beta) \rangle = 2\langle \cos^2(\Delta\beta) \rangle - 1 \qquad \text{(Eq. 4.1)}$$

where $\langle \cos^2(\Delta\beta) \rangle$ is given by:

$$\langle \cos^2(\Delta\beta) \rangle = \frac{\int_0^{\pi} f(\Delta\beta) \cos^2(\Delta\beta) d(\Delta\beta)}{\int_0^{\pi} f(\Delta\beta) d(\Delta\beta)} \qquad \text{(Eq. 4.2)}$$

Here, $\Delta\beta = \beta - \bar{\beta}$, where β represents the individual trajectory angles, and $\Delta\beta$ defines their deviations from the average trajectory angle for each aging time. In practice, $\langle \cos^2(\Delta\beta) \rangle$ is

determined from the arithmetic mean of the $\cos^2(\Delta\beta)$ values from the single molecule trajectories. For a perfectly aligned mesophase $\langle P \rangle$ = 1.0, while for a totally disordered population $\langle P \rangle$ = 0.0.

Several factors motivate the use of this alternative (2D) order parameter. For the SMT data, out-of-plane disorder is assumed to be much smaller than in-plane disorder. The shear rate during channel filling is inversely proportional to the channel dimension, suggesting a narrower orientation distribution in the out-of-plane direction. The observation of aligned pores extending for tens of microns in the SMT data provides support for this assumption. Were the pores tilted out of the image plane by only a few degrees, they would appear much shorter than is observed (see **Figure 4.4**) as they would extend beyond the excitation volume of the microscope. While the orientation distribution function is expected to be cylindrically symmetric for the SAXS samples, comparison with SMT data requires the use of the same order parameter.

The $\langle P \rangle$ values obtained from SMT data demonstrate that highly ordered mesoporous materials can be obtained from sols aged for ≤ 16 h. As shown in Table 1, results derived from several thousand trajectories produce relatively constant $\langle P \rangle$ values ranging from 0.88 to 0.79. These values are similar to those reported previously for individual domains in spin-coated mesoporous silica films.[50] A marked decrease in $\langle P \rangle$ is observed for samples prepared from 20 h aged sols, for which $\langle P \rangle$ = 0.37. This same trend in order with sol aging time was observed in three replicate sample series. The order parameters obtained from these individual series are plotted in **Figure 4.8**. The average width of the individual distributions provides a more fundamental view of materials order. These values are given in **Table 4.2** as $\langle \Delta\bar{\beta} \rangle$. Average distribution widths of 14° to 19° are obtained for samples prepared well before sol gelation. An increase in the average distribution width to 34° occurs near the time of gelation.

SAXS anisotropy data depict a similar level of mesopore orientational order and a

similar trend with sol aging time. In this case, due to difficulties with background subtraction, the results were fit to Gaussian functions and their widths, σ, were used to determine the associated $\langle P \rangle$ values:

$$\langle P \rangle \approx 2\cos^2\sigma - 1 \qquad \text{(Eq. 4.3)}$$

The values obtained are given in **Table 4.2** and are also plotted along with the SMT results in **Figure 4.8**. The $\langle P \rangle$ values obtained by SAXS provide strong supporting evidence for the high level of materials order deduced from SMT data. However, the SAXS $\langle P \rangle$ values are almost all modestly smaller than those from the SMT data. These differences are easily attributable to differences in both fundamental and experimental aspects of the measurements. SAXS probes periodic structures in the monoliths while SMT probes the alignment of individual mesopores that support 1D diffusion. Furthermore, SAXS probes the entire monolith thickness, while TIRF-mode SMT probes materials organization only near the gel/glass interface.

Table 4.2 Single molecule tracking and SAXS data compiled from a series of replicate samples in each case. Errors give the 95% confidence intervals of the mean values.

Aging Time (h)	Single Molecule				2D-SAXS				
	n_1[a]	$\overline{\beta}$[b]	$\langle P \rangle$	$\langle \Delta\beta \rangle$[c]	n_2[d]	$\overline{\beta}$[e]	$\langle P \rangle$	$\langle \Delta\beta \rangle$[f]	*d*-spacing (nm)
0	883	$3_{\pm 1}$	$0.88_{\pm 0.02}$	14	6	$-16_{\pm 16}$	$0.66_{\pm 0.13}$	24	$5.30_{\pm 0.04}$
4	997	$2_{\pm 1}$	$0.86_{\pm 0.02}$	15	3	$0_{\pm 1}$	$0.81_{\pm 0.02}$	18	$5.26_{\pm 0.03}$
8	1053	$-3_{\pm 1}$	$0.80_{\pm 0.03}$	18	6	$-15_{\pm 20}$	$0.75_{\pm 0.07}$	21	$5.26_{\pm 0.06}$
12	1173	$-2_{\pm 1}$	$0.86_{\pm 0.02}$	15	3	$10_{\pm 4}$	$0.75_{\pm 0.20}$	20	$5.26_{\pm 0.02}$
16	1038	$3_{\pm 1}$	$0.79_{\pm 0.02}$	19	3	$-5_{\pm 6}$	$0.77_{\pm 0.05}$	20	$5.31_{\pm 0.02}$
20	886	$25_{\pm 3}$	$0.37_{\pm 0.04}$	34	3	$-8_{\pm 100}$	$0.39_{\pm 0.38}$	31	$5.31_{\pm 0.01}$

[a] Number of trajectories analyzed from three different samples at each aging time.

[b] Average trajectory orientation in degrees, relative to the expected alignment direction, given as the arithmetic mean of all individual trajectory orientations.

[c] Average width of the trajectory angle distribution in degrees, derived from single molecule data.

[d] Number of 2D-SAXS measurements analyzed (3 measurements were made per sample).

[e] Average alignment of hexagonal mesopores in degrees, relative to the expected alignment direction, determined from 3-6 replicate SAXS measurements.

[f] Average width of hexagonal mesopore orientation distribution determined from SAXS, i.e., $\langle \Delta\beta \rangle$ = σ in Eq. 4.3.

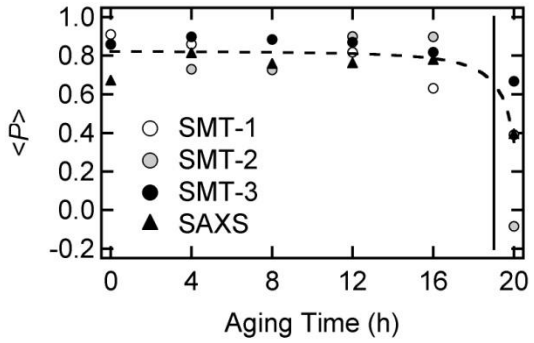

Figure 4.8 Order parameters measured for flow-aligned silica monoliths as a function of sol aging time prior to injection into the microfluidic channel. Shown are SMT data from three replicate sample series along with SAXS data. The data depict a constant, high level of organization up to approximately the gelation time (~ 19 h, vertical line), beyond which an abrupt decrease in order is observed. The dashed line has been appended to better highlight this tren

4. 4. 2 Mechanism for Organization of Flow-Aligned Mesopores

The SMT and SAXS results demonstrate that mesopore alignment and order is strongly dependent upon sol aging time. Microfluidic channels filled well before gelation yield materials comprising large, well-ordered monodomains of mesopores aligned along the flow direction. In contrast, those filled close to the time of sol gelation yield monoliths in which the mesopores are misaligned and substantially more disordered. A simple model has been developed to explain these observations, as shown in **Figure 4.9**.

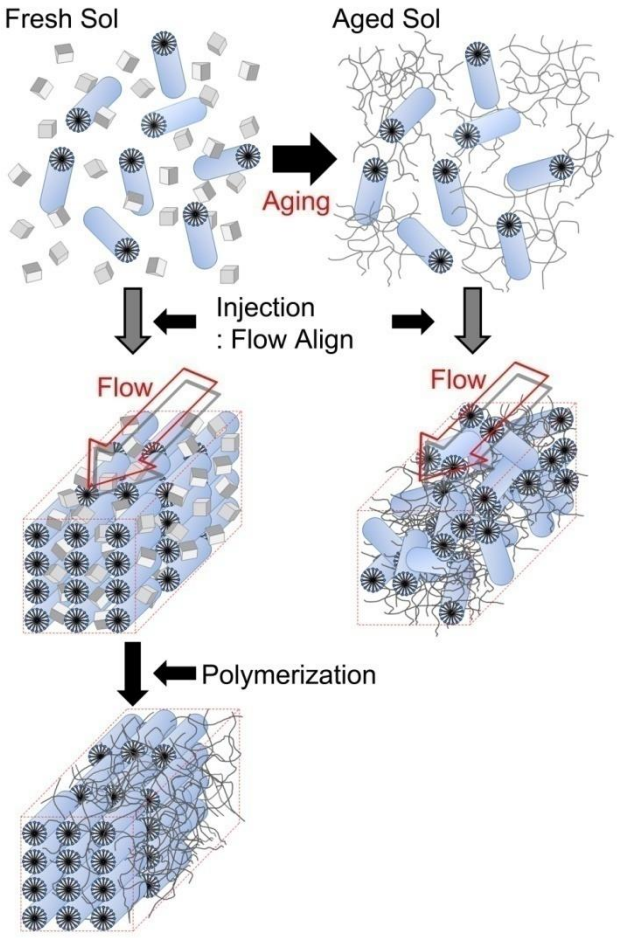

Figure 4.9 Model for the trend in mesopore order as a function of sol aging time. Surfactant-templated sols that are injected into microfluidic channels or capillaries prior to gelation are strongly aligned by shear flow during injection. Subsequent gelation of the sol forms a rigid matrix incorporating well aligned mesopores. For sols close to the gelation time, the rigid gel structure has already begun to form around randomly aligned domains in the original vessel. These sols are not strongly aligned by flow during injection into the channels and capillaries and may be broken up by strong mechanical forces during injection.

Under the conditions employed, as-prepared (fresh) sols incorporate cylindrical surfactant micelles that are organized in randomly-aligned domains. Prior to gelation, the surfactant mesophase is easily aligned by shear forces during the filling of the microfluidic channels. The mesophase remains aligned during condensation of the silica precursors, which ultimately form a rigid gel around the micelles. Importantly, the sols remain sufficiently fluid up until just before gelation to allow for well-aligned materials to be prepared. However, for sols aged to near or

beyond the gelation time, the transition to a gel state occurs in the original vessel and locks in the original mesophase orientations within the sol. Injection of these rigid, polycrystalline materials into the microfluidic channel produces a monolith comprised of misaligned, disordered mesopores. Mesopore order may reflect whatever alignment/order was originally present, or the mesophase may be broken up as it is infused into the microfluidic channel. It is believed the former mechanism is most important, as evidenced by the 20 h data shown in **Figure 4.5** and the associated replicate measurements. In these cases, the average mesopore alignment ($\bar{\beta}$) values fluctuate from sample to sample and can be far from the expected 0°. The 20 h SAXS data shown in **Figure 4.3c** depicts a similar deviation from the expected $\bar{\beta} = 0^{o}$ for a similarly prepared sample. Taken together, these results suggest that "large" preformed domains present in the original vessel are loaded into the channel. These domains are not strongly aligned by the flow process when infused into the channel near the time of gelation. Were such domains broken up by infusion into the channel, small, randomly-aligned domains, similar to those observed for spin coated films,[50, 121] and exhibiting $\bar{\beta} = 0^{o}$ would be expected.

4. 5 Conclusion

We have demonstrated that well-ordered mesoporous silica monoliths can be obtained by flow alignment of viscous, surfactant-templated sols within etched glass microfluidic channels. The orientational alignment of open, surfactant-filled mesopores in these materials was assessed by tracking the motions of single molecules exhibiting 1D diffusion. Confirmation of materials alignment and order was obtained by SAXS anisotropy measurements. Mesopore organization was explored as a function of sol aging time. Microfluidic channels filled well before gelation of the sol were shown to incorporate large mesoporous monodomains having average pore alignments within a few degrees of the expected direction over distances of several millimeters.

These domains exhibit a high degree of mesopore orientation order, producing 2D order parameters averaging between 0.79 and 0.88. Channels filled near the time of sol gelation exhibited substantially greater variability in average pore alignment and markedly reduced pore order, yielding order parameters near 0.35. The results of this study demonstrate that highly-aligned, well-ordered mesoporous silica monoliths having applications in capillary- and/or microfluidic-based chemical separations can be obtained by simple flow alignment procedures. They also provide important guidance on the sample preparation conditions required to achieve optimum mesopore alignment: fresh sols or those aged for only brief periods of time should be employed.

Chapter 5 - On the Dimensionality of Diffusion in Flow-Aligned Surfactant-Templated Mesoporous Silica: A Single Molecule Tracking Study of Pore Wall Permeability[2]

5. 1 Introduction

Surfactant-templated mesoporous silica films and monoliths[4] find a wealth of potential applications in chemical sensing,[147] catalysis,[9, 148-150] separations,[151, 152] batteries[153] and fuel cells.[154] Broad interest in these materials stems from their unique attributes such as regular and adjustable pore sizes (from 2 to 20 nm), high surface areas, and tunable pore surface chemistries. In many of the aforementioned applications, the ability to prepare aligned, well-ordered one-dimensional (1D) mesopores that guide and confine the motions of reagents or analytes is often required to achieve optimum material performance. A variety of methods for obtaining aligned cylindrical mesopores have been reported to date. Many involve flow alignment of the cylindrical surfactant micelles that serve as structure-directing agents in the precursor sols.[34, 36, 99, 119]

The structure, alignment and organization of mesoporous silica materials are often characterized by small angle X-ray scattering (SAXS)[34, 36, 99, 119] and scanning or transmission electron microscopy (SEM or TEM).[28, 99, 119, 137] SAXS anisotropy measurements provide quantitative data on average pore alignment and order from the angular positions and widths of the diffraction peaks.[36, 146] Pore alignment can be assessed on a microscopic scale by TEM, which also provides evidence of relatively large pore interconnections, blockages and other materials defects.[137] However, none of these methods provides concrete information on the permeability of

[2] Reproduced with permission from (Park, S. C.; Ito, T.; Higgins, D. A. Dimensionality of Diffusion in Flow-Aligned Surfactant-Templated Mesoporous Silica: A Single Molecule Tracking Study of Pore Wall Permeability. J. Phys. Chem. C, 2015, 119, 26101–26110.). Copyright (2015) American Chemical Society.

the pore walls to incorporated reagents or analytes. Evidence that the silica pore walls are relatively permeable has been obtained from water- and organic-sorption[51, 52] and NMR[37] measurements. Possible cross-wall diffusion has also been observed in optical studies of dye molecule release from mesoporous silica materials.[53, 54] The extent to which molecules can pass through the silica pore walls depends upon their size relative to any pore wall openings.[155-157] Besides such steric effects, pore wall permeability in solution-phase applications also depends upon the partitioning of the reagents or analytes (i.e., solutes) to regions nearest the pore walls. The relative polarities of the solute molecules, pore surface and pore-filling medium are all important factors in governing partitioning processes. The charge carried by the molecules and pore surface, and the thickness of the diffuse electrical double layer within the pores are also important factors.[158, 159] Distinguishing the roles played by mesopore structure, order and pore wall permeability in determining the dimensionality of reagent or analyte motions is often difficult when ensemble methods are employed. Perhaps the best methods for such studies involve directly following the motions of the incorporated molecules as they pass through the materials.

Single molecule tracking (SMT) methods are now being widely employed in investigations of mass transport within mesoporous silica[39-43, 121] and related 1D nanostructured systems.[38, 41, 44-46] An important advantage of SMT is that the motions of individual probe molecules can be directly visualized and the dimensionality of their motions quantitatively assessed in local sample regions. In recent work of relevance to this study, the electrophoretic mobility of charged and uncharged dyes within aligned mesoporous silica was explored.[47] The results showed that molecules having different chemical structures and different charges exhibited distinctly different levels of isotropic and anisotropic motion. Most importantly, it was found that charged probe

molecules could be driven across the pore walls by applied electric fields while uncharged molecules primarily moved in 1D along the pore axis.

In the present work, the random diffusive motions of a series of charged and uncharged perylene diimide (PDI) dyes were followed by SMT as a means to explore the origins of pore-wall permeability in mesoporous silica. For this purpose, silica monoliths were prepared by flow injection of surfactant-templated silica sols into microfluidic channels.[34, 36] The triblock copolymer Pluronic F127 was used as the structure-directing agent. Its concentration was adjusted to obtain hexagonally ordered cylindrical micelles in the precursor sols.[48] Silica-free F127 gels were also prepared and characterized to aid in understanding the silica results. The dyes employed include an uncharged PDI, N,N′-bis(octyloxypropyl)-perylene-3,4,9,10-tetracarboxylic diimide, and two doubly charged PDIs, N,N′-bis(3-sulfonatopropyl)perylene-3,4,9,10-tetracarboxylic diimide and N,N′-bis(2-(trimethylammonio)ethyl)-perylene-3,4,9,10-tetracarboxylic diimide.[128] The chemical structures of these dyes are shown in **Figure 3.2**. Each was loaded into separate silica monoliths and their diffusive motions were followed by wide-field fluorescence video microscopy as a function of monolith aging time. Orthogonal regression methods[50] were used to analyze the single molecule trajectory data and to assign the mobility and dimensionality of motion for each molecule. While SMT data have been widely used to measure the rates of diffusion for molecules moving through related gels and polymer matrices,[39, 40, 88, 122] the molecules in the present studies diffused too rapidly to allow for accurate determination of their diffusion coefficients.[122] As a result, fluorescence correlation spectroscopy (FCS) was used to obtain these data from the same samples imaged in SMT studies. The FCS results afforded more information on the environments in which the molecules were incorporated.

5. 2 Experimental Considerations

5. 2. 1 Sample Preparation

Tetramethoxysilane (TMOS) (99%, Aldrich) was used as the silica precursor, while Pluronic F127 (Anatrace) was employed as the structure-directing agent. The chemical structure of F127 is shown in **Figure 3.1**, and has the formula $PEO_{100}PPO_{65}PEO_{100}$. Silica sols were prepared from TMOS, acidified water (HPLC grade, pH ~1.4), n-butanol (reagent grade), and F127. In the preparation process, 0.520 g of TMOS was first mixed with 500 µL of acidified water, with stirring. The methanol generated by TMOS hydrolysis was subsequently removed under vacuum.[34] F127 (0.72 g) and n-butanol (265 µL) were next added to the sol with vigorous stirring, repeated inversion and centrifuging to remove air bubbles. Sols prepared in this manner were optically clear and fall within the hexagonal region of the ternary F127/water/butanol phase diagram.[48] Each sol was doped with either an uncharged, cationic, or anionic PDI dye, all of which were synthesized in house.[128] Each sol was doped by addition of 10 µL of a 200 nM dye solution in ethanol (uncharged PDI) or methanol (charged PDIs) to the sol, prior to mixing as described above, yielding a final dye concentration of ~2 nM.

Dye doped F127 gels comprising ternary F127/water/butanol mixtures were also prepared without inclusion of silica. The same procedure described above was employed to prepare these gels, except that the silica precursor was replaced by an equivalent amount (by weight) of water. The same dyes were added to these samples for SMT studies.

5. 2. 2 Flow Alignment of Gels

Microfluidic channels were used for encapsulation and flow alignment of the mesoporous silica sols.[36, 122] Microfluidic channels were used for encapsulation and flow alignment of the mesoporous silica sols.[36, 122] These channels were designed to be rectangular in shape and of 150

μm depth, 10 mm length, and 2 mm width. A diagram of the channel is shown in **Figure 5.1**. They were prepared by casting uncured poly(dimethylsiloxane) (PDMS, Sylgaard 184) in a prefabricated glass mold. A small rectangular piece of glass coverslip (FisherFinest Premium) was utilized to define the channel dimensions. Once cured, the PDMS monolith was removed from the mold, and 1 mm diameter inlet and outlet holes were punched at each end of the channel. The PDMS monolith and a microscope coverslip (FisherFinest Premium) were subsequently cleaned in an air plasma for 5 min and were then immediately pressed together to form the microfluidic channel. The microscope coverslip formed the bottom surface of the channel. All optical experiments involved imaging through the coverslip.

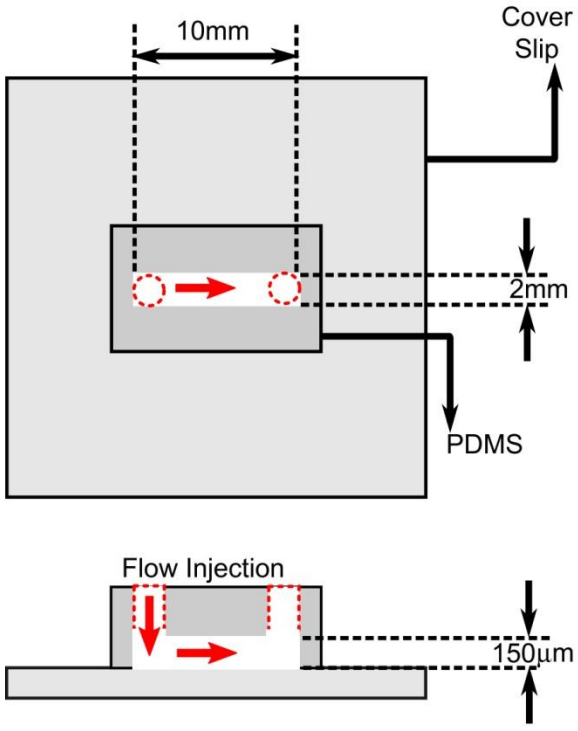

Figure 5.1 PDMS-based microfluidic cell employed to obtain flow aligned mesoporous silica monoliths and F127 gels.

Silica sols and surfactant gels were loaded into the channels by first drawing them into a short glass capillary using a syringe pump. The capillary was then contacted to the channel inlet,

and the syringe pump reversed to fill the channel. The viscous sols and gels were flowed into the channels at a linear flow velocity of ~12 mm/min. After filling, the inlet and outlet holes were sealed by covering with another plasma-cleaned coverslip.

All sols were found to be optically clear immediately after injection into the channel. They were then aged at 35 °C in the dark for periods of 22−77 h before characterization by SMT and FCS. After 77 h, the sols started to become white due to drying and formation of microcracks. SMT and FCS data were only collected out to 77 h aging because light scattering from the samples became significant relative to the fluorescence signal at later times.

The F127 gels prepared in the absence of silica were also injected into microfluidic channels for SMT studies. Imaging of the F127 samples was conducted immediately after sample preparation without aging. These F127 gels have been shown previously by both SMT[122] and small angle X-ray scattering (data not shown) to incorporate flow-aligned, hexagonally organized cylindrical micelles.

5. 2. 3 Single Molecule Tracking

All SMT experiments were conducted on a wide-field microscope that has been described previously.[50] The microscope was operated in the through-objective total internal reflection fluorescence (TIRF) mode and employed closed-loop focus stabilization. A blue diode laser (488 nm) was used as the excitation source. The light delivered to the sample was circularly polarized for all SMT experiments and was passed through a spinning optical diffuser before being reflected from a dichroic beamsplitter (Chroma, 505 DCLP) and focused, off-axis, into the back aperture of an oil immersion objective (Nikon Apo TIRF 100X, 1.49 numerical aperture, NA). The power of the incident light was maintained at 3 mW in all experiments (measured prior to entering the microscope). Fluorescence videos were recorded using an electron-multiplying CCD camera

(Andor iXon DU-897). Videos were collected from nine different locations in each monolith. The data acquisition points were spaced at ~1 mm intervals along the centerline of the monolith. Videos were recorded with a cycle time of 42 ms per frame, using an electron-multiplying gain of 30 and a 10 MHz readout rate. Each video comprised sequences of 500 images. With 2 × 2 binning, the calibrated pixel size in each image was 125 nm.

For analysis of single-molecule motions, the videos obtained were processed using software written in house. First, a rolling-ball background subtraction was performed using a MATLAB routine. The average background signal for each frame was also obtained and saved. The background-subtracted data was next input into a LabView program that was used for locating and fitting the individual fluorescent spots produced by the single molecules in each video frame. These spots were fit to Gaussian functions to determine their precise locations, emission amplitudes and widths. The detected spots were next linked frame-by-frame to produce trajectories depicting the diffusive motions of each molecule.

An orthogonal regression method was utilized for quantitative analysis of the 1D trajectories.[50] Only those trajectories ≥ 10 frames in length were analyzed. By fitting the single-molecule trajectory data to linear functions, this method provides the in-plane trajectory orientation. Other important parameters obtained include two different measures of the spatial variances in molecular position. The positioning variance across the trajectory (σ_δ^2) gives an estimate of the deviation from a 1D model for each trajectory and also provides an estimate of the single-molecule positioning precision (σ_δ). This parameter affords a quantitative means for distinguishing mobile from immobile molecules and different dimensionalities of molecular motion. The motional variance in molecular position (σ_R^2) along each trajectory is also obtained and provides a measure of the geometric length of the trajectory. The ratio of these two parameters,

σ_R/σ_δ, was used to determine the trajectory aspect ratio (i.e. length/width).

The SMT data also provides a measure of the mobility of each molecule from its frame-to-frame mean square displacement (MSD). The average slope of each MSD vs. delay-time plot was used to determine the MSD value. MSD plots (not shown) were only fit out to a six-frame delay because they showed deviations from linearity at longer times. While apparent single-molecule diffusion coefficients could be determined from the MSD values,[142, 160] these were concluded to be inaccurate for the fast moving molecules probed here.[122] Therefore, MSD data were only employed as a means to assign molecules to immobile and mobile populations.

5. 2. 4 Fluorescence Correlation Spectroscopy (FCS)

A home-built confocal microscope was used to collect single point fluorescence time transients for FCS experiments. Fluorescence was again excited by 488 nm light from a blue diode laser. The incident laser power was maintained at ~300 μW. The confocal microscope employed a 1.3 NA oil immersion objective (Nikon Plan Fluor, 100X) to produce a focused spot in the sample, ~ 1 μm above the coverslip-monolith interface. The objective was mounted to a closed-loop piezoelectric positioner (Physik Instrumente) to prevent focus drift. Fluorescence from the sample was collected in reflection, using the same objective. The detection volume was defined by a 50 μm pinhole placed in its primary image plane. The dimensions of the detection volume were determined by calibration with 10 nM aqueous solution of rhodamine 123. Sample emission was detected using a single-photon-counting avalanche photodiode. Time transients were acquired using a 150 μs bin time for 22 h and 41 h aged samples and a 600 μs bin time for 77 h aged samples. They were usually 10^6 data points in length.

5. 3 Results and Discussion

TIRF mode was employed for collection of all wide-field fluorescence videos. Its use was

required to minimize background fluorescence from molecules at different depths in the monoliths. The images obtained are therefore limited to regions within ~200 nm of the gel/glass interface, as governed by the decay of the evanescent fields. **Figure 5.2** depicts representative TIRF-mode images produced by plotting the maximum signal for each pixel across the entire video length (termed Z-projection images). Single molecule trajectories are also shown in **Figure 5.2** and depict the motions of certain dye molecules (i.e., trajectories ≥ 10 frames in length) in these videos. These data are presented as a function of monolith aging time for uncharged, cationic and anionic PDI dyes.

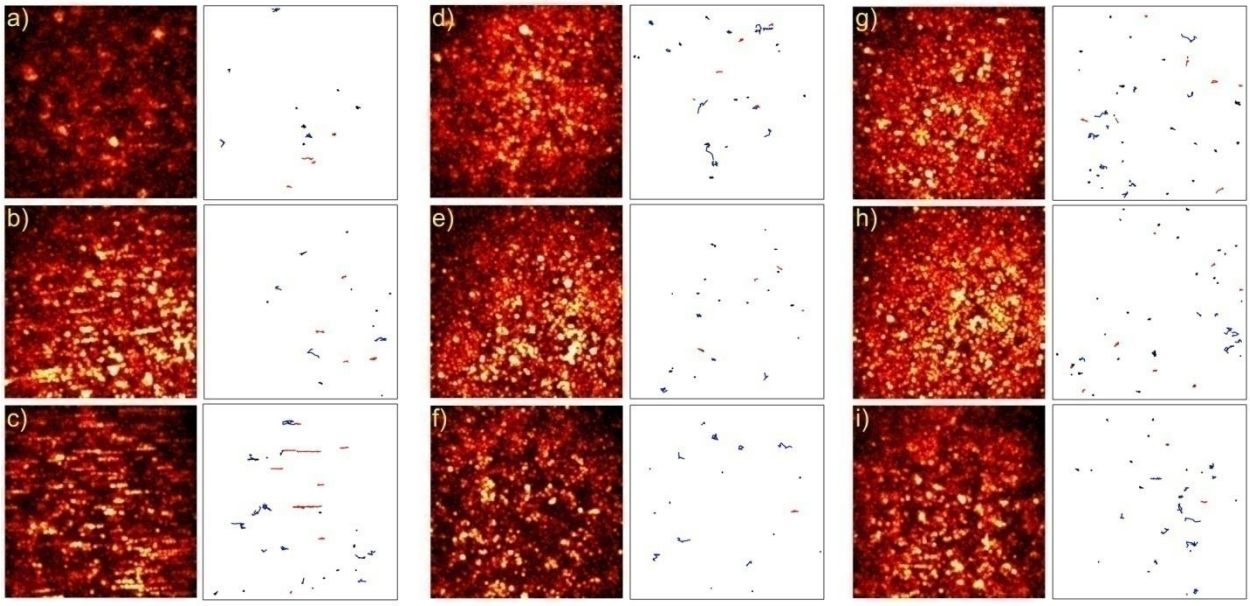

Figure 5.2 Representative TIRF-mode Z-projection images and corresponding trajectory plots obtained from uncharged (a-c), cationic (d-f) and anionic (g-i) PDIs. Results obtained at monolith aging times of 22 h, 41 h and 77 h are shown from top to bottom. Trajectories (≥ 10 frames in length) of immobile molecules and molecules exhibiting 1D and 2D motions are shown in black, red and blue, respectively.

5. 3. 1 General Observations from Video Data

The video data represented in **Figure 5.2** demonstrate that all three dyes exhibit different levels of mobility, with certain single molecules appearing to be immobile on the measurement

time scale while others are mobile. Furthermore, all three dyes exhibit both isotropic and anisotropic diffusive motions. However, the relative populations of molecules exhibiting each of these behaviors clearly depends upon the specific dye employed and on monolith age. **Figures 5.2a-c** show that uncharged PDI molecules exhibit more anisotropic (1D) motions than the others. A gradual evolution in its behavior from apparent isotropic diffusion at the shortest aging time (22 h, panel a) to clear 1D motion at the longest (77 h, panel c) is also revealed in this series of images. In all cases, the 1D motion of the uncharged dye was very closely aligned with the flow injection direction along virtually the entire length of the monolith. In contrast, the charged PDI dyes (**Figure 5.2d-i**) exhibited a predominance of isotropic motion for all samples and all aging times investigated. Although the isotropic motions are visualized in 2D, they most likely reflect 3D diffusion. These same general trends were reproduced in three independent replicate experiments performed on different samples.

Indeed, it has been demonstrated in a number of previous publications that uncharged PDI dyes will diffuse along the 1D pores incorporated within hexagonal surfactant-templated mesoporous silica[36, 39, 40, 42, 43, 121] as well as the hydrophobic cores of cylindrical F127 micelles in their lyotropic liquid crystal mesophases.[122] Thus, the development of 1D motion in the present studies seems to suggest an aging-time-dependent evolution of these 1D nanostructures. While it is possible that organized 1D pores may first appear at the longer aging times, such an explanation is easily discounted. Were these pores to form only well after flow injection of the sols, it is likely they would produce small (i.e., tens of micrometers) randomly oriented domains, as has been observed for solvent-vapor-annealed spin-coated films.[50] The observation of 1D diffusion aligned parallel to the original flow direction is most consistent with the presence of oriented 1D nanostructures that were originally aligned by solution flow.[36]

The predominance of isotropic motion exhibited by the charged dyes demonstrates that they do not follow the same 1D nanostructures as the uncharged dye. Their simple physical confinement within cylindrical silica pores should produce the same level of 1D diffusion and the same time dependent evolution in the dimensionality of their motions. The stark differences in behavior observed for the charged and uncharged PDIs therefore suggests that factors other than physical confinement within the silica pores governs the dimensionality of dye motions.

5. 3. 2 Quantitative Analysis of Single Molecule Trajectories in Mesoporous Silica

A quantitative analysis of the SMT data was undertaken to better understand the factors governing the dimensionality of single molecule diffusion and its evolution in time. The first step in this analysis was to separate the molecules into immobile and mobile fractions. The mobile fraction was then further separated into anisotropic (1D) and isotropic (2D) diffusing populations. To make these assignments, the mean localization precision for the molecules was first determined. The mean localization precision for each frame was obtained using the following equation:[161]

$$\sigma^2 = \frac{s^2 + a^2/12}{N} + \frac{8\pi s^4 b^2}{a^2 N^2} \qquad \text{(Eq. 5.1)}$$

where σ is the localization precision, *s* is the Gaussian width of the detected spot, *N* is the total number of photon counts in the spot area, and *a* is the pixel size. The background noise, b^2, was obtained from the rolling-ball background subtraction step described in Experimental Considerations. With the spot amplitude, *A*, obtained by fitting the individual spots to Gaussian functions, *N* was determined as follows:

$$N = 2\pi A s^2 \qquad \text{(Eq. 5.2)}$$

The localization precision for individual trajectories was estimated by averaging the mean localization precision values for corresponding frames. The mobility characteristics of individual molecules were determined by comparing σ to the localization precision across each trajectory,

σ^2, interpreted as the width of the trajectory, determined by the orgthogonal regression analysis. Molecules were first assigned to immobile and mobile fractions by comparing their MSD values to σ^2. Trajectories having MSD $> 4.6\sigma^2$ were classified as mobile, while those with smaller MSD were classified as immobile. Immobile molecules were excluded from further analysis.

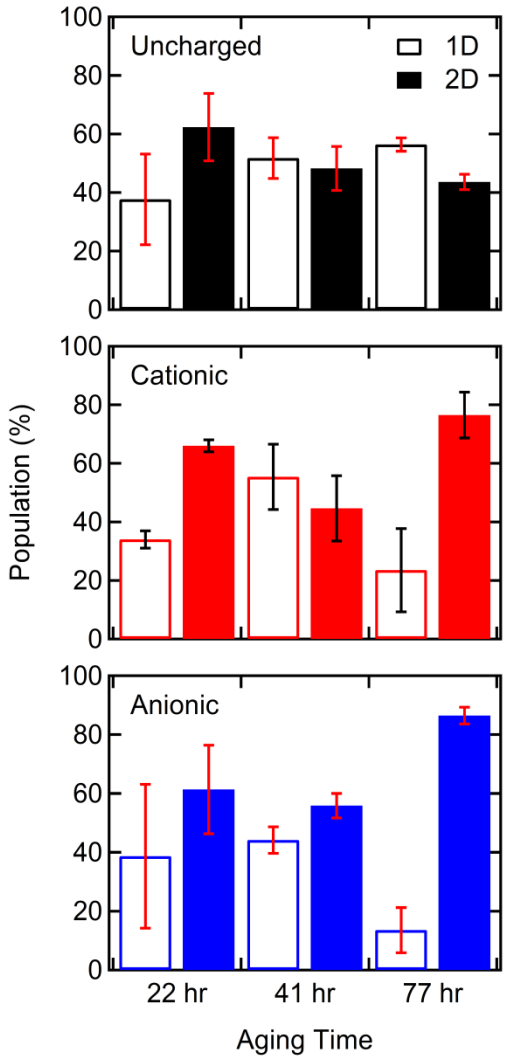

Figure 5.3 Fractions of 1D and 2D mobile populations for uncharged (top), cationic (middle) and anionic (bottom) PDI dyes obtained from flow-aligned mesoporous silica monoliths as a function of aging time. Results from 9 videos obtained from each samples were used to obtain each pair of 1D/2D bars. The empty bars represent the 1D mobile population and solid bars indicate the 2D mobile population. The error bars show the 95% confidence intervals.

The mobile molecules were next separated into 1D and 2D diffusing populations. For this

determination, σ_δ^2, and σ^2 were compared. Trajectories having $\sigma_\delta^2 > 4.6\sigma^2$ were assigned as 2D diffusion while all others were classified as 1D diffusion.

The mean populations of 1D and 2D diffusing molecules are plotted in **Figure 5.3** for all three dyes. As is readily apparent from these data, all samples showed some level of 1D diffusion, consistent with the presence of cylindrical pores/micelles in the samples at all aging times. These same data also reveal a monotonic, aging-time-dependent increase (at 90% confidence) in the population of uncharged PDI molecules exhibiting 1D diffusion. In contrast, the data obtained from the cationic and anionic dyes reveal aging-time-dependent increases in isotropic (2D) diffusion (at 80% and 95% confidence, respectively). Curiously, these results suggest that the uncharged dye becomes more strongly confined within the incorporated cylindrical nanostructures as the monoliths age while the charged dyes become progressively less confined.

Further evidence for the enhanced confinement of the uncharged molecules as a function of aging time was obtained through an analysis of the trajectory aspect ratios (length/width). As the dyes become better confined within the cylindrical pores, their trajectories are expected to appear more linear, yielding larger aspect ratios. Trajectory aspect ratios were calculated for both 1D and 2D diffusing molecules as the ratio σ_R/σ_δ. The ensemble averaged results are shown in **Figure 5.4**. For long trajectories, 2D diffusing molecules should produce aspect ratios near one. However, due to trajectory length limitations, fortuitous "elongation" often occurs and the mean value obtained for 2D trajectories was actually 2.4±1.7 (average and standard deviation). The 1D trajectories in all cases produced aspect ratios that were at least two-fold larger. Again, these data are consistent with the occurrence of some 1D diffusion in all samples at all aging times due to the presence of cylindrical pores.

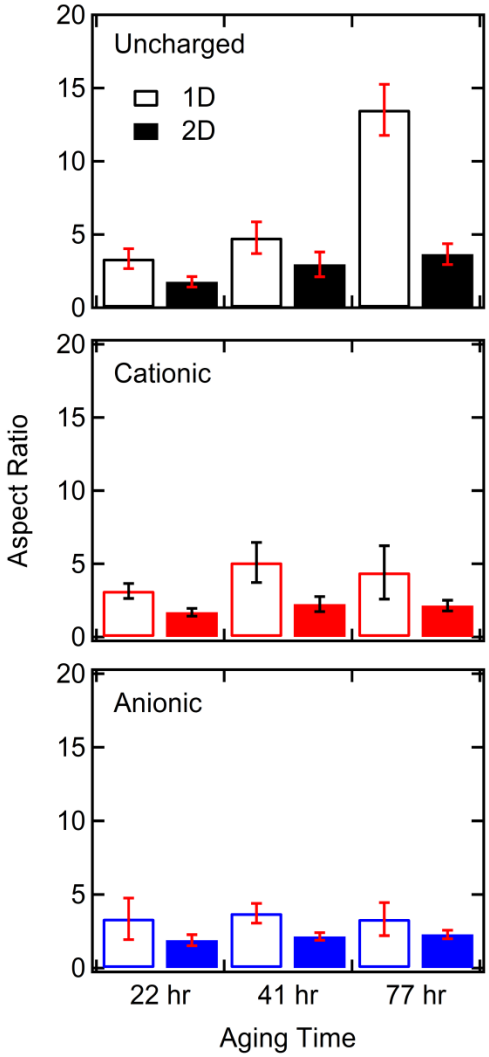

Figure 5.4 Mean trajectory aspect ratios for 1D and 2D trajectories of uncharged (top), cationic (middle) and anionic (bottom) PDI molecules as a function of aging time. The empty bars show the mean trajectory aspect ratios for 1D trajectories, while the solid bars depict the mean 2D trajectory aspect ratios. The error bars show the 95% confidence intervals.

The aspect ratios obtained from the 1D diffusing uncharged PDI dyes exhibit a clear increase (>99.9% confidence level) with aging time in a trend that parallels the increase in population of 1D diffusing molecules. The largest value is observed at 77 h aging. In contrast, the cationic dye shows a weaker trend towards increased aspect ratios with monolith age (< 90% confidence) while the anionic dye shows no trend whatsoever.

The greater trajectory aspect ratios observed for the uncharged dye, especially at 77 h aging, indicate that it spends significantly more time confined within the 1D silica pores. In the absence of photobleaching, the square of the trajectory aspect ratios for pure 1D diffusion should be proportional to the time the molecules spend confined within the pores (i.e., each trajectory ends when the molecule escapes the pore). At long aging times, for the uncharged dye, the average aspect ratio is ~13 while at short aging times, and for the charged molecules, the aspect ratios are ~ 3-4. Assuming no difference in diffusion coefficients for the different dyes (see below), the average length of time the uncharged dye spends confined to the 1D pores is estimated to be ~ 16 times longer at 77 h aging than at 22 h. With quantitative knowledge of the diffusion coefficients (see below), the mean time each molecule spends confined to the 1D pores can be estimated.

5. 3. 3 Comparisons with F127 Gels in the Absence of Silica

The SMT results obtained from mesoporous silica point to an apparent aging-time-dependent increase in confinement of the uncharged dye to 1D silica pores while the charged dyes exhibit an opposite trend towards decreasing confinement. To explore the role played by the F127 micelles in governing this behavior, SMT results were also obtained from silica-free F127 gels using the same series of dyes. Representative video images and trajectory plots are given in **Figure 5.5**. The uncharged PDI once again exhibited clear evidence of 1D diffusion, producing trajectories oriented approximately parallel to the flow alignment direction. It is noteworthy that these data were acquired immediately after filling of the microfluidic channels with the gels, providing support for the conclusion that flow aligned F127 micelles are present in the surfactant-templated silica monoliths even at very early aging times (see above).

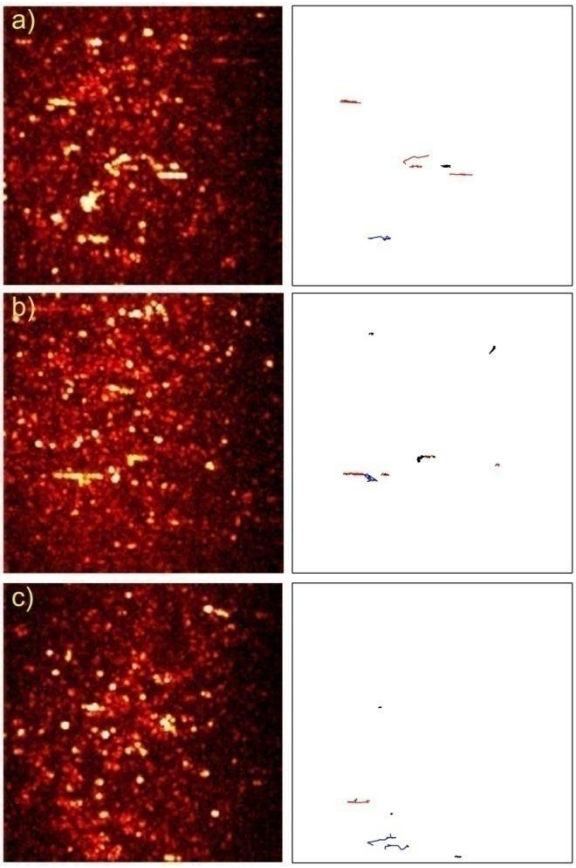

Figure 5.5 Representative TIRF-mode images (left) and corresponding trajectory plots (right) obtained from silica-free F127 gels doped with uncharged (a), cationic (b), and anionic (c) dye. Trajectories (≥ 10 frames in length) obtained by tracking the motions of the molecules were separated into immobile (black), and 1D (red) and 2D (blue) mobile populations. The images were obtained using the Z-project routine in ImageJ and depict the maximum intensity for each pixel in the associated videos.

Once again, the uncharged PDI exhibited the greatest level of anisotropic diffusion while 1D diffusion was less prevalent for the cationic and anionic PDI dyes. **Figure 5.6a** plots the populations of 1D and 2D diffusing species in these samples. Since there are no silica pores in these materials, confinement of the uncharged PDI motions to 1D is concluded to arise entirely from its partitioning into the hydrophobic core of the cylindrical F127 micelles, as has been reported previously.[122] Likewise, the increased prevalence of isotropic diffusion in the case of the charged dyes must result from enhanced partitioning out of these 1D nanostructures. The

trajectory aspect ratios observed in the F127 gels are plotted in **Figure 5.6b** and are similar for all three dyes, although the value for the uncharged dye is largest, consistent with its relatively strong confinement to the micelle core.[122] These aspect ratios are also similar to the values obtained at short aging times in the silica monoliths and much smaller than the value obtained for the uncharged dye at 77 h aging.

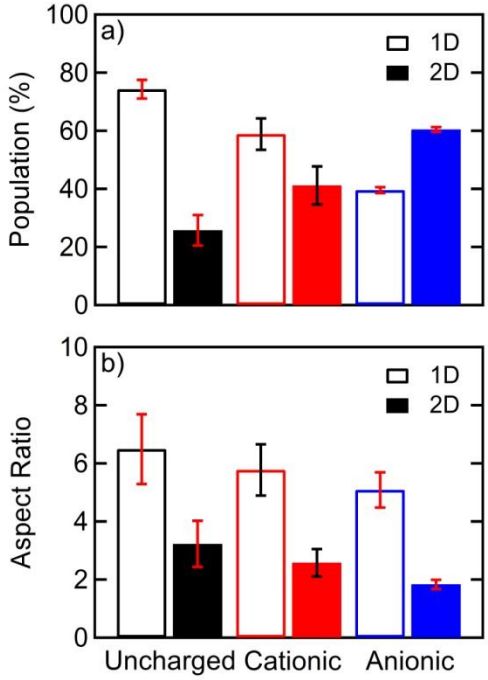

Figure 5.6 Fractions of 1D and 2D mobile populations (a), and mean trajectory aspect ratio of 1D and 2D trajectories (b) for uncharged (black), cationic (red) and anionic (blue) PDI molecules obtained from flow-aligned silica-free F127 gels. The solid bars depict the 1D mobile population and empty bars the 2D mobile population. The error bars show the 95% confidence intervals.

The aspect ratio results are again most consistent with the partitioning of the uncharged dye into the hydrophobic micelle core and the partitioning of the charged dyes into the hydrophilic micelle coronas. Indeed, probe molecules of different polarities have been shown previously to preferentially partition into the core or corona regions of F127 micelles.[162-164] It is concluded that

similar differences in the partitioning behaviors of the charged and uncharged PDIs must also be important in governing the dimensionalities of their motion in the mesoporous silica monoliths.

5. 3. 4 Diffusion Coefficient Measurements

The charged and uncharged dyes are expected to exhibit different diffusion coefficients in the different regions of the mesoporous silica samples. Dyes that partition differently between the F127 core and corona regions have been shown previously to yield different diffusion coefficients, reflecting the microviscosities of the local environments.[162-166] While diffusion coefficients can often be determined from SMT data,[142, 160] the dye motions in the present samples were too rapid to obtain accurate *D* values, as was shown previously for PDI diffusion in F127 gels.[122] Therefore, FCS measurements were instead employed to make these measurements. The same samples used in the SMT studies were also employed here, with FCS measurements made immediately after collection (within 1 h) of the SMT data.

Each time transient was autocorrelated as follows:

$$C(\tau) = \frac{\langle i(t)i(t+\tau)\rangle}{\langle i(t)\rangle^2} - 1 \qquad \text{(Eq. 5.3)}$$

where *i(t)* is the time transient data, *i(t+τ)* is the time transient with a time-delay, *τ*, and the brackets, ⟨ ⟩, indicate the average value is calculated over time. **Figure 5.7** shows representative autocorrelation data from the charged and uncharged PDIs at different monolith aging times. Each autocorrelation decay revealed clear evidence of two decay components. Based on the SMT data and the cylindrical structure of both the templated pores and F127 micelles, these were attributed to anisotropic and isotropic diffusion. The equation selected for fitting of these data included models for both types of diffusion, as given by Eq. 5.4: [49]

$$\mathrm{G}(\tau) = \frac{A}{(1+\tau D_f/\sigma^2)\sqrt{1+\tau D_f/z^2}} + \frac{B}{\sqrt{1+\tau D_s/\sigma^2}} \qquad \text{(Eq. 5.4)}$$

The diffusion coefficients for the fast and slow components of the decays are represented by D_f and D_s, respectively, while A and B provide information on the relative contributions of each. The lateral and longitudinal detection volume dimensions, σ and z, were determined by the calibration procedure described in Experimental Considerations.

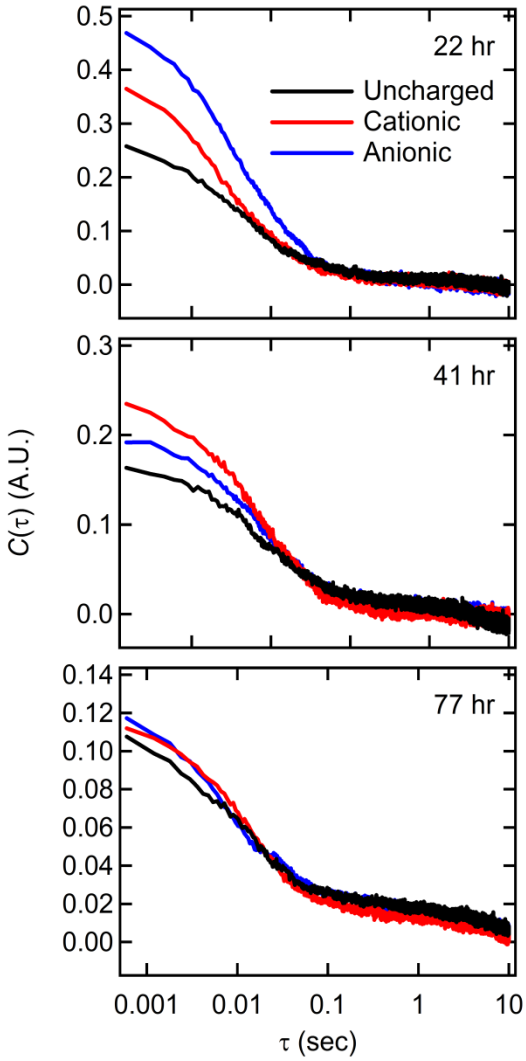

Figure 5.7 Representative autocorrelation data from charged and uncharged dye doped samples at each aging time.

Previous studies have reported faster diffusion by probe molecules in the F127 corona and slower diffusion in the micelle cores.[164, 166] Therefore, the faster decay was fitted to the 3D component of the model and the slower decay to the 1D component. While previous reports have

tried to deduce the dimensionality of motion from FCS decay profiles,[167-170] the signal-to-noise ratio in the present studies was too low for such a determination.

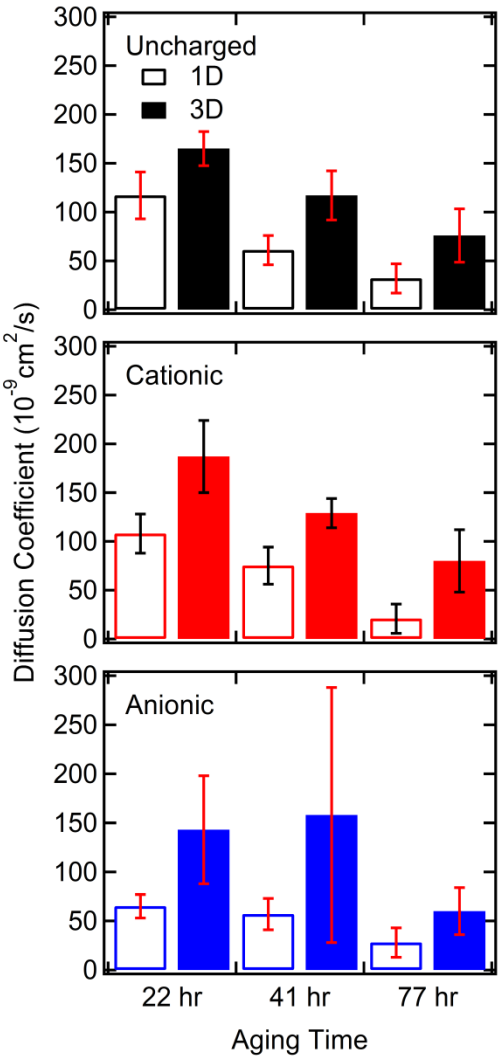

Figure 5.8 Mean diffusion coefficients estimated from FCS measurements of uncharged (top, black), cationic (middle, red), and anionic (bottom, blue) PDI dye molecules at different aging times. The error bars give the 95% confidence intervals.

The ensemble averaged diffusion coefficients determined from fits of the autocorrelation date are plotted in **Figure 5.8**. The diffusion coefficients for all three dyes depict clear trends towards smaller values with increasing monolith age. Such trends are consistent with a time-dependent increase in the microviscosities of the local environments in these materials, likely due

to evaporation of water and butanol from the monoliths, as well as conversion of the silica sol to a gel. Interestingly, the mean diffusion coefficients for isotropic and anisotropic diffusion are, individually, very similar for all three dyes. Thus, on average, the dyes all appear to be incorporated into gel regions of similar microviscosities, suggesting all three dyes spend appreciable time in the same regions within the silica pores.

5. 3. 5 Model for Confinement of Dyes in F127-Templated Mesoporous Silica

The results presented above point to a possible model for diffusion of the charged and uncharged PDIs in the F127-templated mesoporous silica monoliths. **Figure 5.9** provides a pictorial representation of this model. All three dyes are most likely associated with the F127 micelles filling the silica pores, as shown in **Figure 5.9a**. As suggested by their similar diffusion coefficients, and by the prevalence of 1D diffusion in all samples, both the charged and uncharged dyes likely spend significant time diffusing along the hydrophobic cores at the center of the silica pores, as depicted in **Figure 5.9b**. However, as evidenced by the greater fraction of isotropic diffusion in the case of the charged dyes, it is likely these molecules more readily partition out of the core into the hydrophilic corona nearest the silica pore walls. Once in these regions, the charged molecules can more readily access and pass through any defects (i.e., openings) in the pore walls. In fact, the coronas of individual micelles may extend through the pore walls and overlap with those of neighboring pores, greatly enhancing pore wall permeability.[171, 172] It is the enhanced crossing of the charged dyes between neighboring pores that likely leads to their isotropic motions, as shown in **Figure 5.9c**. The uncharged dye visits the corona regions much less frequently and thus exhibits longer 1D segments, as is consistent with the trajectory aspect ratio data in **Figure 5.4**, and the greater fraction of anisotropic diffusion, as demonstrated in **Figure 5.3**. The appearance of enhanced 1D diffusion in the case of the uncharged dye at 77 h aging is

likely due to its greater confinement to the hydrophobic core as the solvents present in the gel evaporate. Butanol is expected to evaporate much faster than water, with the increased fraction of water present driving the hydrophobic dye into more hydrophobic regions of the micelles. The opposite effect is observed for the charged dyes. As the butanol evaporates, these molecules partition more strongly to the hydrophilic, water-rich regions near the pore walls and an increase in isotropic diffusion is observed.

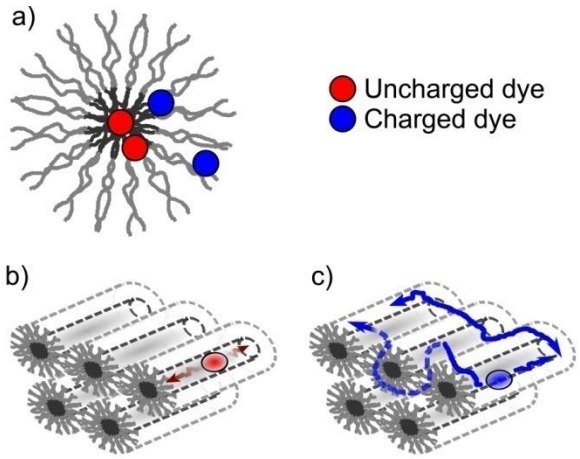

Figure 5.9 Model for probe localization (a), and diffusion modes for anisotropic (b) and apparent isotropic (c) diffusion. Uncharged dyes (red circles) are mainly localized in hydrophobic core of the F127 micelles (dark gray region) while the charged dyes (blue circles) preferentially partition into the hydrophilic corona region (light gray region).

5. 4 Conclusion

The diffusion behavior of fluorescent probe molecules in flow-aligned, surfactant-templated mesoporous silica monoliths has been studied by single molecule tracking and fluorescence correlation spectroscopy. These studies were undertaken to better understand the passage of molecules between neighboring cylindrical silica pores as manifested by the dimensionality of their diffusive motions. Uncharged, cationic, and anionic perylene diimide dyes were employed as probe molecules and their diffusive motions were studied as a function of

monolith aging time. SMT studies of the flow-aligned mesoporous silica demonstrated that all three dyes exhibited both apparent isotropic and anisotropic motions. The charged dyes exhibited a trend towards increasing isotropic motion with monolith age while the uncharged dye exhibited the opposite trend, in which the prevalence of 1D diffusion increased with monolith age. While their diffusion dimensionalities clearly differed, the diffusion coefficients of the three dyes, as measured by FCS, were very similar. It was concluded that all three dyes spend significant time diffusing along the hydrophobic cores of the F127 micelles within the silica pores. However, the uncharged dye more strongly partitions into the core while the charged dyes more readily access the hydrophilic corona nearest the pore walls. The latter allows the charged dyes to more easily pass through defects in the pore walls, leading to a greater fraction of apparent isotropic diffusion. The aging time dependence of the diffusion data were attributed to the uncharged dye becoming better confined to the pore axis and the charged dyes spending more time near the silica pore walls with monolith age.

This study provides important insight into the role of partitioning in governing anisotropic diffusion by solute molecules in aligned, solvent-filled surfactant-templated mesoporous silica. Molecules that partition to regions near the hydrophilic pore walls can more readily access and pass through defects in the silica walls. These molecules exhibit apparent isotropic diffusive motions. In contrast, nonpolar molecules will partition to less polar regions in the pores, preventing them from regularly passing between pores and better confining their motions to 1D along the long axis of the pores.

Chapter 6 - General Conclusions and Future Directions

This dissertation introduced a simple method to produce well-ordered mesoporous silica monoliths by flow alignment of viscous, surfactant-templated sols within microfluidic channels. SMT was employed for the quantitative characterization of the nanoscale structures and mass-transport properties of the surfactant-templated mesoporous silica monoliths. The remarkable capability of SMT for characterization of these materials was elucidated and was based on high-throughput single molecule imaging with high spatial resolution The data obtained allowed for the quantitative assessment of the local mass-transport and material properties in the silica materials. The properties of nanostructured materials were probed by monitoring the diffusive motions of individual probe molecules incorporated in the mesoporous silica materials.

Orthogonal regression analysis of these motions provided important parameters associated with local mass-transport and structural characteristics of the mesoporous silica monoliths. By fitting the single-molecule trajectories to linear functions, the analysis allowed for (i) the best fit locations of the single molecule spot in each video frame to be determined, (ii) the orientational angle of individual trajectories and the angular deviation from the average trajectory angle to be estimated, and (iii) the positional errors along and across the trajectory direction to be assessed. The trajectory angle afforded a quantitative measure of the in-plane orientation of the 1D nanostructures, and the angular distribution of individual mesopore orientation provided the orientational order via the 2D order parameter, $\langle P \rangle$. The angular and positional error afforded useful means to determine mobility and dimensionalities of the diffusive motions.

In Chapter 4, the utility of SMT for quantitative assessment of the 1D mesostructures was demonstrated for flow-aligned mesoporous silica monoliths incorporating nanochannels templated by cylindrical CTAB micelles. SMT imaging afforded direct visualization of the open mesopore

structures in the silica materials. The aging-time dependence of mesopore organization was then explored as a function of time between sol preparation and filling of the microfluidic channels. Orthogonal regression analysis was used to assess pore order and organization, based on the SMT data. The results showed that sols injected into the channels well before gelation incorporated large monodomains extending over several millimeters. These monodomains showed average pore alignment within a few degrees of the flow direction and yield aging-time-independent $\langle P \rangle$ values larger than ~ 0.80. In contrast, channels filled near/beyond the time of sol gelation produced monoliths with misaligned pores that were also more disordered, having $\langle P \rangle \approx 0.35$. To support the SMT results, SAXS anisotropy experiments were conducted and these data were consistent across the range of samples investigated.

SMT was also employed to directly visualize the diffusive motions of uncharged, cationic and anionic perylene diimide (PDI) dyes within the mesoporous silica monoliths (Chapter 5). SMT imaging was conducted as a function of aging time after filling of the microfluidic channels, and isotropic and anisotropic diffusion were found for all three dyes. The charged dyes exhibited predominantly isotropic motions that increased in prevalence with aging time. The isotropic motions of the charged dyes suggested that they readily pass through the silica pore walls. In contrast, the motions of the uncharged PDI became more anisotropic as the monoliths age. Results obtained from flow-aligned F127 gels in the absence of silica suggest that partitioning plays an important role in limiting passage of the PDIs between pores. The dye diffusion coefficients were estimated by FCS as a function of monolith age. All three dyes exhibited similar mean diffusion coefficients, D, that they diffuse through similar sample regions. Also, mean diffusion coefficients for all three dyes decreased with monolith age. The overall results suggest that enhanced partitioning of the charged PDI dyes into hydrophilic pore regions and better confinement of

uncharged PDI to the hydrophobic regions governs their observed motions. Confinement of the molecules by the silica pore walls appears to be less important. In fact, the silica pore wall appear to be permeable, as revealed by the motions of the charged dyes. The increase in isotropic motions and anisotropic motions with aging time for the charged and uncharged dyes, respectively, were attributed to changes in the pore composition in time: namely, due to the evaporation of solvent (i.e., butanol) from the pores.

This dissertation has described the application of SMT for the characterization of the mesopore organization in surfactant-templated mesoporous silica monoliths and diffusion behaviors of probe molecules in the mesoporous silica system. More importantly, these studies revealed two critical aspects in the fabrication and application of mesoporous silica materials. First, the aging-time dependence of pore order has provided information on the exact aging conditions that are required to produce highly ordered mesoporous silica materials incorporating well-aligned nanochannels. Second, the physical phenomena behind pore wall permeability in surfactant-templated mesoporous silica materials were elucidated. It was determined that the partitioning preference of incorporated probe molecules played a significant role. This finding indicates that the transport and diffusion processes of the incorporated reagents and analytes are governed not only by mesopore structure but also by the host-guest interaction in the mesoporous system.

This work will ultimately help establish a clear route to produce materials with well-defined mesopore structure. It also provides important new knowledge on factors that control mass-transport behavior within the mesoporous materials. In fact, these are crucial for many potential applications. For example, the production of highly organized cylindrical 1D mesopore structures combined with well-defined mass-transport characteristics would afford optimum performance for chemical separations. Also, release of drug molecules are precisely predicted and

controlled by well-characterized structural and diffusion properties of the mesoporous silica materials. In addition, more efficient, selective catalytic reactions can be expected in materials with more highly ordered porous structure and predictable mass transport pathways. Furthermore, findings from the present work should lead to improved strategies and theoretical models for developing novel mesoporous silica materials, and also contribute to improving conventional applications in separations, catalysis, sensing and drug delivery.

Considering the noteworthy capability of single molecule methods to monitor molecular motions at the single-molecule and single pore level, utilization of SMT for the investigation of mesoporous silica materials possessing a diversity of functionalities is essential. However, it is, obviously, challenging for thick monolithic materials, due to severe cracking and collapse of the monolith after drying and removal of incorporated surfactants. Therefore, it should be worthwhile to develop a method for fabrication of highly organized, true mesoporous silica monoliths having different pore sizes and chemical functionalities without cracking and collapse.

Chapter 7 - References

(1) Soler-illia, G. J. D.; Sanchez, C.; Lebeau, B.; Patarin, J. Chemical Strategies to Design Textured Materials: From Microporous and Mesoporous Oxides to Nanonetworks and Hierarchical Structures. *Chem. Rev.* **2002**, *102*, 4093-4138.

(2) Meynen, V.; Cool, P.; Vansant, E. F. Verified Syntheses of Mesoporous Materials. *Microporous Mesoporous Mater.* **2009**, *125*, 170-223.

(3) Kresge, C. T.; Leonowicz, M. E.; Roth, W. J.; Vartuli, J. C.; Beck, J. S. Ordered Mesoporous Molecular-Sieves Synthesized by a Liquid-Crystal Template Mechanism. *Nature* **1992**, *359*, 710-712.

(4) Beck, J. S.; Vartuli, J. C.; Roth, W. J.; Leonowicz, M. E.; Kresge, C. T.; Schmitt, K. D.; Chu, C. T. W.; Olson, D. H.; Sheppard, E. W.; Mccullen, S. B.; Higgins, J. B.; Schlenker, J. L. A New Family of Mesoporous Molecular-Sieves Prepared with Liquid-Crystal Templates. *J. Am. Chem. Soc.* **1992**, *114*, 10834-10843.

(5) Vartuli, J. C.; Schmitt, K. D.; Kresge, C. T.; Roth, W. J.; Leonowicz, M. E.; Mccullen, S. B.; Hellring, S. D.; Beck, J. S.; Schlenker, J. L.; Olson, D. H.; Sheppard, E. W. Effect of Surfactant Silica Molar Ratios on the Formation of Mesoporous Molecular-Sieves - Inorganic Mimicry of Surfactant Liquid-Crystal Phases and Mechanistic Implications. *Chem. Mater.* **1994**, *6*, 2317-2326.

(6) Han, Y.; Ying, J. Y. Generalized Fluorocarbon-Surfactant-Mediated Synthesis of Nanoparticles with various Mesoporous Structures. *Angew. Chem. , Int. Ed.* **2005**, *44*, 288-292.

(7) Song, S. W.; Hidajat, K.; Kawi, S. Functionalized SBA-15 Materials as Carriers for Controlled Drug Delivery: Influence of Surface Properties on Matrix-Drug Interactions. *Langmuir* **2005**, *21*, 9568-9575.

(8) Munoz, B.; Ramila, A.; Perez-Pariente, J.; Diaz, I.; Vallet-Regi, M. MCM-41 Organic Modification as Drug Delivery Rate Regulator. *Chem. Mater.* **2003**, *15*, 500-503.

(9) Corma, A. From Microporous to Mesoporous Molecular Sieve Materials and their use in Catalysis. *Chem. Rev.* **1997**, *97*, 2373-2419.

(10) Sayari, A.; Hamoudi, S. Periodic Mesoporous Silica-Based Organic - Inorganic Nanocomposite Materials. *Chem. Mater.* **2001**, *13*, 3151-3168.

(11) Ying, J. Y.; Mehnert, C. P.; Wong, M. S. Synthesis and Applications of Supramolecular-Templated Mesoporous Materials. *Angew. Chem. , Int. Ed.* **1999**, *38*, 56-77.

(12) Liu, X. W.; Li, J. W.; Zhou, L.; Huang, D. S.; Zhou, Y. P. Adsorption of CO2, CH4 and N-2 on Ordered Mesoporous Silica Molecular Sieve. *Chem. Phys. Lett.* **2005**, *415*, 198-201.

(13) Grun, M.; Kurganov, A. A.; Schacht, S.; Schuth, F.; Unger, K. K. Comparison of an Ordered Mesoporous Aluminosilicate, Silica, Alumina, Titania and Zirconia in Normal-Phase High-Performance Liquid Chromatography. *J. Chromatogr. A* **1996**, *740*, 1-9.

(14) Raja, R.; Thomas, J. M. Catalyst Design Strategies for Controlling Reactions in Microporous and Mesoporous Molecular-Sieves. *J. Mol. Catal. A: Chem.* **2002**, *181*, 3-14.

(15) Polarz, S.; Kuschel, A. Chemistry in Confining Reaction Fields with Special Emphasis on Nanoporous Materials. *Chem. - Eur. J.* **2008**, *14*, 9816-9829.

(16) Wu, C. G.; Bein, T. Conducting Polyaniline Filaments in a Mesoporous Channel Host. *Science* **1994**, *264*, 1757-1759.

(17) Llewellyn, P. L.; Ciesla, U.; Decher, H.; Stadler, R.; Schuth, F.; Unger, K. K. In *Mcm-41 and Related Materials as Media for Controlled Polymerization Processes;* Weitkamp, J Karge, HG Pfeifer, H Holderich,W., Ed.; STUDIES IN SURFACE SCIENCE AND CATALYSIS; 1994; Vol. 84, pp 2020.

(18) Cardin, D. J.; Constantine, S. P.; Gilbert, A.; Lay, A. K.; Alvaro, M.; Galletero, M. S.; Garcia, H.; Marquez, F. Polymerization of Alkynes in the Channels of Mesoporous Materials Containing Ni and Zn Cations: Almost Complete Filling of the Voids. *J. Am. Chem. Soc.* **2001**, *123*, 3141-3142.

(19) Lin, V. S. Y.; Radu, D. R.; Han, M. K.; Deng, W. H.; Kuroki, S.; Shanks, B. H.; Pruski, M. Oxidative Polymerization of 1,4-Diethynylbenzene into Highly Conjugated Poly(Phenylene Butadiynylene) within the Channels of Surface-Functionalized Mesoporous Silica and Alumina Materials. *J. Am. Chem. Soc.* **2002**, *124*, 9040-9041.

(20) Wu, C. G.; Bein, T. Conducting Carbon Wires in Ordered, Nanometer-Sized Channels. *Science* **1994**, *266*, 1013-1015.

(21) Bearzotti, A.; Bertolo, J. M.; Innocenzi, P.; Falcaro, P.; Traversa, E. Humidity Sensors Based on Mesoporous Silica Thin Films Synthesised by Block Copolymers. *J. Eur. Ceram. Soc.* **2004**, *24*, 1969-1972.

(22) Casasus, R.; Marcos, M. D.; Martinez-Manez, R.; Ros-Lis, J. V.; Soto, J.; Villaescusa, L. A.; Amoros, P.; Beltran, D.; Guillem, C.; Latorre, J. Toward the Development of Ionically Controlled Nanoscopic Molecular Gates. *J. Am. Chem. Soc.* **2004**, *126*, 8612-8613.

(23) Yantasee, W.; Lin, Y. H.; Li, X. H.; Fryxell, G. E.; Zemanian, T. S.; Viswanathan, V. V. Nanoengineered Electrochemical Sensor Based on Mesoporous Silica Thin-Film Functionalized with Thiol-Terminated Monolayer. *Analyst* **2003**, *128*, 899-904.

(24) Walcarius, A.; Bessiere, J. Electrochemistry with Mesoporous Silica: Selective Mercury(II) Binding. *Chem. Mater.* **1999**, *11*, 3009-3011.

(25) Hirano, T.; Yui, T.; Okazaki, K.; Kajino, T.; Fukushima, Y.; Inoue, H.; Torimoto, T.; Takagi, K. Photo-Induced Electron Migrations in the Nano-Cavities of Mesoporous Silica Sensitized by a Cationic Porphyrin Dye. *J. Nanosci. Nanotechnol.* **2009**, *9*, 495-500.

(26) Xia, Y. N.; Yang, P. D.; Sun, Y. G.; Wu, Y. Y.; Mayers, B.; Gates, B.; Yin, Y. D.; Kim, F.; Yan, Y. Q. One-Dimensional Nanostructures: Synthesis, Characterization, and Applications. *Adv Mater* **2003**, *15*, 353-389.

(27) Su, B.; Wu, Y.; Jiang, L. The Art of Aligning One-Dimensional (1D) Nanostructures. *Chem. Soc. Rev.* **2012**, *41*, 7832-7856.

(28) Walcarius, A.; Sibottier, E.; Etienne, M.; Ghanbaja, J. Electrochemically Assisted Self-Assembly of Mesoporous Silica Thin Films. *Nat. Mater.* **2007**, *6*, 602-608.

(29) Goux, A.; Etienne, M.; Aubert, E.; Lecomte, C.; Ghanbaja, J.; Walcarius, A. Oriented Mesoporous Silica Films obtained by Electro-Assisted Self-Assembly (EASA). *Chem. Mater.* **2009**, *21*, 731-741.

(30) Miyata, H. Epitaxial Growth of a Surfactant-Silica Mesostructure on Oriented Polymide Films. *Microporous Mesoporous Mater.* **2007**, *101*, 296-302.

(31) Miyata, H.; Kuroda, K. Preferred Alignment of Mesochannels in a Mesoporous Silica Film Grown on a Silicon (110) Surface. *J. Am. Chem. Soc.* **1999**, *121*, 7618-7624.

(32) Yamaguchi, A.; Teramae, N. Fabrication and Analytical Applications of Hybrid Mesoporous Membranes. *Anal. Sci.* **2008**, *24*, 25-30.

(33) Yamaguchi, A.; Kaneda, H.; Fu, W.; Teramae, N. Structural Control of Surfactant-Templated Mesoporous Silica Formed Inside Columnar Alumina Pores. *Adv Mater* **2008**, *20*, 1034-1037.

(34) Melosh, N. A.; Davidson, P.; Feng, P.; Pine, D. J.; Chmelka, B. F. Macroscopic Shear Alignment of Bulk Transparent Mesostructured Silica. *J. Am. Chem. Soc.* **2001**, *123*, 1240-1241.

(35) Tolbert, S. H.; Firouzi, A.; Stucky, G. D.; Chmelka, B. F. Magnetic Field Alignment of Ordered Silicate-Surfactant Composites and Mesoporous Silica. *Science* **1997**, *278*, 264-268.

(36) Park, S. C.; Ito, T.; Higgins, D. A. Single Molecule Tracking Studies of Flow-Aligned Mesoporous Silica Monoliths: Aging-Time Dependence of Pore Order. *J. Phys. Chem. B* **2013**, *117*, 4222-4230.

(37) Stallmach, F.; Karger, J.; Krause, C.; Jeschke, M.; Oberhagemann, U. Evidence of Anisotropic Self-Diffusion of Guest Molecules in Nanoporous Materials of MCM-41 Type. *J. Am. Chem. Soc.* **2000**, *122*, 9237-9242.

(38) Tran-Ba, K. H.; Higgins, D. A.; Ito, T. Single-Molecule Tracking Studies of Flow-Induced Microdomain Alignment in Cylinder-Forming Polystyrene-Poly(Ethylene Oxide) Diblock Copolymer Films. *J. Phys. Chem. B* **2014**, *118*, 11406-11415.

(39) Jung, C.; Kirstein, J.; Platschek, B.; Bein, T.; Budde, M.; Frank, I.; Muellen, K.; Michaelis, J.; Bräuchle, C. Diffusion of Oriented Single Molecules with Switchable Mobility in Networks of Long Unidimensional Nanochannels. *J. Am. Chem. Soc.* **2008**, *130*, 1638-1648.

(40) Ito, S.; Fukuya, S.; Kusumi, T.; Ishibashi, Y.; Miyasaka, H.; Goto, Y.; Ikai, M.; Tani, T.; Inagaki, S. Microscopic Structure and Mobility of Guest Molecules in Mesoporous Hybrid Organosilica: Evaluation with Single-Molecule Tracking. *J. Phys. Chem. C* **2009**, *113*, 11884-11891.

(41) Higgins, D. A.; Tran-Ba, K. H.; Ito, T. Following Single Molecules to a Better Understanding of Self-Assembled One-Dimensional Nanostructures. *J. Phys. Chem. Lett.* **2013**, *4*, 3095-3103.

(42) Pramanik, R.; Ito, T.; Higgins, D. A. Molecular Length Dependence of Single Molecule Wobbling within Surfactant- and Solvent-Filled Silica Mesopores. *J. Phys. Chem. C* **2013**, *117*, 15438-15446.

(43) Pramanik, R.; Ito, T.; Higgins, D. A. Single Molecule Wobbling in Cylindrical Mesopores. *J. Phys. Chem. C* **2013**, *117*, 3668-3673.

(44) Yorulmaz, M.; Kiraz, A.; Demirel, A. L. Motion of Single Terrylene Molecules in Confined Channels of Poly(Butadiene)-Poly(Ethylene Oxide) Diblock Copolymer. *J. Phys. Chem. B* **2009**, *113*, 9640-9643.

(45) Liao, Y.; Yang, S. K.; Koh, K.; Matzger, A. J.; Biteen, J. S. Heterogeneous Single-Molecule Diffusion in One-, Two-, and Three-Dimensional Microporous Coordination Polymers: Directional, Trapped, and Immobile Guests. *Nano Lett.* **2012**, *12*, 3080-3085.

(46) Tran-Ba, K. H.; Finley, J. J.; Higgins, D. A.; Ito, T. Single-Molecule Tracking Studies of Millimeter-Scale Cylindrical Domain Alignment in Polystyrene-Poly(Ethylene Oxide) Diblock Copolymer Films Induced by Solvent Vapor Penetration. *J. Phys. Chem. Lett.* **2012**, *3*, 1968-1973.

(47) Davies, M.; Ruehle, B.; Li, C.; Muellen, K.; Bein, T.; Bräuchle, C. Insights into Nanoscale Electrophoresis of Single Dye Molecules in Highly Oriented Mesoporous Silica Channels. *J. Phys. Chem. C* **2014**, *118*, 24013-24024.

(48) Holmqvist, P.; Alexandridis, P.; Lindman, B. Phase Behavior and Structure of Ternary Amphiphilic Block Copolymer-Alkanol-Water Systems: Comparison of Poly(Ethylene Oxide) Poly(Propylene Oxide) to Poly(Ethylene Oxide) Poly(Tetrahydrofuran) Copolymers. *Langmuir* **1997**, *13*, 2471-2479.

(49) Higgins, D. A.; Park, S. C.; Tran-Ba, K. H.; Ito, T. Single-Molecule Investigations of Morphology and Mass Transport Dynamics in Nanostructured Materials. *Annu. Rev. Anal. Chem.* **2015**, *8*, 193-216.

(50) Tran-Ba, K. H.; Everett, T. A.; Ito, T.; Higgins, D. A. Trajectory Angle Determination in One Dimensional Single Molecule Tracking Data by Orthogonal Regression Analysis. *Phys. Chem. Chem. Phys.* **2011**, *13*, 1827-35.

(51) Kocherbitov, V.; Alfredsson, V. Assessment of Porosities of SBA-15 and MCM-41 using Water Sorption Calorimetry. *Langmuir* **2011**, *27*, 3889-3897.

(52) Alsyouri, H.; Gobin, O. C.; Jentys, A.; Lercher, J. A. Diffusion in Circularly Ordered Mesoporous Silica Fibers. *J. Phys. Chem. C* **2011**, *115*, 8602-8612.

(53) Stempniewicz, M.; Rohwerder, M.; Marlow, F. Release from Silica SBA-3-Like Mesoporous Fibers: Cross-Wall Transport and External Diffusion Barrier. *ChemPhysChem* **2007**, *8*, 188-194.

(54) Stempniewicz, M.; Khalil, A. S. G.; Rohwerder, M.; Marlow, F. Diffusion in Coiled Pores - Learning from Microrelease and Microsurgery. *J. Am. Chem. Soc.* **2007**, *129*, 10561-10566.

(55) Mann, S.; Burkett, S. L.; Davis, S. A.; Fowler, C. E.; Mendelson, N. H.; Sims, S. D.; Walsh, D.; Whilton, N. T. Sol-Gel Synthesis of Organized Matter. *Chem. Mater.* **1997**, *9*, 2300-2310.

(56) Antonietti, M.; Berton, B.; Goltner, C.; Hentze, H. P. Synthesis of Mesoporous Silica with Large Pores and Bimodal Pore Size Distribution by Templating of Polymer Latices. *Adv Mater* **1998**, *10*, 154-159.

(57) Bagshaw, S. A.; Prouzet, E.; Pinnavaia, T. J. Templating of Mesoporous Molecular-Sieves by Nonionic Polyethylene Oxide Surfactants. *Science* **1995**, *269*, 1242-1244.

(58) Slowing, I. I.; Trewyn, B. G.; Giri, S.; Lin, V. S. -. Mesoporous Silica Nanoparticles for Drug Delivery and Biosensing Applications. *Adv. Funct. Mater.* **2007**, *17*, 1225-1236.

(59) Slowing, I. I.; Vivero-Escoto, J. L.; Wu, C.; Lin, V. S. -. Mesoporous Silica Nanoparticles as Controlled Release Drug Delivery and Gene Transfection Carriers. *Adv. Drug Deliv. Rev.* **2008**, *60*, 1278-1288.

(60) Walcarius, A.; Collinson, M. M. Analytical Chemistry with Silica Sol-Gels: Traditional Routes to New Materials for Chemical Analysis. *Annu. Rev. Anal. Chem.* **2009**, *2*, 121-143.

(61) Brinker, C.; Scherer, G. In *Sol-Gel Science: The Physics and Chemistry of Sol-Gel Processing.* Section Title: Ceramics; Academic: New York, 1990; .

(62) Hench, L. L.; West, J. K. The Sol-Gel Process. *Chem. Rev.* **1990**, *90*, 33-72.

(63) Lofgreen, J. E.; Ozin, G. A. Controlling Morphology and Porosity to Improve Performance of Molecularly Imprinted Sol-Gel Silica. *Chem. Soc. Rev.* **2014**, *43*, 911-933.

(64) Ito, S.; Kusumi, T.; Takei, S.; Miyasaka, H. Diffusion Processes of Single Fluorescent Molecules in a Polymer-Based Thin Material with Three-Dimensional Network. *Chem. Commun.* **2009**, , 6165-6167.

(65) Collinson, M. M. In *In Structure, chemistry, and applications of sol-gel derived materials.* Section Title: Optical, Electron, and Mass Spectroscopy and Other Related Properties; 2001; Vol. 5, pp 163-194.

(66) Ye, F.; Collinson, M. M.; Higgins, D. A. What can be Learned from Single Molecule Spectroscopy? Applications to Sol-Gel-Derived Silica Materials. *Phys. Chem. Chem. Phys.* **2009**, *11*, 66-82.

(67) Hoffmann, F.; Cornelius, M.; Morell, J.; Froeba, M. Silica-Based Mesoporous Organic-Inorganic Hybrid Materials. *Angew. Chem. , Int. Ed.* **2006**, *45*, 3216-3251.

(68) Attard, G. S.; Glyde, J. C.; Goltner, C. G. Liquid-Crystalline Phases as Templates for the Synthesis of Mesoporous Silica. *Nature* **1995**, *378*, 366-368.

(69) Goltner, C.; Antonietti, M. Mesoporous Materials by Templating of Liquid Crystalline Phases. *Adv Mater* **1997**, *9*, 431-436.

(70) Monnier, A.; Schuth, F.; Huo, Q.; Kumar, D.; Margolese, D.; Maxwell, R. S.; Stucky, G. D.; Krishnamurty, M.; Petroff, P.; Firouzi, A.; Janicke, M.; Chmelka, B. F. Cooperative Formation of Inorganic-Organic Interfaces in the Synthesis of Silicate Mesostructures. *Science* **1993**, *261*, 1299-1303.

(71) Boissiere, C.; Larbot, A.; van der Lee, A.; Kooyman, P. J.; Prouzet, E. A New Synthesis of Mesoporous MSU-X Silica Controlled by a Two-Step Pathway. *Chem. Mater.* **2000**, *12*, 2902-2913.

(72) Firouzi, A.; Kumar, D.; Bull, L. M.; Besier, T.; Sieger, P.; Huo, Q.; Walker, S. A.; Zasadzinski, J. A.; Glinka, C.; Nicol, J.; Margolese, D.; Stucky, G. D.; Chmelka, B. F. Cooperative Organization of Inorganic-Surfactant and Biomimetic Assemblies. *Science* **1995**, *267*, 1138-1143.

(73) Dong, W.; Sun, Y.; Lee, C. W.; Hua, W.; Lu, X.; Shi, Y.; Zhang, S.; Chen, J.; Zhao, D. Controllable and Repeatable Synthesis of Thermally Stable Anatase Nanocrystal-Silica Composites with Highly Ordered Hexagonal Mesostructures. *J. Am. Chem. Soc.* **2007**, *129*, 13894-13904.

(74) Meng, Y.; Gu, D.; Zhang, F. Q.; Shi, Y. F.; Yang, H. F.; Li, Z.; Yu, C. Z.; Tu, B.; Zhao, D. Y. Ordered Mesoporous Polymers and Homologous Carbon Frameworks: Amphiphilic Surfactant Templating and Direct Transformation. *Angew. Chem. , Int. Ed.* **2005**, *44*, 7053-7059.

(75) Schacht, S.; Huo, Q.; VoigtMartin, I. G.; Stucky, G. D.; Schuth, F. Oil-Water Interface Templating of Mesoporous Macroscale Structures. *Science* **1996**, *273*, 768-771.

(76) Lu, Y. F.; Fan, H. Y.; Stump, A.; Ward, T. L.; Rieker, T.; Brinker, C. J. Aerosol-Assisted Self-Assembly of Mesostructured Spherical Nanoparticles. *Nature* **1999**, *398*, 223-226.

(77) Davis, S. A.; Burkett, S. L.; Mendelson, N. H.; Mann, S. Bacterial Templating of Ordered Macrostructures in Silica and Silica-Surfactant Mesophases. *Nature* **1997**, *385*, 420-423.

(78) Marlow, F.; Leike, I.; Weidenthaler, C.; Lehmann, C. W.; Wilczok, U. Mesostructured Silica Fibers: Ring Structures in Reciprocal Space. *Adv Mater* **2001**, *13*, 307-310.

(79) Melosh, N. A.; Lipic, P.; Bates, F. S.; Wudl, F.; Stucky, G. D.; Fredrickson, G. H.; Chmelka, B. F. Molecular and Mesoscopic Structures of Transparent Block Copolymer-Silica Monoliths. *Macromolecules* **1999**, *32*, 4332-4342.

(80) Yang, H. F.; Shi, Q. H.; Tian, B. Z.; Xie, S. H.; Zhang, F. Q.; Yan, Y.; Tu, B.; Zhao, D. Y. A Fast Way for Preparing Crack-Free Mesostructured Silica Monolith. *Chem. Mater.* **2003**, *15*, 536-541.

(81) Huo, Q. S.; Margolese, D. I.; Stucky, G. D. Surfactant Control of Phases in the Synthesis of Mesoporous Silica-Based Materials. *Chem. Mater.* **1996**, *8*, 1147-1160.

(82) Zhao, D. Y.; Feng, J. L.; Huo, Q. S.; Melosh, N.; Fredrickson, G. H.; Chmelka, B. F.; Stucky, G. D. Triblock Copolymer Syntheses of Mesoporous Silica with Periodic 50 to 300 Angstrom Pores. *Science* **1998**, *279*, 548-552.

(83) Israelachvili, J. N.; Mitchell, D. J.; Ninham, B. W. Theory of Self-Assembly of Hydrocarbon Amphiphiles into Micelles and Bilayers. *J. Chem. Soc. , Faraday Trans. 2* **1976**, *72*, 1525-1568.

(84) Zhang, A.; Zhang, Y.; Xing, N.; Hou, K.; Guo, X. Hollow Silica Spheres with a Novel Mesoporous Shell Perforated Vertically by Hexagonally Arrayed Cylindrical Nanochannels. *Chem. Mater.* **2009**, *21*, 4122-4126.

(85) Primo, A.; Liebel, M.; Quignard, F. Palladium Coordination Biopolymer: A Versatile Access to Highly Porous Dispersed Catalyst for Suzuki Reaction. *Chem. Mater.* **2009**, *21*, 621-627.

(86) Djojoputro, H.; Zhou, X. F.; Qiao, S. Z.; Wang, L. Z.; Yu, C. Z.; Lu, G. Q. Periodic Mesoporous Organosilica Hollow Spheres with Tunable Wall Thickness. *J. Am. Chem. Soc.* **2006**, *128*, 6320-6321.

(87) Friberg, S. E.; van Oss, C. J. Physico-Chemical Properties of Selected Anionic Cationic and Nonionic Surfactants. *J. Dispersion Sci. Technol.* **1995**, *16*, 99-101.

(88) Ruehle, B.; Davies, M.; Lebold, T.; Bräuchle, C.; Bein, T. Highly Oriented Mesoporous Silica Channels Synthesized in Microgrooves and Visualized with Single-Molecule Diffusion. *ACS Nano* **2012**, *6*, 1948-1960.

(89) Trau, M.; Yao, N.; Kim, E.; Xia, Y. N.; Whitesides, G. M.; Aksay, I. A. Microscopic Patterning of Orientated Mesoscopic Silica through Guided Growth. *Nature* **1997**, *390*, 674-676.

(90) Huh, S.; Wiench, J. W.; Yoo, J. C.; Pruski, M.; Lin, V. S. Y. Organic Functionalization and Morphology Control of Mesoporous Silicas Via a Co-Condensation Synthesis Method. *Chem. Mater.* **2003**, *15*, 4247-4256.

(91) Huo, Q. S.; Zhao, D. Y.; Feng, J. L.; Weston, K.; Buratto, S. K.; Stucky, G. D.; Schacht, S.; Schuth, F. Room Temperature Growth of Mesoporous Silica Fibers: A New High-Surface-Area Optical Waveguide. *Adv Mater* **1997**, *9*, 974-978.

(92) Wang, J. F.; Zhang, J. P.; Asoo, B. Y.; Stucky, G. D. Structure-Selective Synthesis of mesostructured/mesoporous Silica Nanofibers. *J. Am. Chem. Soc.* **2003**, *125*, 13966-13967.

(93) Marlow, F.; McGehee, M. D.; Zhao, D. Y.; Chmelka, B. F.; Stucky, G. D. Doped Mesoporous Silica Fibers: A New Laser Material. *Adv Mater* **1999**, *11*, 632-636.

(94) Kleitz, F.; Marlow, F.; Stucky, G. D.; Schuth, F. Mesoporous Silica Fibers: Synthesis, Internal Structure, and Growth Kinetics. *Chem. Mater.* **2001**, *13*, 3587-3595.

(95) Wang, J. F.; Tsung, C. K.; Hong, W. B.; Wu, Y. Y.; Tang, J.; Stucky, G. D. Synthesis of Mesoporous Silica Nanofibers with Controlled Pore Architectures. *Chem. Mater.* **2004**, *16*, 5169-5181.

(96) Rankin, S. E.; Malanoski, A. P.; Van Swol, F. Monte Carlo Simulation of Amphiphile Self-Assembly during Dip Coating. *Mater. Res. Soc. Symp. Proc.* **2001**, *636*, D1.2/1-D1.2/6.

(97) Tian, F.; Luo, Y.; Zhang, X. Curvature Modulates the Self-Assembly of Amphiphilic Molecules. *J. Chem. Phys.* **2010**, *133*, 144701.

(98) Fukuoka, A.; Miyata, H.; Kuroda, K. Alignment Control of a Cyanine Dye using a Mesoporous Silica Film with Uniaxially Aligned Mesochannels. *Chem. Commun.* **2003**, , 284-285.

(99) Miyata, H.; Kuroda, K. Formation of a Continuous Mesoporous Silica Film with Fully Aligned Mesochannels on a Glass Substrate. *Chem. Mater.* **2000**, *12*, 49-54.

(100) Miyata, H.; Noma, T.; Watanabe, M.; Kuroda, K. Preparation of Mesoporous Silica Films with Fully Aligned Large Mesochannels using Nonionic Surfactants. *Chem. Mater.* **2002**, *14*, 766-772.

(101) Yamaguchi, A.; Uejo, F.; Yoda, T.; Uchida, T.; Tanamura, Y.; Yamashita, T.; Teramae, N. Self-Assembly of a Silica-Surfactant Nanocomposite in a Porous Alumina Membrane. *Nat. Mater.* **2004**, *3*, 337-341.

(102) Wu, Y. Y.; Cheng, G. S.; Katsov, K.; Sides, S. W.; Wang, J. F.; Tang, J.; Fredrickson, G. H.; Moskovits, M.; Stucky, G. D. Composite Mesostructures by Nano-Confinement. *Nat. Mater.* **2004**, *3*, 816-822.

(103) Platschek, B.; Petkov, N.; Bein, T. Tuning the Structure and Orientation of Hexagonally Ordered Mesoporous Channels in Anodic Alumina Membrane Hosts: A 2D Small-Angle X-Ray Scattering Study. *Angew. Chem. , Int. Ed.* **2006**, *45*, 1134-1138.

(104) Lu, Q. Y.; Gao, F.; Komarneni, S.; Mallouk, T. E. Ordered SBA-15 Nanorod Arrays Inside a Porous Alumina Membrane. *J. Am. Chem. Soc.* **2004**, *126*, 8650-8651.

(105) Wang, D. H.; Kou, R.; Yang, Z. L.; He, J. B.; Yang, Z. Z.; Lu, Y. F. Hierachical Mesoporous Silica Wires by Confined Assembly. *Chem. Commun.* **2005**, , 166-167.

(106) Lai, P.; Hu, M. Z.; Shi, D.; Blom, D. STEM Characterization on Silica Nanowires with New Mesopore Structures by Space-Confined Self-Assembly within Nano-Scale Channels. *Chem. Commun.* **2008**, , 1338-1340.

(107) Wu, C.; Ohsuna, T.; Edura, T.; Kuroda, K. Orientational Control of Hexagonally Packed Silica Mesochannels in Lithographically Designed Confined Nanospaces. *Angew. Chem. , Int. Ed.* **2007**, *46*, 5364-5368.

(108) Yang, H.; Kuperman, A.; Coombs, N.; MamicheAfara, S.; Ozin, G. A. Synthesis of Oriented Films of Mesoporous Silica on Mica. *Nature* **1996**, *379*, 703-705.

(109) Aksay, I. A.; Trau, M.; Manne, S.; Honma, I.; Yao, N.; Zhou, L.; Fenter, P.; Eisenberger, P. M.; Gruner, S. M. Biomimetic Pathways for Assembling Inorganic Thin Films. *Science* **1996**, *273*, 892-898.

(110) Fukumoto, H.; Nagano, S.; Kawatsuki, N.; Seki, T. Photo-Alignment Behavior of Mesoporous Silica Thin Films Synthesized on a Photo-Cross-Linkable Polymer Film. *Chemistry of Materials* **2006**, *18*, 1226-1234.

(111) Yamauchi, Y.; Nagaura, T.; Inoue, S. Oriented Growth of Small Mesochannels Utilizing a Porous Anodic Alumina Substrate: Preparation of Continuous Film with Standing Mesochannels. *Chem. - Asian J.* **2009**, *4*, 1059-1063.

(112) Yamauchi, Y.; Nagaura, T.; Ishikawa, A.; Chikyow, T.; Inoue, S. Evolution of Standing Mesochannels on Porous Anodic Alumina Substrates with Designed Conical Holes. *J. Am. Chem. Soc.* **2008**, *130*, 10165-10170.

(113) Hara, M.; Nagano, S.; Seki, T. Pi-Pi Interaction-Induced Vertical Alignment of Silica Mesochannels Templated by a Discotic Lyotropic Liquid Crystal. *J. Am. Chem. Soc.* **2010**, *132*, 13654-13656.

(114) Firouzi, A.; Schaefer, D. J.; Tolbert, S. H.; Stucky, G. D.; Chmelka, B. F. Magnetic-Field-Induced Orientational Ordering of Alkaline Lyotropic Silicate - Surfactant Liquid Crystals. *J. Am. Chem. Soc.* **1997**, *119*, 9466-9477.

(115) Rapp, A.; Ermolaev, K.; Fung, B. M. The Alignment of Lyotropic Liquid Crystals Formed by Hexadecyltrimethylammonium Bromide in D2O in a Magnetic Field. *J Phys Chem B* **1999**, *103*, 1705-1711.

(116) Yamauchi, Y.; Sawada, M.; Noma, T.; Ito, H.; Furumi, S.; Sakka, Y.; Kuroda, K. Orientation of Mesochannels in Continuous Mesoporous Silica Films by a High Magnetic Field. *J. Mater. Chem.* **2005**, *15*, 1137-1140.

(117) Yamauchi, Y.; Sawada, M.; Sugiyama, A.; Osaka, T.; Sakka, Y.; Kuroda, K. Magnetically Induced Orientation of Mesochannels in 2D-Hexagonal Mesoporous Silica Films. *J. Mater. Chem.* **2006**, *16*, 3693-3700.

(118) Yamauchi, Y.; Sawada, M.; Komatsu, M.; Sugiyama, A.; Osaka, T.; Hirota, N.; Sakka, Y.; Kuroda, K. Magnetically Induced Orientation of Mesochannels in Mesoporous Silica Films at 30 Tesla. *Chem. - Asian J.* **2007**, *2*, 1505-1512.

(119) Su, B.; Lu, X.; Lu, Q. A Facile Method to Prepare Macroscopically Oriented Mesostructured Silica Film: Controlling the Orientation of Mesochannels in Multilayer Films by Air Flow. *J. Am. Chem. Soc.* **2008**, *130*, 14356-14357.

(120) Woolley, A. T.; Kelly, R. T. Deposition and Characterization of Extended Single-Stranded DNA Molecules on Surfaces. *Nano Letters* **2001**, *1*, 345-348.

(121) Kirstein, J.; Platschek, B.; Jung, C.; Brown, R.; Bein, T.; Brauchle, C. Exploration of Nanostructured Channel Systems with Single-Molecule Probes. *Nat. Mater.* **2007**, *6*, 303-310.

(122) Kirkeminde, A. W.; Torres, T.; Ito, T.; Higgins, D. A. Multiple Diffusion Pathways in Pluronic F127 Mesophases Revealed by Single Molecule Tracking and Fluorescence Correlation Spectroscopy. *J. Phys. Chem. B* **2011**, *115*, 12736-12743.

(123) Wanka, G.; Hoffmann, H.; Ulbricht, W. Phase-Diagrams and Aggregation Behavior of Poly(Oxyethylene)-Poly(Oxypropylene)-Poly(Oxyethylene) Triblock Copolymers in Aqueous-Solutions. *Macromolecules* **1994**, *27*, 4145-4159.

(124) Alexandridis, P.; Hatton, T. A. Poly(Ethylene Oxide)-Poly(Propylene Oxide)-Poly(Ethylene Oxide) Block-Copolymer Surfactants in Aqueous-Solutions and at Interfaces - Thermodynamics, Structure, Dynamics, and Modeling. *Colloids Surf. , A* **1995**, *96*, 1-46.

(125) Almgren, M.; Brown, W.; Hvidt, S. Self-Aggregation and Phase-Behavior of Poly(Ethylene Oxide) Poly(Propylene Oxide) Poly(Ethylene Oxide) Block-Copolymers in Aqueous-Solution. *Colloid Polym. Sci.* **1995**, *273*, 2-15.

(126) Marlow, F.; Spliethoff, B.; Tesche, B.; Zhao, D. Y. The Internal Architecture of Mesoporous Silica Fibers. *Adv Mater* **2000**, *12*, 961-+.

(127) Doshi, D. A.; Gibaud, A.; Goletto, V.; Lu, M. C.; Gerung, H.; Ocko, B.; Han, S. M.; Brinker, C. J. Peering into the Self-Assembly of Surfactant Templated Thin-Film Silica Mesophases. *J. Am. Chem. Soc.* **2003**, *125*, 11646-11655.

(128) Weitzel, C. R.; Everett, T. A.; Higgins, D. A. Aggregation and its Influence on Macroscopic in-Plane Organization in Thin Films of Electrostatically Self-Assembled Perylene-Diimide/Polyelectrolyte Nanofibers. *Langmuir* **2009**, *25*, 1188-1195.

(129) Papathanassoglou, D. A.; Vohnsen, B. Direct Visualization of Evanescent Optical Waves. *Am. J. Phys.* **2003**, *71*, 670-677.

(130) Ahmad, M.; Hench, L. L. Effect of Taper Geometries and Launch Angle on Evanescent Wave Penetration Depth in Optical Fibers. *Biosens. Bioelectron.* **2005**, *20*, 1312-1319.

(131) Deming, W. E. In *Statistical Adjustment of Data.* Section Title: General and Physical Chemistry; Wiley: New York, .

(132) Hood, K.; Nix, B. A. J.; Iles, T. C. Asymptotic Information and Variance-Covariance Matrices for the Linear Structural Model. *J Roy Stat Soc D-Sta* **1999**, *48*, 477-493.

(133) Dunn, G. In *Statistical Evaluation of Measurement Errors: Design and Analysis of Reliability Studies;* Arnold: London, 2004; .

(134) Selvam, P.; Bhatia, S. K.; Sonwane, C. G. Recent Advances in Processing and Characterization of Periodic Mesoporous MCM-41 Silicate Molecular Sieves. *Ind Eng Chem Res* **2001**, *40*, 3237-3261.

(135) Fan, J.; Boettcher, S. W.; Tsung, C.; Shi, Q.; Schierhorn, M.; Stucky, G. D. Field-Directed and Confined Molecular Assembly of Mesostructured Materials: Basic Principles and New Opportunities. *Chem. Mater.* **2008**, *20*, 909-921.

(136) Innocenzi, P.; Malfatti, L.; Kldchob, T.; Falcaro, P. Order-Disorder in Self-Assembled Mesostructured Silica Films: A Concepts Review. *Chem. Mater.* **2009**, *21*, 2555-2564.

(137) Zuerner, A.; Kirstein, J.; Doeblinger, M.; Bräuchle, C.; Bein, T. Visualizing Single-Molecule Diffusion in Mesoporous Materials. *Nature* **2007**, *450*, 705-708.

(138) Moerner, W. E.; Fromm, D. P. Methods of Single-Molecule Fluorescence Spectroscopy and Microscopy. *Rev. Sci. Instrum.* **2003**, *74*, 3597-3619.

(139) Meyer, A. R.; Clark, A. M.; Culbertson, C. T. The Effect of Photomask Resolution on Separation Efficiency on Microfabricated Devices. *Lab Chip* **2006**, *6*, 1355-1361.

(140) Fu, Y.; Ye, F. M.; Sanders, W. G.; Collinson, M. M.; Higgins, D. A. Single Molecule Spectroscopy Studies of Diffusion in Mesoporous Silica Thin Films. *J Phys Chem B* **2006**, *110*, 9164-9170.

(141) Levy, G. Particle Tracker. *http://rsb.info.nih.gov/ij/*2009).

(142) Schmidt, T.; Schutz, G.; Baumgartner, W.; Gruber, H.; Schindler, H. Imaging of Single Molecule Diffusion. *Proc. Natl. Acad. Sci. U. S. A.* **1996**, *93*, 2926-2929.

(143) Ye, F.; Higgins, D. A.; Collinson, M. M. Probing Chemical Interactions at the Single-Molecule Level in Mesoporous Silica Thin Films. *J. Phys. Chem. C* **2007**, *111*, 6772-6780.

(144) Jung, C.; Schwaderer, P.; Dethlefsen, M.; Koehn, R.; Michaelis, J.; Braeuchle, C. Visualization of the Self-Assembly of Silica Nanochannels Reveals Growth Mechanism. *Nat. Nanotechnol.* **2011**, *6*, 86-91.

(145) Ehlich, D.; Takenaka, M.; Okamoto, S.; Hashimoto, T. Frs Study of the Diffusion of a Block Copolymer .1. Direct Determination of the Anisotropic Diffusion of Block Copolymer Chains in a Lamellar Microdomain. *Macromolecules* **1993**, *26*, 189-197.

(146) Jain, A.; Hall, L. M.; Garcia, C. B. W.; Gruner, S. M.; Wiesner, U. Flow-Induced Alignment of Block Copolymer-Sol Nanoparticle Coassemblies Toward Oriented Bulk Polymer-Silica Hybrids. *Macromolecules* **2005**, *38*, 10095-10100.

(147) Wagner, T.; Haffer, S.; Weinberger, C.; Klaus, D.; Tiemann, M. Mesoporous Materials as Gas Sensors. *Chem. Soc. Rev.* **2013**, *42*, 4036-4053.

(148) Shiju, N. R.; Alberts, A. H.; Khalid, S.; Brown, D. R.; Rothenberg, G. Mesoporous Silica with Site-Isolated Amine and Phosphotungstic Acid Groups: A Solid Catalyst with Tunable Antagonistic Functions for One-Pot Tandem Reactions. *Angew. Chem. , Int. Ed.* **2011**, *50*, 9615-9619.

(149) Yokoi, T.; Kubota, Y.; Tatsumi, T. Amino-Functionalized Mesoporous Silica as Base Catalyst and Adsorbent. *Appl. Catal. , A* **2012**, *421*, 14-37.

(150) Yamada, Y.; Mizutani, M.; Nakamura, T.; Yano, K. Mesoporous Microcapsules with Decorated Inner Surface: Fabrication and Photocatalytic Activity. *Chem. Mater.* **2010**, *22*, 1695-1703.

(151) Sierra, I.; Perez-Quintanilla, D.; Morante, S.; Ganan, J. Novel Supports in Chiral Stationary Phase Development for Liquid Chromatography. Preparation, Characterization and Application of Ordered Mesoporous Silica Particles. *J. Chromatogr. A* **2014**, *1363*, 27-40.

(152) Wang, Y.; Ai, F.; Ng, S.; Tan, T. T. Y. Sub-2 Mu m Porous Silica Materials for Enhanced Separation Performance in Liquid Chromatography. *J. Chromatogr. A* **2012**, *1228*, 99-109.

(153) Evers, S.; Nazar, L. F. New Approaches for High Energy Density Lithium-Sulfur Battery Cathodes. *Acc. Chem. Res.* **2013**, *46*, 1135-1143.

(154) Fujita, S.; Kamazawa, K.; Yamamoto, S.; Tyagi, M.; Araki, T.; Sugiyama, J.; Hasegawa, N.; Kawasumi, M. Proton Conductivity Under Dry Conditions for Mesoporous Silica with Highly Dense Sulfonic Acid Groups. *J. Phys. Chem. C* **2013**, *117*, 8727-8736.

(155) Beck, R. E.; Schultz, J. S. Hindered Diffusion in Microporous Membranes with Know Pore Geometry. *Science* **1970**, *170*, 1302-1305.

(156) Jirage, K. B.; Hulteen, J. C.; Martin, C. R. Nanotubule-Based Molecular-Filtration Membranes. *Science* **1997**, *278*, 655-658.

(157) Savariar, E. N.; Krishnamoorthy, K.; Thayumanavan, S. Molecular Discrimination Inside Polymer Nanotubules. *Nat. Nanotechnol.* **2008**, *3*, 112-117.

(158) Martin, C. R.; Nishizawa, M.; Jirage, K.; Kang, M. Investigations of the Transport Properties of Gold Nanotubule Membranes. *J. Phys. Chem. B* **2001**, *105*, 1925-1934.

(159) Baker, L.; Jin, P.; Martin, C. Biomaterials and Biotechnologies Based on Nanotube Membranes. *Crit. Rev. Solid State Mater. Sci.* **2005**, *30*, 183-205.

(160) Saxton, M. J. Single-Particle Tracking: The Distribution of Diffusion Coefficients. *Biophys. J.* **1997**, *72*, 1744-1753.

(161) Thompson, R.; Larson, D.; Webb, W. Precise Nanometer Localization Analysis for Individual Fluorescent Probes. *Biophys. J.* **2002**, *82*, 2775-2783.

(162) Grant, C. D.; Steege, K. E.; Bunagan, M. R.; Castner, E. W. Microviscosity in Multiple Regions of Complex Aqueous Solutions of Poly(Ethylene Oxide)-Poly(Propylene Oxide)-Poly(Ethylene Oxide). *J. Phys. Chem. B* **2005**, *109*, 22273-22284.

(163) Shiraishi, Y.; Inoue, T.; Hirai, T. Local Viscosity Analysis of Triblock Copolymer Micelle with Cyanine Dyes as a Fluorescent Probe. *Langmuir* **2010**, *26*, 17505-17512.

(164) Ghosh, S.; Mandal, U.; Adhikari, A.; Bhattacharyya, K. Study of Diffusion of Organic Dyes in a Triblock Copolymer Micelle and Gel by Fluorescence Correlation Spectroscopy. *Chem. - Asian J.* **2009**, *4*, 948-954.

(165) Constantin, D.; Oswald, P. Diffusion Coefficients in a Lamellar Lyotropic Phase: Evidence for Defects Connecting the Surfactant Structure. *Phys. Rev. Lett.* **2000**, *85*, 4297-4300.

(166) Constantin, D.; Oswald, P.; Imperor-Clerc, M.; Davidson, P.; Sotta, P. Connectivity of the Hexagonal, Cubic, and Isotropic Phases of the C12EO6/H2O Lyotropic Mixture Investigated by Tracer Diffusion and X-Ray Scattering. *J. Phys. Chem. B* **2001**, *105*, 668-673.

(167) Seebacher, C.; Hellriegel, C.; Deeg, F.; Brauchle, C.; Altmaier, S.; Behrens, P.; Mullen, K. Observation of Translational Diffusion of Single Terrylenediimide Molecules in a Mesostructured Molecular Sieve. *J. Phys. Chem. B* **2002**, *106*, 5591-5595.

(168) Schulz, B.; Taeuber, D.; Friedriszik, F.; Graaf, H.; Schuster, J.; von Borczyskowski, C. Optical Detection of Heterogeneous Single Molecule Diffusion in Thin Liquid Crystal Films. *Phys. Chem. Chem. Phys.* **2010**, *12*, 11555-11564.

(169) Schulz, B.; Taeuber, D.; Schuster, J.; Baumgaertel, T.; von Borczyskowski, C. Influence of Mesoscopic Structures on Single Molecule Dynamics in Thin Smectic Liquid Crystal Films. *Soft Matter* **2011**, *7*, 7431-7440.

(170) Kawai, T.; Yoshihara, S.; Iwata, Y.; Fukaminato, T.; Irie, M. Anisotropic Translational Diffusion of Single Fluorescent Perylene Molecules in a Nematic Liquid Crystal. *ChemPhysChem* **2004**, *5*, 1606-1609.

(171) Ryoo, R.; Ko, C. H.; Kruk, M.; Antochshuk, V.; Jaroniec, M. Block-Copolymer-Templated Ordered Mesoporous Silica: Array of Uniform Mesopores Or Mesopore-Micropore Network? *J. Phys. Chem. B* **2000**, *104*, 11465-11471.

(172) Imperor-Clerc, M.; Davidson, P.; Davidson, A. Existence of a Microporous Corona Around the Mesopores of Silica-Based SBA-15 Materials Templated by Triblock Copolymers. *J. Am. Chem. Soc.* **2000**, *122*, 11925-11933.